



**PROCESS FOR REFINING AND VALIDATING A FINITE ELEMENT MODEL
OF AN EXPERIMENTAL HIGH-ALTITUDE, LONG-ENDURANCE (HALE)
AIRCRAFT**

THESIS

Nicholas A. Sinnokrak, Lieutenant Commander, USN
AFIT/GAE/ENY/11-J04

**DEPARTMENT OF THE AIR FORCE
AIR UNIVERSITY**

AIR FORCE INSTITUTE OF TECHNOLOGY

Wright-Patterson Air Force Base, Ohio

APPROVED FOR PUBLIC RELEASE; DISTRIBUTION UNLIMITED

The views expressed in this thesis are those of the author and do not reflect the official policy or position of the United States Air Force, the United States Navy, the Department of Defense, or the United States Government. This material is declared a work of the U.S. Government and is not subject to copyright protection in the United States.

AFIT/GAE/ENY/11-J04

**PROCESS FOR REFINING AND VALIDATING A FINITE ELEMENT MODEL
OF AN EXPERIMENTAL HIGH-ALTITUDE, LONG-ENDURANCE (HALE)
AIRCRAFT**

THESIS

Presented to the Faculty

Department of Aeronautics and Astronautics

Graduate School of Engineering and Management

Air Force Institute of Technology

Air University

Air Education and Training Command

In Partial Fulfillment of the Requirements for the
Degree of Master of Science in Aeronautical Engineering

Nicholas A. Sinnokrak

Lieutenant Commander, USN

June 2011

APPROVED FOR PUBLIC RELEASE; DISTRIBUTION UNLIMITED.

**PROCESS FOR REFINING AND VALIDATING A FINITE ELEMENT MODEL
OF AN EXPERIMENTAL HIGH-ALTITUDE, LONG-ENDURANCE (HALE)
AIRCRAFT**

Nicholas A. Sinnokrak

Lieutenant Commander, USN

Approved:

Lt Col Christopher M. Shearer, USAF (Chairman)

Date

Dr. Eric D. Swenson (Member)

Date

Dr. Donald L. Kunz (Member)

Date

Abstract

The work presented here focuses on finite element (FE) modeling of X-HALE, a test aircraft designed and built by the University of Michigan, in conjunction with the Air Force Institute of Technology (AFIT) and Air Force Research Laboratory (AFRL). This scaled vehicle is representative of high-altitude, long-endurance (HALE) aircraft and was designed to provide controlled aeroelastic and flight data. FE models of portions of the X-HALE wing structure were created and analysis results were compared against two separate laboratory static bending tests conducted on X-HALE wing sections. The process documented here should improve future efforts to refine FE models of X-HALE. Improved modeling techniques will help design and test X-HALE to provide data for future designs of HALE aircraft and will also help to validate coupled nonlinear aeroelastic and flight dynamic codes. Results of the FE models created indicate the manufactured wing structure possesses material properties close to those expected of the composite materials used in its design. However, the results also suggest additional focus is required to accurately model the wing joint region of the X-HALE structure, with specific attention paid to the joiner piece which connects the wing sections together.

To my wife & son

Table of Contents

	Page
Abstract	iv
List of Figures	viii
List of Tables	xiii
Nomenclature	xiv
I. Introduction	1
Mission Requirements	2
Research Focus and Objectives	4
II. Background	6
HALE Aircraft	6
DARPA Vulture Program	11
Theory and Previous Research	11
X-HALE Overview	12
X-HALE Wing	14
Wing Joint	16
Setup and Apparatus of Laboratory Tests	19
Three-point Bending Test	20
Bending and Torsion Rig Test	23
Rig Design	23
Stiffness Tests	28
X-HALE Ground and Flight Testing	28
III. Methodology	32
FEMAP Uses and Limitations	33
Modeling Process	34
Three-point Bending Test	35
Simplifying Assumptions	38
Loads and Boundary Conditions	39
Loads	40
Boundary conditions	40
FE meshes	41
Contact Problem	45
Lessons Learned	55
Bending and Torsion Test Rig	59
Simplifying Assumptions	60

Loads and Boundary Conditions.....	61
FE Model Development.....	62
Lessons Learned.....	92
IV. Results and Discussion	96
Three-point Bending Test	96
Deformed Geometry.	98
Stress Contours.	98
Comparison to Laboratory Data.....	100
Quality of Load and Boundary Condition Definitions.	105
Additional Comments Regarding FE Model Quality.	106
Bending and Torsion Rig Test	107
Deformed Geometry.	109
V. Conclusions.....	119
Appendix.....	123
X-HALE Design Components	123
X-HALE Fabrication	125
Foam Core.....	125
Wing Box.	126
Wing Section.....	128
Wing Joint.....	130
X-HALE Testing.....	131
Test Plan [31].....	131
Previous Tests [31].	132
Bibliography	135
Vita.....	138

List of Figures

Figure	Page
Figure 1. Performance envelope for unmanned systems [3].....	4
Figure 2. Pathfinder aircraft at rest on Rogers Dry Lake Bed, c. 1992 [11].....	7
Figure 3. Pathfinder aircraft in flight, c. 1992 [11].....	7
Figure 4. Helios flying near the Hawaiian islands of Niihau and Lehua [15]	8
Figure 5. Plan view of ERAST Program aircraft plus front view of HP03 [23].....	9
Figure 6. AeroVironment, Inc. Global Observer's first flight [1]	9
Figure 7. Boeing's Phantom Eye UAV [2]	10
Figure 8. RQ-4 Global Hawk [3]	10
Figure 9. Final variant of X-HALE [8]	13
Figure 10. Plan- and front-views of X-HALE [9].....	14
Figure 11. Cross section of X-HALE wing with additional detail of wing box corner area (detail shows individual layers of fiberglass in blue) [28]	15
Figure 12. CAD model of a single wing section.....	16
Figure 13. a) Joiner block and b) alignment between joiner block and wing box [9]	17
Figure 14. Joiner block for outer dihedral wing joints [27]	17
Figure 15. Joiner sleeve joint fitting [29].....	18
Figure 16. Transparent CAD view of fairing structure [9]	19
Figure 17. Unassembled wing joint [28].....	21
Figure 18. Assembled wing joint showing strain gauges [28].....	21
Figure 19. Joined 2-wing test section (right side up) [28]	22
Figure 20. Wing Joint Bending Set-up [28].....	22
Figure 21. Laboratory wing joint 3-point bending test [28]	22
Figure 22. 3-point bending test loading cycle [28]	23
Figure 23. Test rig overview [20]	25
Figure 24. Wing mount assembly (showing 2 wings joined) [20].....	26
Figure 25. Bottom wing mount [20]	27
Figure 26. Top wing mount [20].....	27

Figure 27. X-HALE Transport Box	30
Figure 28. X-HALE Transport Box (Top View)	31
Figure 29. X-HALE Transport Box (Front View)	31
Figure 30. CAD model of 2 wing section and joiner block (separated apart)	37
Figure 31. FE model constraints indicated by red triangles.....	41
Figure 32. FE model constraints indicated by red triangles (front view)	41
Figure 33. Overlapping wing box and airfoil geometry and mesh	43
Figure 34. End of wing box model (only fiberglass wing box remains)	43
Figure 35. Model 3 deformed showing wooden joiner block inside wing box	45
Figure 36. Wing box joint without contact surfaces defined showing protruding joiner (with close-up detail of joiner block).....	46
Figure 37. Cantilever Test Model, Contact Surfaces NOT Activated	48
Figure 38. Successful Contact Test.....	48
Figure 39. Joined wing box model showing top wing box surfaces highlighted.....	50
Figure 40. Joined wing box model showing top joiner block surface highlighted	50
Figure 41. Joined wing box model showing bottom joiner block surface highlighted	51
Figure 42. Joined wing box model showing bottom wing box surfaces highlighted	51
Figure 43. Wing box joint with contact surfaces defined showing resulting contact forces (detail of Model 5, color contours show contact force).....	52
Figure 44. Deformed geometry (Model 6) with no foam in the airfoil.....	54
Figure 45. Behavior resulting from trailing edge mesh separation.....	55
Figure 46. Overlapping foam elements at leading edge of wing	57
Figure 47. Corrected leading edge foam element	58
Figure 48. Deformed model with load applied to nodes on the right wing box section	59
Figure 49. CAD drawing of single wing showing coordinate system	60
Figure 50. Single wing span representing only fiberglass structure	61
Figure 51. Original CAD geometry of single wing box	65
Figure 52. Undeformed (blue) and deformed (white) coarse mesh of wing box.....	66
Figure 53. Undeformed (blue) and deformed (white) fine mesh of wing box.....	67
Figure 54. Wing box mesh showing 3 different mesh sizes along span	68

Figure 55. View showing placement of load at free end of wing box with deformed mesh	68
Figure 56. Airfoil-only model of single wing showing applied load and constraint	70
Figure 57. Single wing model with color contours showing total element translation.....	71
Figure 58. Two single wing meshes with rigid elements (white lines) along free edge	72
Figure 59. Transparent view showing wing box and airfoil geometries merged.....	73
Figure 60. Initial mesh of combined wing box and airfoil model (top); and view showing poor chordwise alignment of airfoil and wing box elements (bottom).....	74
Figure 61. Outline of undeformed wing and deformed color contour mesh showing concentration of translated elements along trailing edge half of free edge	76
Figure 62. Outline of undeformed wing and deformed mesh showing elements of lower wing surface deflecting through those of upper wing surface	76
Figure 63. Undeformed wing (dark green) and deformed mesh (gray) with rigid links added between wing surfaces along free edge (white lines)	77
Figure 64. Wing box model with solid foam (bright blue) inside fiberglass walls	79
Figure 65. Undeformed outline and deformed color contour mesh of wing box with solid foam (bright orange).....	80
Figure 66. Wing mesh in the progress of adding solid foam elements (white) within fiberglass plate elements (gray)	80
Figure 67. Color contour mesh of foam-filled single wing model	82
Figure 68. Outline of single wing and deformed mesh resulting from test load applied to trailing edge of wing	83
Figure 69. Outline of single wing and deformed mesh resulting from test load applied to free edge of wing.....	84
Figure 70. Two-wing model with coincident nodes along joint highlighted	85
Figure 71. 2-wing model showing surface where loads were applied (highlighted yellow).....	86
Figure 72. Original CAD geometry of aluminum joiner	87
Figure 73. Single wing model with Al joiner imported from original CAD	88
Figure 74. Single wing model with Al joiner imported from original CAD	88
Figure 75. Single wing box mesh with Al joiner imported from original CAD.....	89
Figure 76. Single wing box mesh with Al joiner imported from original CAD	89
Figure 77. Single wing model with Al joiner copied to free end of wing	90

Figure 78. FE mesh of two wing sections with Al joiner (highlighted yellow).....	91
Figure 79. FE mesh of two wing sections with Al joiner (highlighted yellow).....	91
Figure 80. View of 2 m wing section subjected to 3-point bending test showing deflection reference line between wing tips	97
Figure 81. Deflection of wing joint vs. time resulting from 3-point bending test	97
Figure 82. Front view of Model 8 showing deformed mesh geometry (color contours indicate total translation)	99
Figure 83. Close up view of Model 8 mesh at the joint showing separation between elements of each wing section as well as joiner protrusion	99
Figure 84. Plate Stress Contour (Model 8, 60lb load)	100
Figure 85. Plate Stress at Center of Airfoil (Model 8, 60lb load).....	100
Figure 86. Comparison of load vs. displacement results amongst lab and 8 FE models	102
Figure 87. Comparison of displacement results between lab test, Model 8, and 3 versions of Model 8 with modified material properties	104
Figure 88. Wing tip deflections for 4 single test wing sections under loading conditions	108
Figure 89. Wing tip deflections for 2 joined test wing sections under loading conditions	108
Figure 90. Free end of wing box model showing total translation under applied load with original position of wing box outlined	109
Figure 91. Deflection of combined wing box / airfoil model for 0.67 lb (3N) applied load (0.276 in. maximum deflection indicated)	113
Figure 92. Exaggerated deflection of wing mesh showing deformation without (left) and with (right) rigid links between airfoil surfaces forward of the wing box	114
Figure 93. Mesh of full wing model showing translation contours	114
Figure 94. Deformations of the final single wing model under 5 loading conditions (undeformed wing in blue/green)	116
Figure 95. Simple 2-wing model under 3 N load showing original position (blue/green) and deformed position (gray mesh)	117
Figure 96. Simple 2-wing model under 7 N load showing original position (blue/green) and deformed position (gray mesh)	118
Figure 97. Off-angle and front views of fairing [28]	123
Figure 98. Front view of 6-m version of X-HALE showing dihedral wing joint.....	124
Figure 99. Side view of spine / fairing / tail section showing typical arrangement of internal electronics of each fairing.....	124

Figure 100. Uncut foam blocks with acrylic templates attached prior to sanding.....	125
Figure 101. Aluminum wing mold used to shape and cure the X-HALE airfoil.....	126
Figure 102. Carbon fiber end of wing box.....	127
Figure 103. Wing box end with carbon fiber dowels added attached to wing box foam.....	127
Figure 104. Layup assembly for wing box	128
Figure 105. End of finished wing box (left) and cross section (right).....	128
Figure 106. Completed wing box attached to leading and trailing edge sections of foam.....	129
Figure 107. Single wing assembly before (left) and after (right) final fiberglass layer.....	129
Figure 108. Layup arrangement for single wing section	129
Figure 109. Three-view diagram of aluminum joiner block with dimensions	130
Figure 110. Three-view diagram of dihedral version of aluminum joiner block.....	131
Figure 111. Graph of Power vs. Thrust [31].....	133

List of Tables

Table	Page
Table 1. Summary of FE models and descriptions	38
Table 2. Summary of FE models and descriptions	101
Table 3. Comparison of laboratory and FE model wing tip deflections for five load cases	110

Nomenclature

Abbreviation

AFIT	Air Force Institute of Technology
AFRL	Air Force Research Laboratory
ATV	Aeroelastic Test Vehicle
CAD	Computer-aided Design
cg	Center of Gravity
DARPA	Defense Advanced Research Projects Agency
E	Modulus of Elasticity / Young's modulus
EI	Bending stiffness
FE	Finite Element
FEMAP	Finite element modeling and post-processing application
FTV	Flight Test Vehicle
FQ	Flying qualities
GPS	Global Positioning System
HALE	High-Altitude, Long-Endurance
ISR	Intelligence, Surveillance, and Reconnaissance
R/C	radio controlled
RPA	Remotely Piloted Aircraft
UM/NAST	University of Michigan's Nonlinear Aeroelastic Simulation Toolbox
X-HALE	Experimental High-Altitude, Long-Endurance

PROCESS FOR REFINING AND VALIDATING A FINITE ELEMENT MODEL OF AN EXPERIMENTAL HIGH-ALTITUDE, LONG-ENDURANCE (HALE) AIRCRAFT

I. Introduction

The desire to fly higher and farther has existed as soon as humans took to the skies over two centuries ago. Aircraft designs have evolved profoundly during this time. Initial designs attempted to mimic birds and therefore focused on flapping wings of various sorts. Once Sir George Cayley of England set the study of aeronautics down the path of fixed wing craft, aviation history was destined towards airmen such as Otto Lilienthal and the Wright brothers. Ultimately, after overcoming the challenge of aircraft propulsion, Orville and Wilbur Wright were able to successfully control their Wright Flyers utilizing wing warping techniques. Upon understanding basic aerodynamics and effective means of aircraft control, aeronautical engineering experienced exponential developments throughout the 20th Century [7].

The arena of aeronautical design again finds itself looking to extend the endurance and application of aircraft far beyond what is most commonly understood to be normal. With the continued advancement and reliability of automated systems, aircraft that can remain airborne for years at a time are nearing the realm of reality.

Mission Requirements

The past decades have seen a dramatic rise in the use of and reliance on satellites for various purposes. Scientific research and military operations alike gather vast amounts of data from these orbiting platforms. Although their value is readily apparent, there are many drawbacks to using satellites. The sensor payloads within satellites are expensive and complicated to design, as they are required to operate reliably in extremely harsh conditions. The mere act of launching satellites is somewhat risky, and by extension costly. The capital investment required up front to successfully place a satellite into orbit is enormous and often prohibitive. Once launched, the coverage areas of satellites are often difficult to adjust, usually requiring large constellations to provide the desired coverage. In contrast, high-flying aircraft are less costly to launch and much less expensive to test. The ability to adjust an aircraft's flight path, and thereby coverage area, is far less complicated both to plan and execute. And with take-off and landing the riskiest portions of an aircraft's flight, the longer an aircraft stays aloft the more of its operational life it spends in a relatively benign environment [11]. Along with improved reliability, maintainability, and modularity, these are just some of the advantages which a high-altitude, long-endurance [34] (HALE) aircraft possesses over satellites. Of course, long before satellites became commonplace aircraft were operating at great heights. Military aircraft such as the U-2 and B-52 have exploited altitude extremes in order to collect information undetected or as a defensive means by remaining out of the reach of adversaries. Scientific aircraft such as Voyager or Helios used extreme altitudes out of necessity to break range and endurance records.

The United States Department of Defense's roadmap for all unmanned systems highlights the desire for increased endurance and range for unmanned aircraft systems (UAS); note the highlighted portion of Figure 1 [3]. While mission endurance is currently most often measured in hours, in the future it will be both beneficial and necessary for UAS aircraft to be able to "conduct their missions in durations measured in days, weeks, months, and feasibly years [3]." Especially for high altitude missions, such as Intelligence, Surveillance, and Reconnaissance (ISR) and data gathering for scientific purposes, operations are almost always limited by the constraints of the human body – our need for food and sleep. Zephyr and Global Observer HALE systems are already in development or being procured. These systems are envisioned to fill the need to have an asset orbit for weeks at a time providing a communication link over an area of thousands of square miles, or to develop power systems able to support HALE UAS operations, respectively. Development is planned within this decade for a persistent HALE UAS able remain on station for months at a time without refueling, providing continuous ISR capabilities.

Aircraft such as these which are designed to fly primarily at altitudes far above those used by current commercial aircraft share some specific characteristics. Specifically, their long wings have relatively large aspect ratios and thick airfoils as compared to more conventional aircraft. At high altitudes thicker airfoils have lower critical Mach numbers due to a lower speed of sound as compared to sea level. For maximum endurance these aircraft have very lightweight structures with flexible wings which tend to experience large deformations during normal, trimmed flight. The results of a wing with higher Mach flows and extreme deformations can be nonlinear

aerodynamics and aeroelastic effects where the assumption of small displacements is no longer valid [17].

	2009	Evolutionary Adaptation	2015	Revolutionary Adaptation	2034
Commands	Physical Human Machine Interfaces		Scripted Voice Command/Hand Signals		Natural Language Understanding
Collaboration	Individual System		Teaming w/in Domain Collaboration Across Domains		Teamed Collaboration
Frequency	Constrained RF		Frequency Hopping		Multi-Frequency Communications
Mission Complexity	Operator Controlled				Autonomous Adaptive Tactical Behaviors
Environmental Capability	Limited Environmental Difficulty		Expanded Environmental Difficulty		All-Weather Environmental Difficulty
Product Line	Mission Package Product Line Dependent				Product Line Independent
OPSEC	Signature High				Signature Low
Operational Control	1 Operator / Platform		1 Operator / Domain		1 Operator / Team
Bandwidth	Limited		Advanced Bandwidth Management		Autonomous Bandwidth
Mission Endurance	Hours		Days	Months	Years
Maintenance	Operator				Automated
Awareness	Sensor Data		Situational Awareness		Actionable Information

Figure 1. Performance envelope for unmanned systems [3]

Research Focus and Objectives

Before these objectives of greatly increased range and endurance can be fulfilled, many questions about such aircraft must be answered. A deeper understanding of the nonlinear aerodynamics and aeroelastic effects which such aircraft encounter, as well as what causes them, will have to be attained before these vehicles can be reliably designed. Among the tools used for such design work, finite element (FE) modeling and analysis will play a part in accurately and efficiently bringing HALE aircraft about. FE modeling is useful in almost any design development for various reasons, not the least of which is

the ability to minimize destructive testing on physical system components. In this particular case an FE model is desired to compare to laboratory bending test results from portions of an experimental HALE aircraft called X-HALE. FE analysis results in this thesis will be compared to results of static testing conducted on wing sections of the X-HALE aircraft. The ultimate goal of this effort will be to create and validate an FE model of the X-HALE vehicle. Improved modeling processes will help characterize X-HALE to provide data for future designs of HALE aircraft.

The FE modeling work done here was intended to mirror static laboratory testing that had been conducted on portions of the X-HALE wing. The Finite Element Modeling and post-processing Application (FEMAP) by Siemens PLM Software was utilized for all FE modeling produced for this research. Initial model results were compared against results from a three-point bending laboratory test on a two-wing section of X-HALE at the University of Michigan in the early design phase of this program. Although small in scope, the modeling of this test provided many lessons learned and much needed experience of both the general FE process as well as FEMAP specifics. The core of this research effort consisted of more rigorous modeling work which attempted to reproduce recent laboratory bending tests conducted on multiple portions of the X-HALE vehicle.

II. Background

HALE Aircraft

With the realization that satellites are not always the best option for missions requiring a perspective high above Earth, the development of HALE aircraft has gathered much interest. Early in the 1980s it was understood that solar power would be the power source for a high altitude aircraft that was to remain airborne for days at a time, and it was during this time that AeroVironment designed and built their HALSOL (High-Altitude SOLar vehicle) prototype aircraft [11]. A decade later, under different government sponsorship, the HALSOL aircraft was updated and became Pathfinder (Figure 2 and Figure 3).

In an effort to continue the advancements of HALE UAVs, NASA and AeroVironment formed the Environmental Research Aircraft and Sensor Technology (ERAST) project. This program was specifically created to develop the capabilities necessary for a UAV to fly at high altitudes for extended durations. Pathfinder became the first of five HALE test bed aircraft that would advance those technologies required to design and develop aircraft with the required lightweight composite structures, low wing loading, and low Reynolds number aerodynamics. These test aircraft also provided necessary developments in many other technologies relating to motors, thermal control, solar arrays, avionics and flight control systems, and flight operations at high altitude. Five distinct UAVs were designed, built, and tested under the



Figure 2. Pathfinder aircraft at rest on Rogers Dry Lake Bed, c. 1992 [11]



Figure 3. Pathfinder aircraft in flight, c. 1992 [11]

ERAST program, culminating with two configurations of Helios Prototype aircraft. Helios can be seen in Figure 4, while Figure 5 compares relative sizes of these five aircraft.

This early work at developing HALE UAV technologies and techniques have increased in recent years. AeroVironment is currently continuing HALE UAV work with its Global Observer, designed to stay aloft for over five days and prove the utility for an aircraft to function as a quasi-satellite. In addition, Boeing is working on their Phantom Eye HALE demonstrator and Northrop Grumman plans to use a variant of their Global Hawk modified to be capable of conducting mid-air refueling. Images of these HALE UAVs can be seen in the following figures.



Figure 4. Helios flying near the Hawaiian islands of Niihau and Lehua [15]

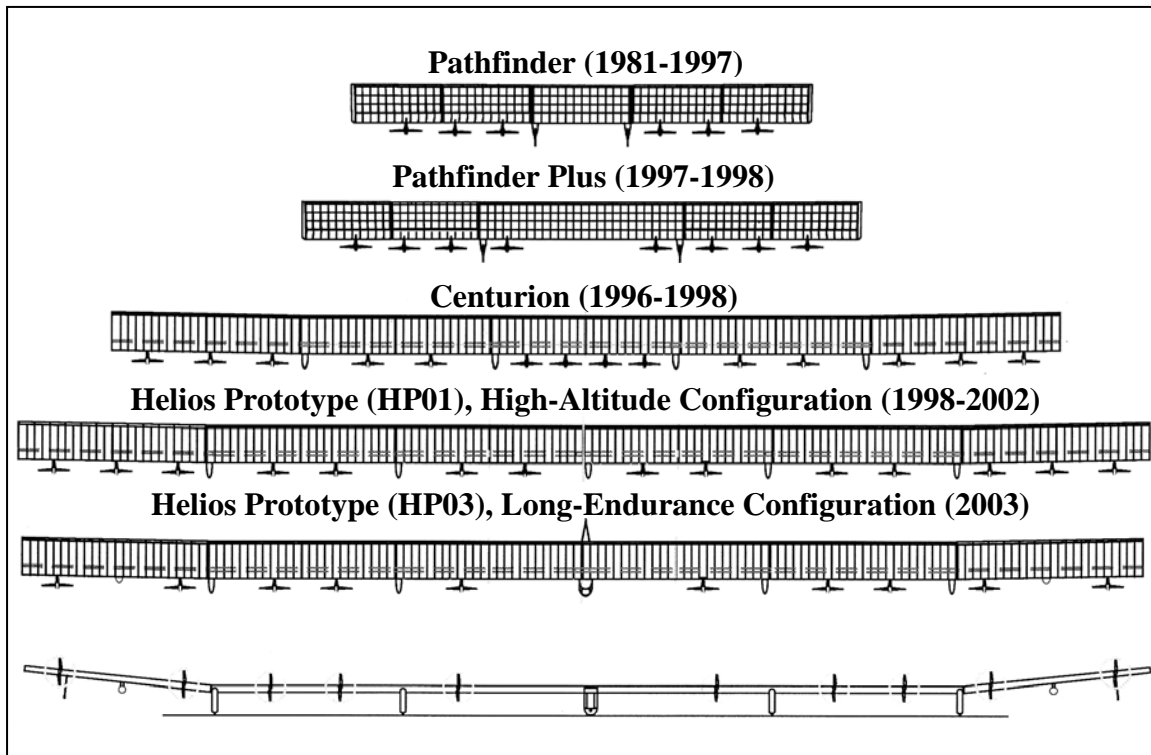


Figure 5. Plan view of ERAST Program aircraft plus front view of HP03 [23]



Figure 6. AeroVironment, Inc. Global Observer's first flight [1]



Figure 7. Boeing's Phantom Eye UAV [2]



Figure 8. RQ-4 Global Hawk [3]

DARPA Vulture Program

The Defense Advanced Research Projects Agency's (DARPA) Vulture Program aims to push the goals of these previous efforts even further. DARPA set a goal of developing an unmanned aircraft which could stay airborne for five years without refueling while carrying a 1000 lb payload with which to provide reliable sensor data [13]. In April 2008 three contracts were awarded to begin this development, and in late 2010 the Phase II contract was awarded to The Boeing Company to continue development and demonstration work on this program [36, 12].

Theory and Previous Research

Although the ERAST program made great strides in demonstrating the reality of an unmanned aircraft with both extended endurance and the ability to fly at extreme altitudes, a lack of adequate analysis tools prevented designers from predicting the behavior of such a structure when it encountered extreme flight conditions. The HP03 Helios aircraft was flying its second high altitude test flight on 26 June 2003 when it encountered turbulent air which caused it to experience severe wing dihedrals and pitch oscillations, resulting in the in-flight catastrophic failure of the vehicle [23]. This mishap highlighted the difference in behavior of HALE aircraft as compared to more conventional aircraft and the need to more confidently predict and analyze structures which behave in a nonlinear aeroelastic manner [22]. Apart from the Helios mishap, significant analysis on the nonlinear aeroelastic behavior of HALE wings has been conducted over the last decade [10, 24, 25, 30, 32, 33, 35]. This work has shown that

traditional design methods employing linear aerodynamic equations are not appropriate for such aircraft designs.

X-HALE Overview

The University of Michigan, with AFIT participation and AFRL support, has designed and built a remotely piloted vehicle which is aeroelastically representative of very flexible aircraft. This experimental HALE aircraft, called X-HALE, has been developed from which nonlinear aeroelastic-coupled rigid body flight dynamics data can be collected in order to validate nonlinear aeroelastic codes and is intended to provide open source data for construction and testing of future HALE aircraft [9]. Kaszynski has explained in detail the background and evolution of design requirements which became X-HALE [18].

The X-HALE concept consists of two aircraft configurations – a Flight Test Vehicle (FTV) and an Aeroelastic Test Vehicle (ATV). The FTV will be the first configuration to be built and flown. Its purpose is to assess X-HALE’s handling and maneuverability. To do this the FTV will include only an abbreviated science sensor package but a full housekeeping sensor package [9, 18]. The purpose of the ATV is to study the aeroelastic behavior of X-HALE. To this end the ATV will only contain abbreviated housekeeping sensors, leaving room for a complete science sensor package. Much like the evolutionary development of previous HALE UAVs, X-HALE will initially be controlled by a pilot via R/C control, although ultimately an autopilot is intended to be incorporated into the design.

In keeping with HALE aircraft designs discussed previously, X-HALE is a high aspect ratio aircraft with multiple boom-tails connected to the flexible wing structure. The main component of the aircraft is the EMX07 reflexed airfoil, which forms each 1-m long section of wing along the span and has a 0.2-m chord. Initial design specifications called for six wings, five motor pods, and four boom-tails. All five pods were covered in fairings, made into the shape of NACA 0010-66 airfoils [28], to contain a propeller motor, battery, and processor boards. Pitch and roll are to be controlled by the four outboard horizontal tails (attached to the ends of the 0.83-m long booms) and yaw controlled using differential thrust from the outboard motors. The outer dihedral wings were designed with ailerons to supplement the planned in-flight disturbances [9]. Adjustments and improvements to this design were made, including two additional wings and one more boom-tail at the center pod. The current aircraft consists of eight identical 1-m wing sections resulting in an overall 8-m span (Figure 9 and Figure 10).

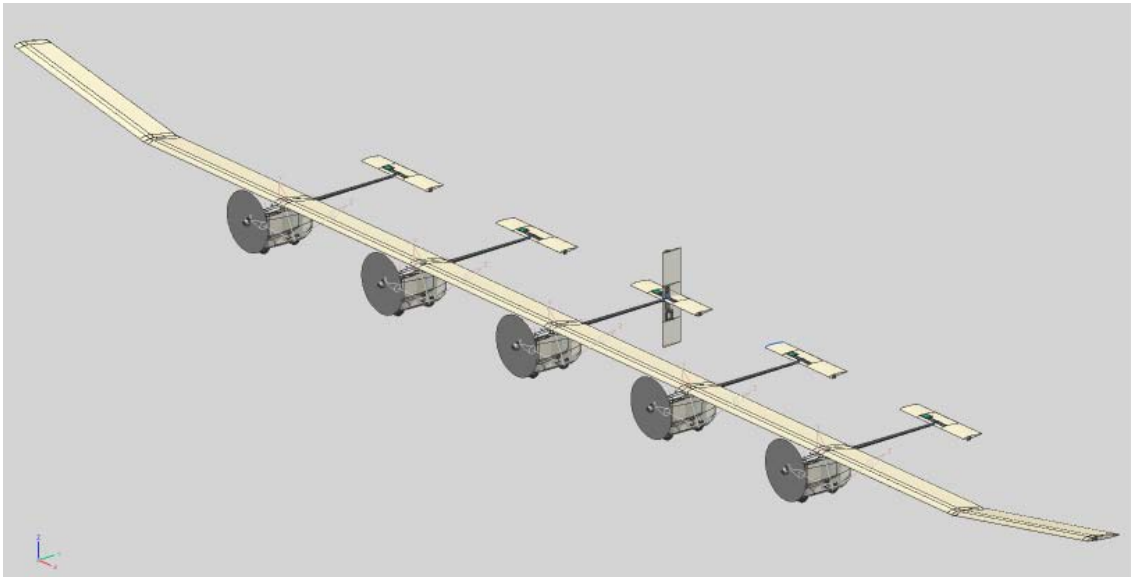


Figure 9. Final variant of X-HALE [8]

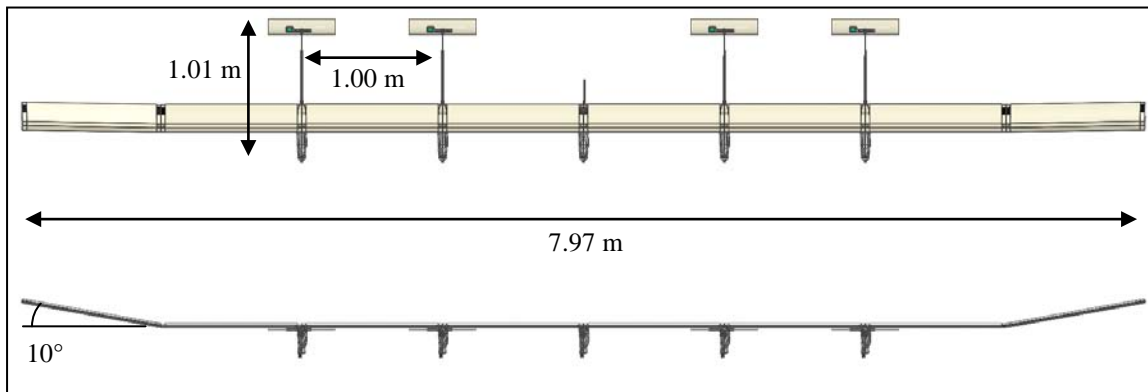


Figure 10. Plan- and front-views of X-HALE [9]

X-HALE Wing.

X-HALE was designed with completely composite wing sections, utilizing fiberglass fabric and unidirectional carbon epoxy prepregs, as well as low density isotropic structural foam. The main structural component of each wing section is a wing box running the length of the airfoil with a cross section measuring approximately 1.18 in. along the chord and 0.69 in. high. The perimeter of the wing box is constructed from five layers of E-Glass 120 fiberglass [4]. The EMX07 airfoil, with a 7.84 in. chord and a maximum thickness of 0.69 in., is constructed from a single layer of the same E-Glass 120 fiberglass wrapped around the previously made wing box. Each layer of fiberglass is 0.0047 in. thick. The outer 1.25 in. of both the wing box and airfoil are reinforced by multiple layers of uni-graphite epoxy. All hollow space within the airfoil and wing box is filled with Rohacell 31-IG foam core [6]. A cross section of the EMX07 airfoil showing the shape and location of the wing box, as well as the relative layers of fiberglass, can be

seen in Figure 11 [28]. A transparent CAD model depiction of a single wing section is shown in Figure 12. Kaszynski has provided a detailed summary of the construction of X-HALE, including a step-by-step explanation of the wing layup [18]. A brief overview of the processes related to X-HALE's wing structure can be found in the Appendix.

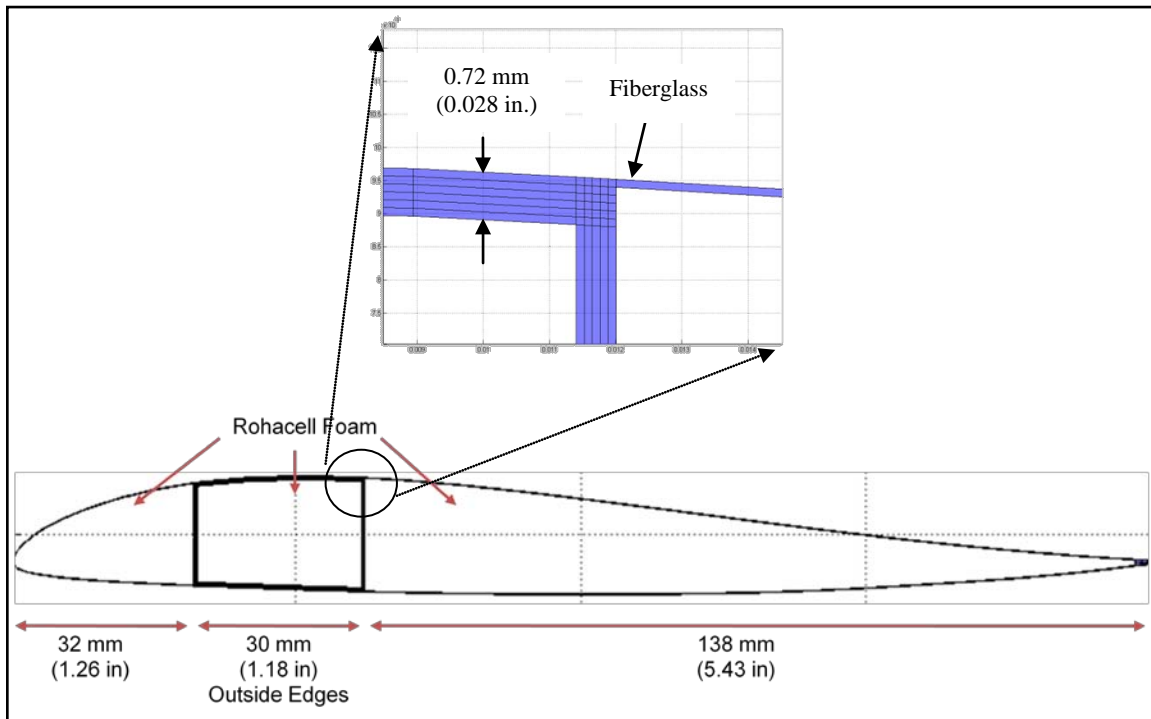


Figure 11. Cross section of X-HALE wing with additional detail of wing box corner area (detail shows individual layers of fiberglass in blue) [28]

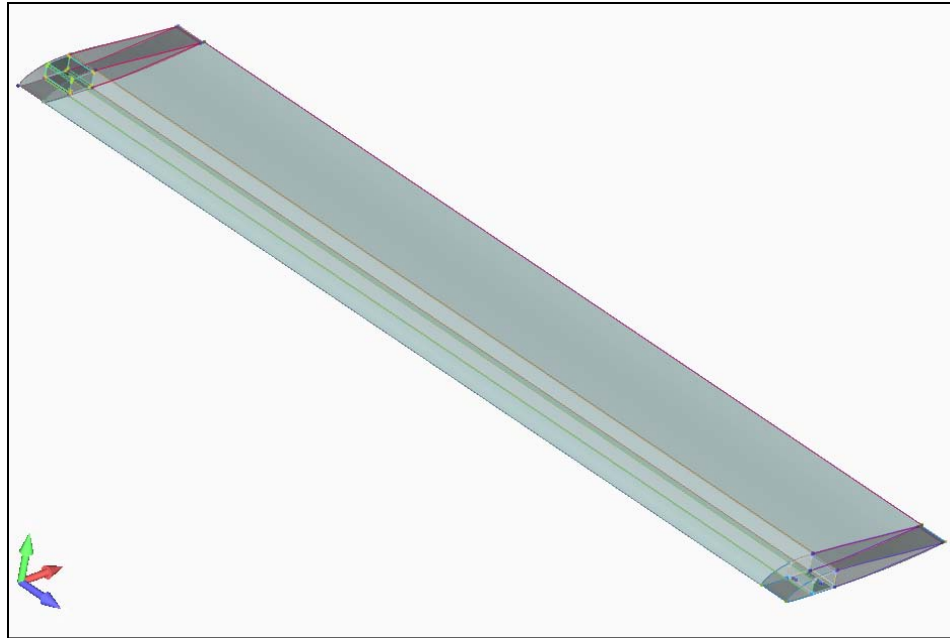


Figure 12. CAD model of a single wing section

Wing Joint.

Between each wing section is a joint which connects the wings to the five spines holding the pod / fairing assemblies. The joint between each wing section consists of a wing joiner block, a fiberglass joint sleeve, and aluminum L-brackets. The joiner block is a single piece of aluminum which was machined to fit within the reinforced opening at the end of each wing box. The joiner block was designed as a single piece to fasten each pair of wing sections together, thereby transferring any bending loads through the wing boxes and acting as a structural fuse. In the event of a sudden impact or severe bending load the joiner was designed to fail before the wing or wing box, thus allowing for the replacement of the joiner and preventing the need to manufacture additional wing sections. The joiner was also designed to allow pathways for the wiring required within the structure of the wings and pods. The joiner pieces for the inner five wing joints were

designed to be identical, and the pieces which join the outboard dihedral wing sections to their inner partners were designed to match the designed 10 degree dihedral angle of those outer sections. Figure 13 and Figure 14 provide further details of the aluminum joiner's design.

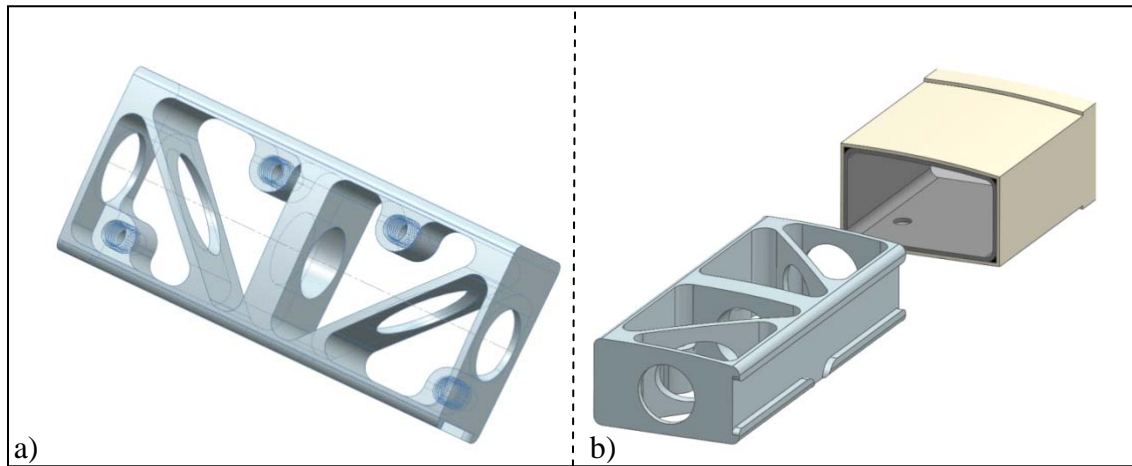


Figure 13. a) Joiner block and b) alignment between joiner block and wing box [9]

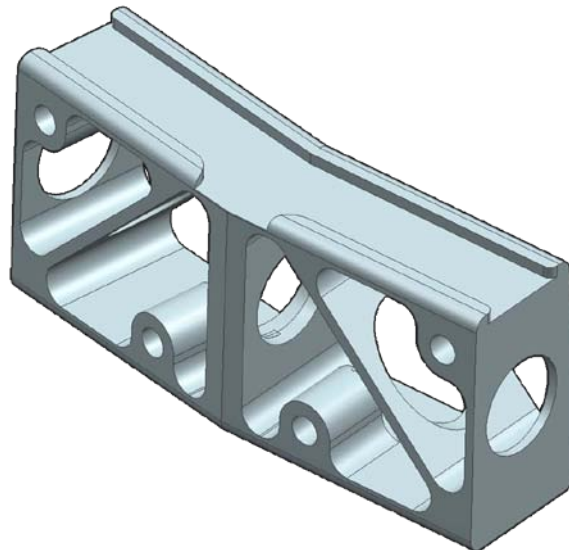


Figure 14. Joiner block for outer dihedral wing joints [27]

A simple fiberglass sleeve was designed to enclose the spanwise portion of the wing along the wing joint. The sleeve was constructed in the shape of the airfoil in a similar method as described above. The ends of each wing section were constructed with a tapered portion to allow the joiner sleeve to slip over both ends. This portion of the joint design provided for the transfer of shear loads through the fiberglass wing skin. Figure 15 depicts the joiner sleeve and how it fits onto the wing section.

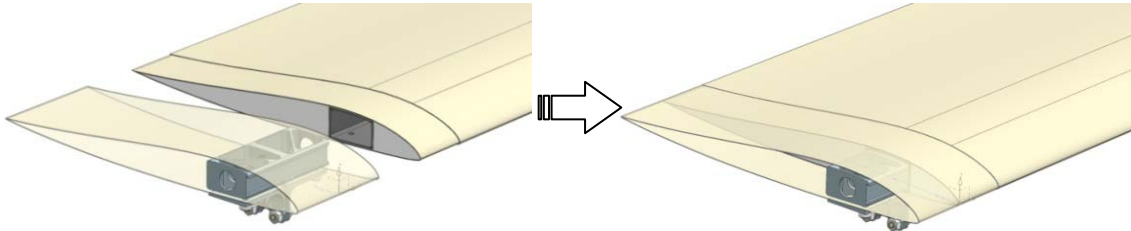


Figure 15. Joiner sleeve joint fitting [29]

Finally, aluminum L-brackets were used to connect each wing section to its corresponding fairing. The brackets were designed to attach to the wing by being bolted through the joiner sleeve and lower surface of the wing box into the aluminum joiner. The lower portion of the L-brackets were then fastened to the carbon fiber spine of each fairing, which provides attachments points and support for the internal components of each pod. This connection is depicted in Figure 16.

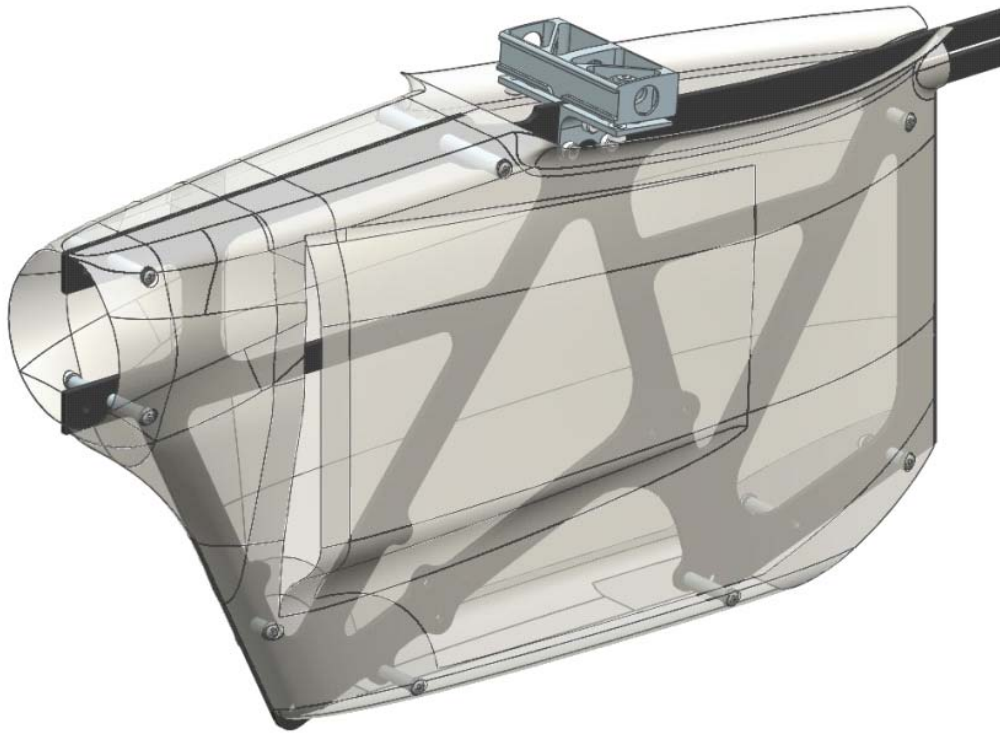


Figure 16. Transparent CAD view of fairing structure [9]

Setup and Apparatus of Laboratory Tests

Nearly all components of X-HALE were tested throughout the design process. Numerous performance tests were conducted on mechanical and electrical components inside X-HALE and the structure was subjected to mass and stiffness testing as well as aeroelastic simulations. The X-HALE Test Plan is summarized in the Appendix and covers these tests in more detail [31]. In addition, two specific sets of tests were performed on the X-HALE structure. The first test was conducted early in the design process of X-HALE. An initial FEMAP model was created and compared against the results of this test while design work on X-HALE continued. The second test was conducted in a more controlled apparatus which allowed for the collection of more

refined data and would be better suited to validate the FE model developed for that test. However, the FE model created to represent the early bending test will also be discussed here to illustrate lessons learned and steps taken in the development of more refined models.

Three-point Bending Test.

The University of Michigan previously subjected a joined two-wing portion of the X-HALE vehicle to various bending loads in a static laboratory environment. The test setup consisted of two wing sections joined together by the joiner sleeve and a basswood joiner (in place of the previously noted aluminum joiner block). The wood joiner connected the two wings inside the joiner sleeve, secured together via two screws from underneath the airfoil (see the following figures for detail). This test section was placed upside down on two rollers with the joint in the middle of an apparatus that would apply loads to the bottom of the combined wing at the joint (Figure 20 and Figure 21) [28].

The wing joint was then subjected to several loads by this three-point bending test stand. A maximum target load of 120 lbs was planned for this test. Loading was conducted in cycles: the test was designed to apply increments of 20 lbs loads at a time, with 10 lbs of load removed in between each increased loading. The test apparatus was designed to apply loading by displacing the center joint at a rate of 0.15 in./min during both positive and negative loading. See Figure 22 for a graph showing the loading timeline. The deflection of the joint in relation to the wing tips was measured for each applied load. Although this test was planned with a target load of 120 lbs, failure of the wing joint prevented testing beyond approximately 60 lbs of applied load [28].

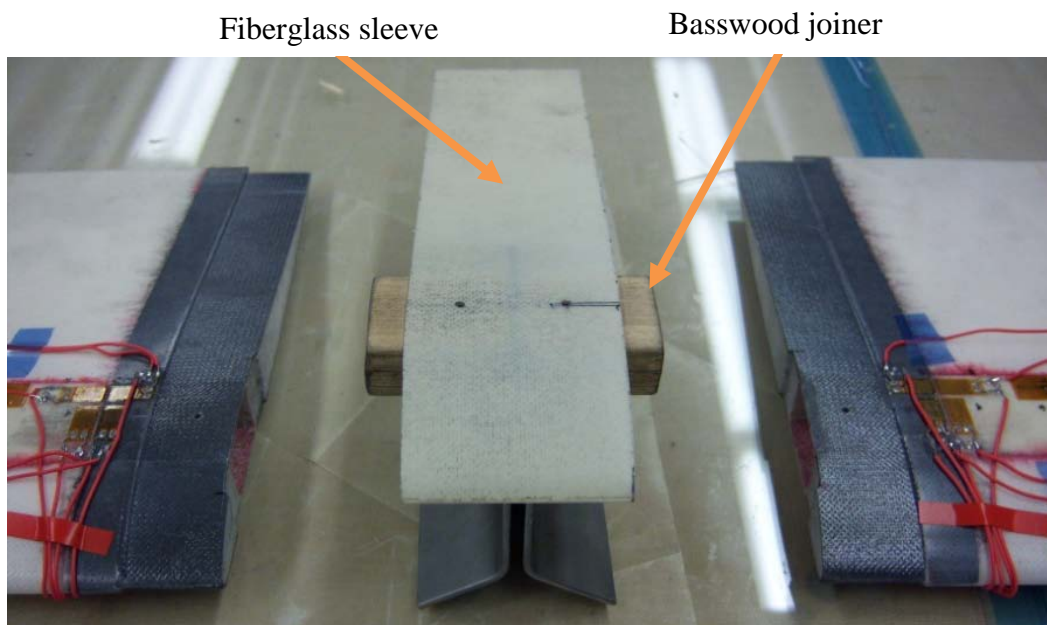


Figure 17. Unassembled wing joint [28]

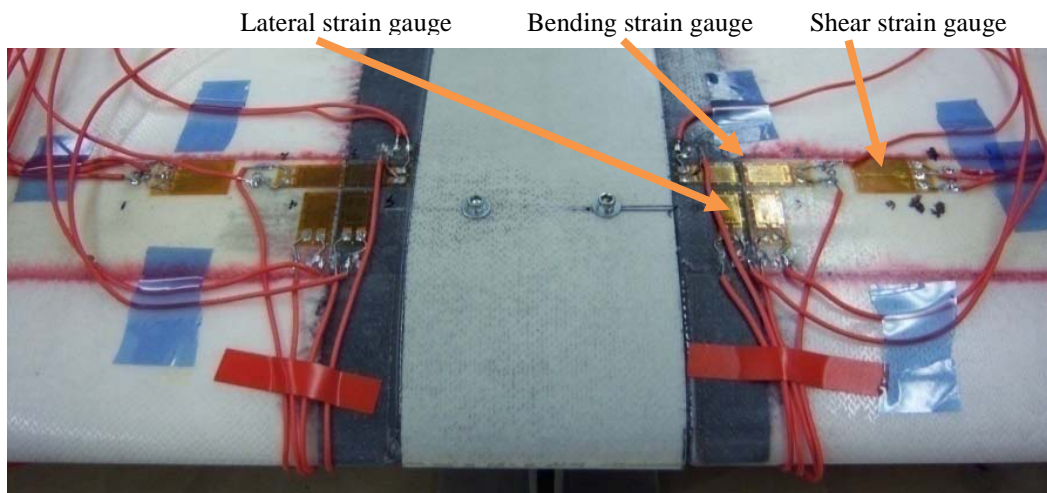


Figure 18. Assembled wing joint showing strain gauges [28]

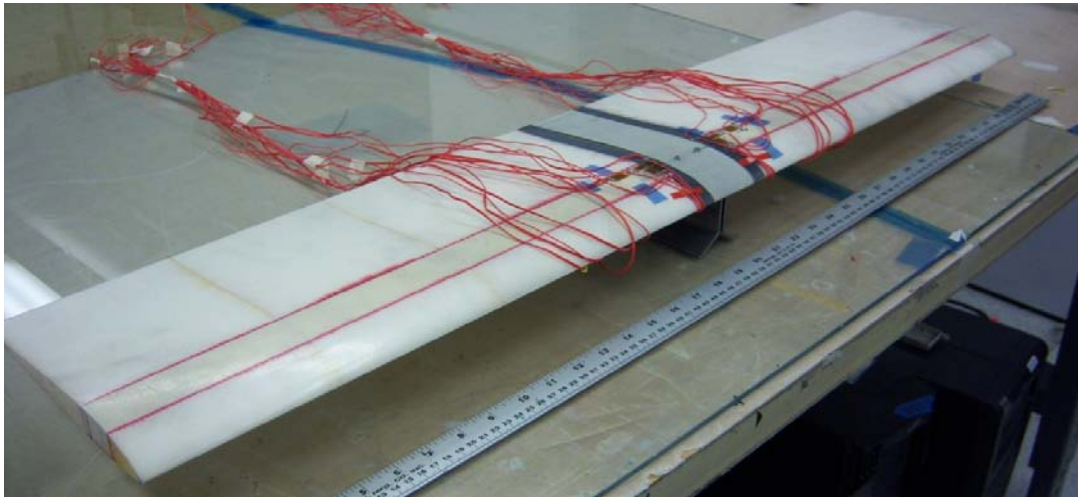


Figure 19. Joined 2-wing test section (right side up) [28]

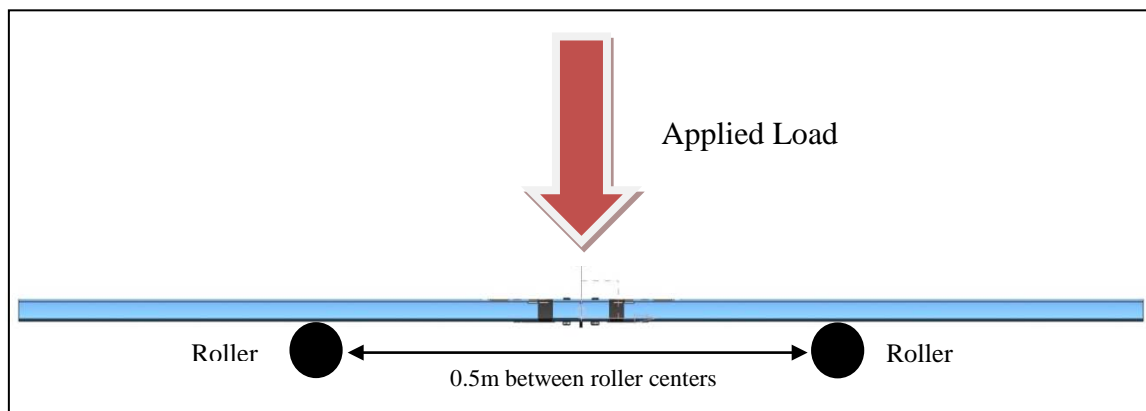


Figure 20. Wing Joint Bending Set-up [28]

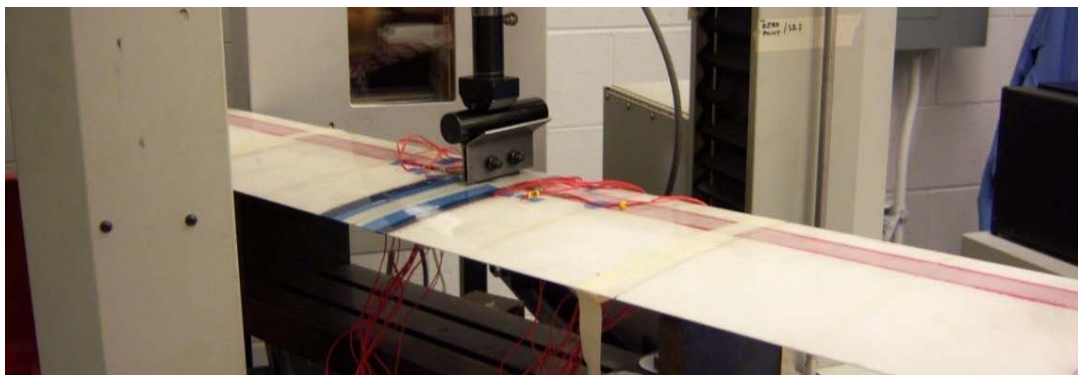


Figure 21. Laboratory wing joint 3-point bending test [28]

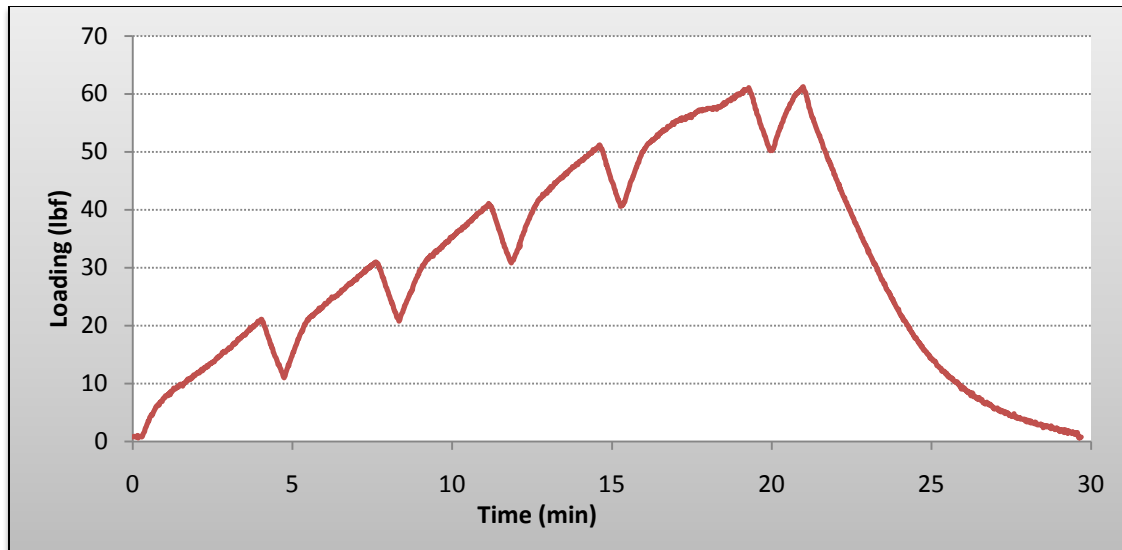


Figure 22. 3-point bending test loading cycle [28]

Bending and Torsion Rig Test.

Although the three-point bending test described above was a valuable step in the design of X-HALE, it did not yield a wealth of data nor was it practical to use repeatedly on multiple sets of wing sections. It was desired to be able to perform a more controlled set of tests on completed sections of the X-HALE wing structure and repeat them as necessary with minimal risk of damaging the fabricated pieces. To this end, a second test setup was constructed in order to conduct bending and torsion tests on single wings as well as combinations of two wings joined together.

Rig Design.

The University of Michigan Active Aeroelasticity and Structures Research Lab designed and built a characterization rig for the X-HALE wing(s). This apparatus was designed such that the wing is mounted vertically to a base plate on the floor. The base

plate, a 0.375 in. thick piece of steel measuring 40 in. by 30.125 in., was bolted to the floor of the test lab to provide a connection point for the remainder of the rig structure. The support frame portion of the rig was constructed of steel Unistrut beams, assembled into a large rectangular box structure with a height of 98 in. and a square footprint of 21.75 in. each side. The frame was bolted to four Unistrut post bases, each of which were welded to the base plate. An additional sliding square assembly of beams is bolted to the outside perimeter of the structure, onto which are mounted a series of pulleys. These pulleys allowed a downward gravitation force from hanging weights to be transferred into horizontal forces which were applied to the mounted cantilever-style wing. Laser measurements were then taken along the wing span. Figure 23 shows this test rig.

Each section of wing, or joined section of two wings, to be tested was mounted within the test rig using two pairs of aluminum wing mounts which were made from scrap pieces of the original wing mold. This provided mounts which exactly matched the contour of the airfoils. An example set up of two joined wings and the wing mounts can be seen in Figure 24. The bottom wing mount used angled brackets and screws to attach to the base plate and fastened the wing to the rig by clamping around the bottom couple inches of its span. Similarly, the top wing mount clamped around roughly 1.5 inches of the opposite end of the wing's span. Four eye bolts were screwed into the sides of the top wing mount, two on each side, and were used to attach wire which applied the bending and torsion loads. Figure 25 and Figure 26 show the bottom and top wing mounts, respectively. Additional details can be found in the report by Matthews [20].

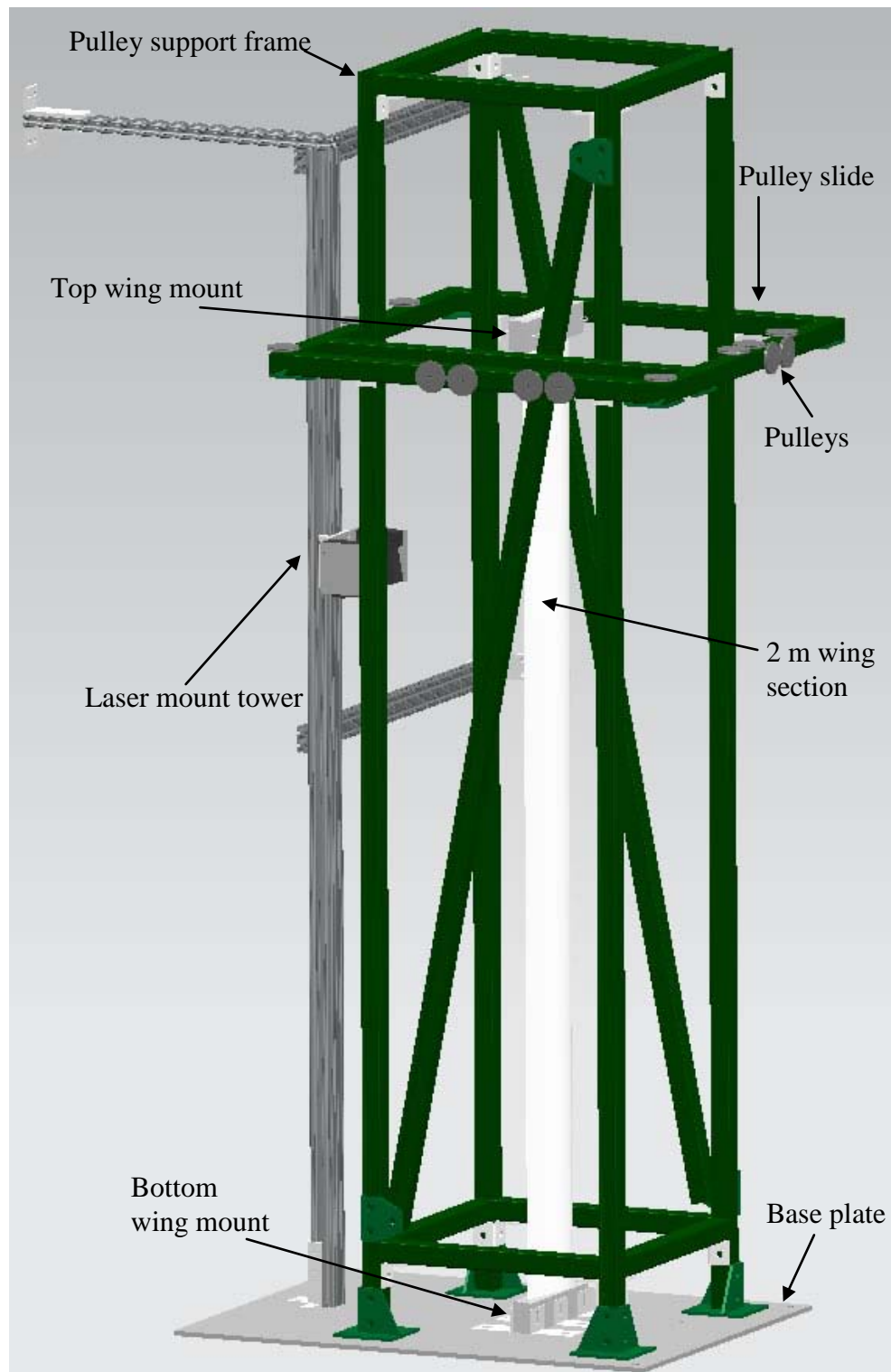


Figure 23. Test rig overview [20]

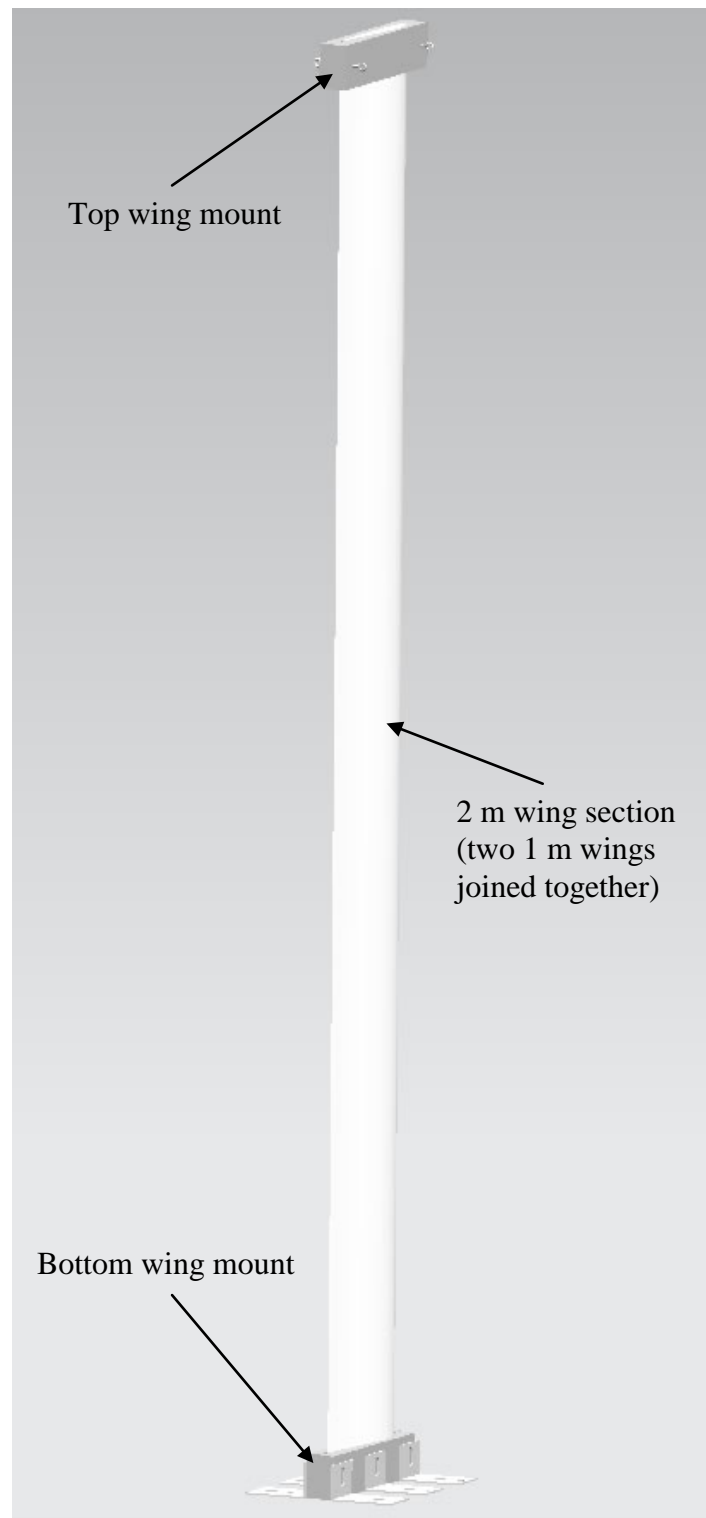


Figure 24. Wing mount assembly (showing 2 wings joined) [20]

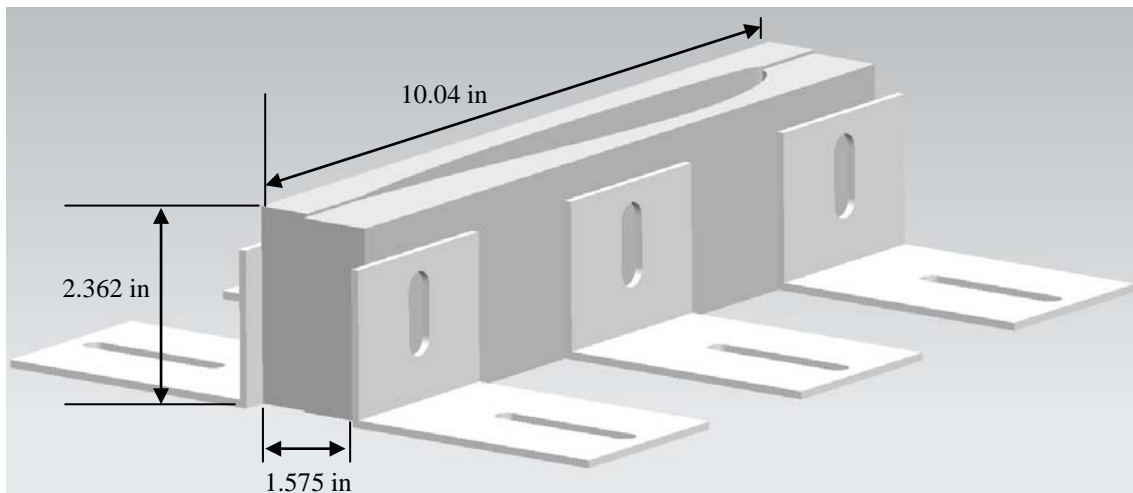


Figure 25. Bottom wing mount [20]

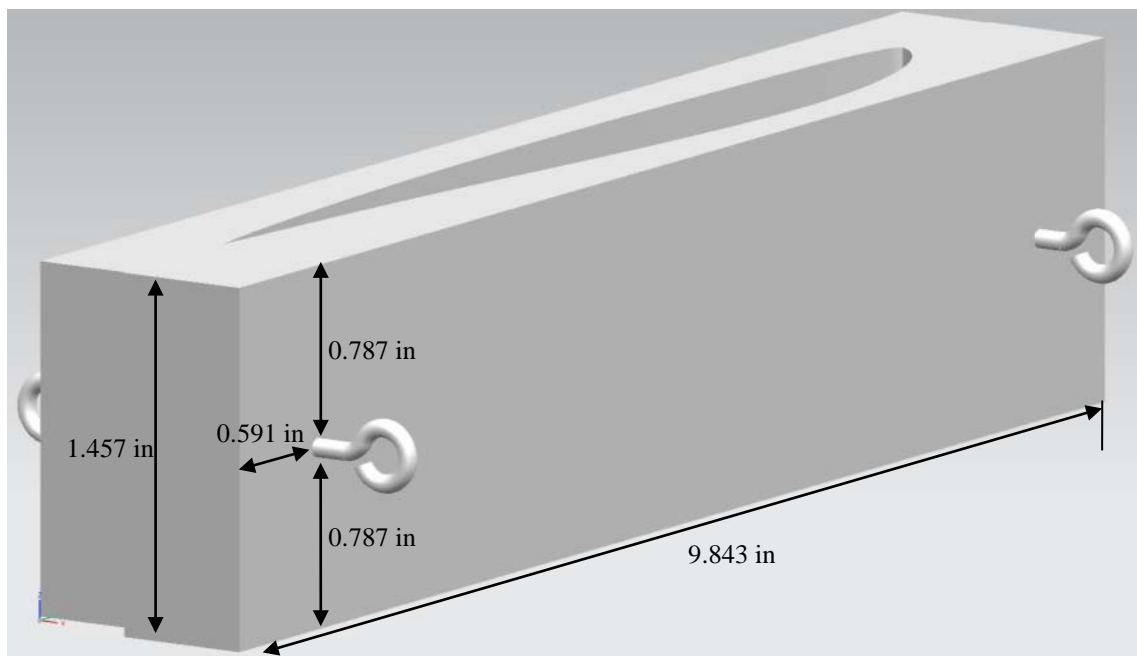


Figure 26. Top wing mount [20]

Stiffness Tests.

Four wing sections from X-HALE were subjected to bending and torsion tests utilizing the test rig. The wing sections were tested as single wing sections and as combinations of two wing sections joined together as they would be assembled in the complete aircraft. For the purposes of this research, only bending tests will be discussed. And although the wing sections were subjected to bending in both directions, this research only considered bending loads applied in the direction from the lower surface to the upper surface, or camber, of the airfoil. All wing sections, both single and joined sections, were subjected to applied loads of 3, 4, 5, 6, and 7 N. The bending stiffness, EI, was also calculated for each test section once results were collected. The progress report by Matthews describes in detail the test procedure and rig calibration, as well as summarizes the test results [21].

X-HALE Ground and Flight Testing

The main test plan for X-HALE was developed into two phases, with each phase employing two different aircraft – the FTV and the ATV, as previously mentioned. These aircraft will be structurally and aerodynamically identical, but will have minor internal differences. While the FTV will have a full housekeeping sensor package, it will include only an abbreviated science sensor package. Since its purpose is to study the aeroelastic behavior of X-HALE, the ATV will have additional electronic components including more extensive scientific instrumentation and an autopilot. To save weight, as well as time and funding required for construction, the FTV will not include these additional components. The FTV will be utilized for all Phase 1 testing and the ATV will

be reserved for Phase 2 of testing. The current version of the test plan pays specific attention only to Phase 1 [31]. Additional detail regarding ground and flight testing can be found in the Appendix.

Building X-HALE in a modular fashion allowed for flexibility in assembly and transportation. The aircraft can be transported as a whole or partial structure and assembled or disassembled as required. Construction and assembly at the University of Michigan was deemed the primary choice, as this will allow for maximum troubleshooting of any assembly-related issues. As such, the aircraft will be preassembled and transported from the University to the field test location as a full vehicle. Because the test plan requires testing of the 6-meter version before continuing with tests of the full 8-meter aircraft, X-HALE will be assembled into the 6-meter version and transported in one piece. The additional sections to make the 8-m FTV will be assembled in the field once the 6-m flight tests are completed. The X-HALE FTV, along with supplies, tools and ground equipment, will be transported by truck. A custom-made wooden box will be constructed to house the assembled vehicle and will be filled with Styrofoam packing material to cushion and help support the structure. The transport box will be approximately four ft wide, 20 ft long, and two ft high. The walls and floor of the box will be constructed from plywood sheets. Running the inner perimeter of the box at both the top and bottom will be 2-in. x 4-in. boards to support the overall container. As required, additional support spars will be added along the 4-ft dimension of the bottom surface of the box. The overall design and dimensions can be seen in the following diagrams (Figure 27 through Figure 29).

Initial ground and flights tests were expected to occur at Camp Atterbury, Indiana throughout the 2010 calendar year. Additional field test sites were also investigated to be used as weather backup locations. Schedule delays prevented any X-HALE field tests from taking place during 2010. However, the overarching details of the test plan remain unchanged, regardless of the eventual date of scheduled ground and flight tests.

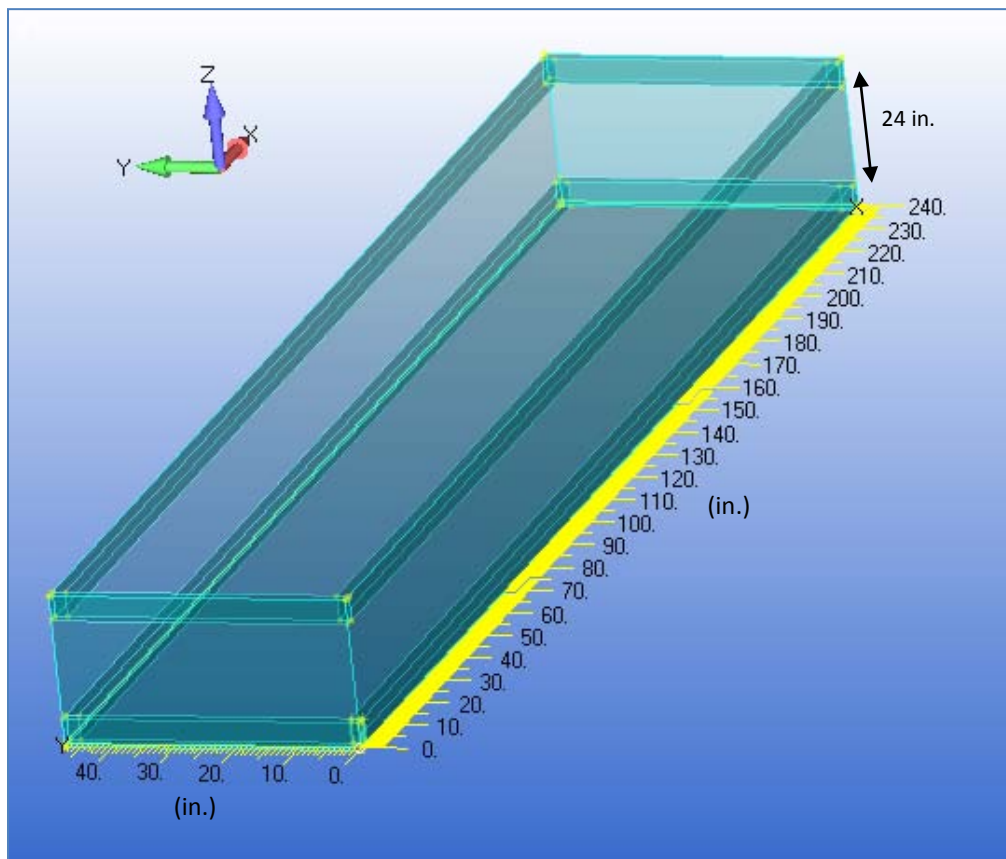


Figure 27. X-HALE Transport Box

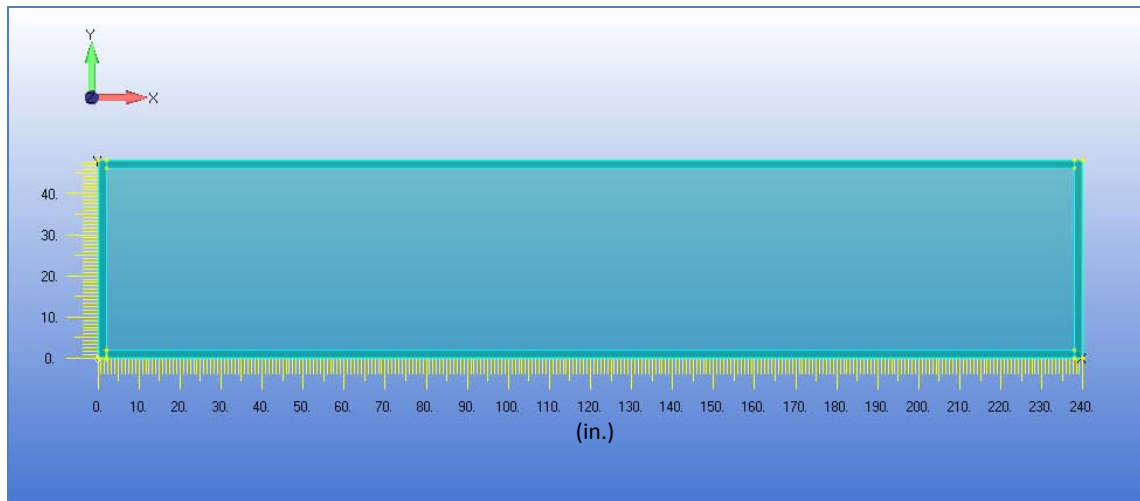


Figure 28. X-HALE Transport Box (Top View)

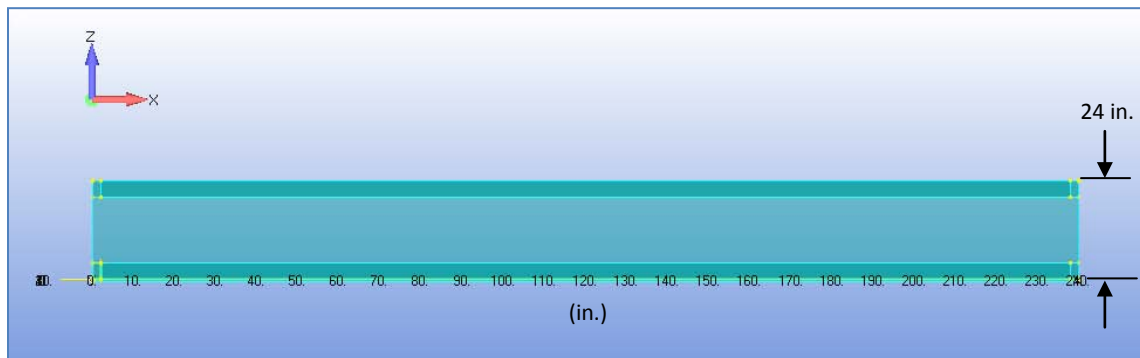


Figure 29. X-HALE Transport Box (Front View)

III. Methodology

As explained by Gosz, the FE method is a mathematical process for approximating the solutions to differential equations [16]. Conceptually, the method takes a mathematical problem and breaks it up into individual pieces referred to as nodes and elements. By discretizing the problem into these smaller parts, they can be treated as finite components and solutions to many smaller problems can be determined. The overall FE modeling procedure is most often divided into three phases: pre-processing, analysis, and post-processing. Gosz feels that the pre-processing phase is often the most difficult and time consuming of the three phases, and the amount of effort expended on this research effort would seem to confirm that suggestion.

Kim and Sankar present an overview of the core principles involved in developing and using FE programs [19]. They highlight that once a system is divided into finite elements, it is the focus of FE analysis to determine the behavior of each element, as well as its interaction with other nearby elements. These elemental behaviors are then translated into an approximation of the global behavior of the entire system. A key principle here is that errors typically decrease as the problem is discretized further. As the number of elements are increased and their sizes are reduced, the overall solution for the system will converge and reach the true solution for the problem. This, of course, directly relates to computational cost and limits associated with arriving at such a problem.

This research was likely similar to the experiences of many engineers in industry, where the use of a finite element software tool can be at odds with the user's low level of

confidence in the many key aspects of the problem at hand, such as the overall assumptions made, how the boundary conditions are defined, and what metrics of failure are to be used. As more time was spent working with the FE program, assumptions were refined and boundary conditions were described with greater detail. The importance of correctly defining material properties was also realized throughout this effort. Many of these realizations occurred after acquiring results and evaluating whether or not boundary conditions had been satisfied, whether the FE mesh was refined sufficiently, if the starting assumptions were made correctly, and whether a more complicated model and analysis were needed.

FEMAP Uses and Limitations

Finite element models created for this research were built and tested using FEMAP, a Siemens PLM Software product. An advantage of using a commercial FE tool such as FEMAP is the ease of utilizing previously created CAD-based geometry of the desired subject and the ability to conduct FE analysis on the whole or partial aircraft component as needed. Limitations of the software system included an education license which excluded some toolkits otherwise available with the program and prevented some modifications to FEMAP that could have increased productivity during this effort. Also, throughout this work several different versions of FEMAP were used. Reasons for this were that training material was initially available only for earlier versions of the software, while AFIT network functionality prevented all but the most recent version of FEMAP from successfully integrating post-processing results.

An incremental process was followed throughout the modeling effort of this research. This step-by-step method allowed starting with significantly simplified versions of the components to be analyzed before moving on to more complex and detailed representations of the structures. There are several benefits to using such a process to develop a model, prime among them being the likelihood that mistakes are often caught earlier than they would have been otherwise. Starting with simplified models often allows the user to more readily test the validity of assumptions, whether the boundary conditions were correctly defined, and whether the selected solver will provide the desired results. Incremental model development usually means less time and effort is spent overall as compared to a process in which the user attempts to develop a more complicated model immediately.

Modeling Process

Computational cost of analysis for this effort did not become an issue. For further FE analysis beyond the modeling effort conducted in this research, the computational requirement will likely increase significantly. The subject of units was recognized early as both important and likely to cause errors. Both SI and English units were used during much of the testing and physical design of X-HALE, so care was taken to remain consistent during the FE analysis process.

Modeling work within FEMAP began with the original CAD models of the parts of X-HALE to be analyzed. CAD files of the complete wing section and joiner block were obtained from the University of Michigan. These models were then imported into

FEMAP as solid geometry and would form the reference foundation for the development of the finite element models.

Two distinct FE modeling efforts will be discussed here. The first is focused on the University of Michigan's three-point bending test conducted early in X-HALE's design and construction effort. At the time it was conducted, this bending test was the only major lab test performed on a significant structural X-HALE component for which appreciable data had been collected. The point in time at which the test had been completed and the organization of its data served as an appropriate test subject with which to work in relation to this research. Subsequent FE modeling and analysis focused on the later bending tests conducted in the University of Michigan's bending and torsion test rig.

Three-point Bending Test

As described in detail previously, the entire X-HALE aircraft is comprised of eight one-meter long wing sections joined together at seven joints (Figure 9 and Figure 10). The inner five joint sections, where airfoils are joined to the five inner motor fairings, are identical and are representative of the wing joint section that was subjected to bending loads. The first assumption made was to neglect the motor fairing from the joint, since this was not included in the test. Because the joiner sleeve is not glued to the wing, but rather intended to transfer torsional loads between wing sections through the joint, the sleeve geometry was also neglected and two wing section models were simply connected together along their edge.

First, the original CAD geometry of a complete X-HALE wing created by the University of Michigan was imported into FEMAP. The geometry included all details of the wing that were to be constructed of fiberglass, foam, and carbon fiber materials. No sensors or wires were included in the geometry. A Cartesian coordinate system was defined about the model such that the positive X direction is along the wing chord out the trailing edge of the wing, the positive Y direction is out to top of the wing surface normal to the chord line and parallel to the direction of the applied load of the test rig, and the positive Z direction is out the aircraft's left wing along the span of the wing section (see Figure 31). For the purposes of creating an FE model, the original CAD geometry was overly complex to use directly, especially for the beginning steps of the incremental process. Some simplification of the model was required to begin the meshing process. The carbon IM7 layers within the airfoil and wing box sections were neglected to simplify the model. Although it would later be added back into the FE model, the foam core of the airfoil and wing box was not included during the initial analysis because it was assumed the foam provided only minimal additional stiffness. This left the initial model consisting of two hollow 1-m (39.37-in.) span airfoils, wrapped around hollow wing boxes, connected together by sliding the inner end of the wing boxes over a 2.5-in. long wooden joiner block (Figure 30).

To remain consistent with the bending test that was conducted, and to further simplify the model, it was assumed the joined wing section would only move in the positive or negative Y (along the direction of the applied load) and Z (span-wise) directions. And although the bending test was conducted at cycles of +20 lb / -10 lb loads at a ± 0.15 in./min loading rate, the model would be subjected to single, incremental

loads corresponding to each of the maximum loads applied for each cycle during the test – 20, 30, 40, 50, and 60 lbs respectively.

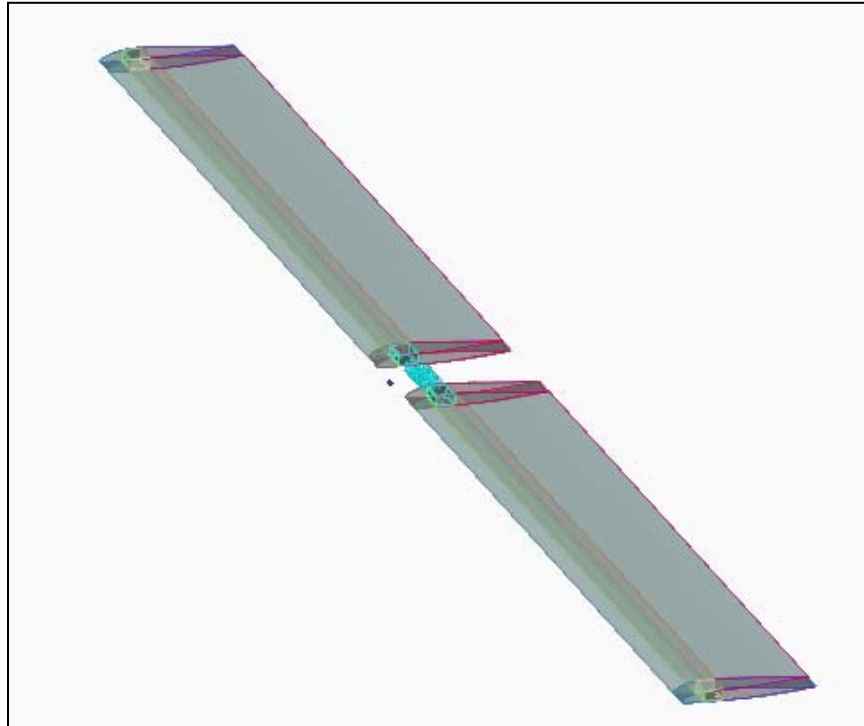


Figure 30. CAD model of 2 wing section and joiner block (separated apart)

The FE modeling and analysis process resulted in the creation of eight relatively distinct models, which are summarized in Table 1. All variations made to higher numbered models generally include characteristics from the previous model unless explicitly stated otherwise in the following sections. An example of this is the inclusion of the contact problem between elements of the joiner block and the inside of the wing box, which was only utilized in Model 5 and will be discussed in detail later.

Table 1. Summary of FE models and descriptions

Model 1	Single 2m Wing Box section with pinned roller constraints
Model 2	Single 2m Wing Box section with fixed X & Y constraints
Model 3	Two 1m Wing Box sections with a wood joiner bolted to the wing box
Model 4	Two 1m Wing Box sections with foam added to wing box
Model 5	Two 1m Wing Box sections with contacts between the joiner block and wing box
Model 6	Two 1m Wing Box sections with airfoil added
Model 7	Single 2m Airfoil section with foam core added to airfoil
Model 8	Two 1m Airfoil sections

Simplifying Assumptions.

Although Model 8 most closely mimicked the actual 2-m wing structure used in the three-point bending test, many assumptions were applied that simplified the modeling process. The method of connecting the wing section to the joiner block by simply merging the coincident nodes of the structures to simulate the screws used to hold them together likely caused the model to be stiffer than the test article. Fastening the wing sections to the relatively soft wooden joiner likely resulted in noticeable movement between the two wing sections at the locations of the screws, movement which would not be allowed by merging coincident nodes. Additionally, working contact definitions between the wing box and joiner block were not successfully employed in Models 7 or 8. As this was shown to have a significant impact on the deflection results (compare Models 4 and 5), not including these boundary conditions must be noted.

Basic assumptions were also made regarding the mass and material properties which may or may not be invalid. The gravitational acceleration of the wing assembly was simply neglected, which immediately removed a degree of reality from the model.

However, the gravitational force on the wing of such a small composite structure was assumed to be orders of magnitude less than the applied loading. For the static analysis performed, this assumption likely had negligible affects. On the other hand, the material properties of the composites (as published by their manufacturer) were used were in the model definitions [4, 6]. How they compared to the true properties of the assembled materials is unknown. The layup technique employed during fabrication of the wings may have resulted in properties varying significantly from their published values. Finally, while the carbon fiber reinforcements to the joint sections of the wings only consisted of a small fraction of the wing, neglecting this material also resulted in material properties of the assembled wing which differed from that of the test section, likely causing the model to be slightly more flexible than the actual physical structure.

As the FE model of the joined wing sections evolved from Model 1 to Model 8, the simplifying assumptions applied were systematically removed. The joiner block was added at the joint inside the wing box (Models 3 – 8) and the wing sections were split into two separate pieces. The foam core was then added back to the wing box. Finally, the airfoil was reintroduced and the foam was included within the airfoil sections. Each change brought the model closer to the test article. However, as will be discussed in the following sections, as more of the wing section structure was added back to the model the results diverged from those of the actual bending test.

Loads and Boundary Conditions.

The loading and boundary conditions for the test case were relatively straightforward. Loads and constraints were applied to the model only at nodes of the wing box

section. While this may not truly represent the setup of the bending test, it should not introduce significant errors in the vertical deflection of the wing box.

Loads.

Loads simulating those from the wing joint bending test were applied to the center joint section of the model. Specifically, for each loading case (20, 30, 40, 50, and 60 lbs) the total load was divided into 3 point loads that were then placed onto nodes along the centerline of the joined wings. Depending on the version of the FE model, the nodal loads were applied to different part of the wing joint. When the model only consisted of the wing box, the loads were applied to the top nodes of the wing box mesh at the centerline. When the model included the basswood joiner, the loads were applied to the top centerline nodes of the solid joiner mesh.

Boundary conditions.

In the laboratory bending test the joined wing section was supported by two rollers, one under each airfoil approximately 0.25 m from the center of the wing joint. Constraints were defined under each airfoil section at these locations to model the rollers. Multiple constraint types were utilized. Initially, pinned constraints were applied to the wing box at the roller positions (Model 1 from Table 1). All subsequent models were constrained in the X (chord-wise) and Y (vertical) directions at the rollers and in the X and Z (span-wise) directions at the center of the joint by placing three nodal constraints along the bottom surface of the model at those locations. The joint constraint ensured the center of the model would displace only in the direction of the applied load. No rotations were constrained. The locations of these constraints are shown in Figure 31 and Figure 32 by red triangles.

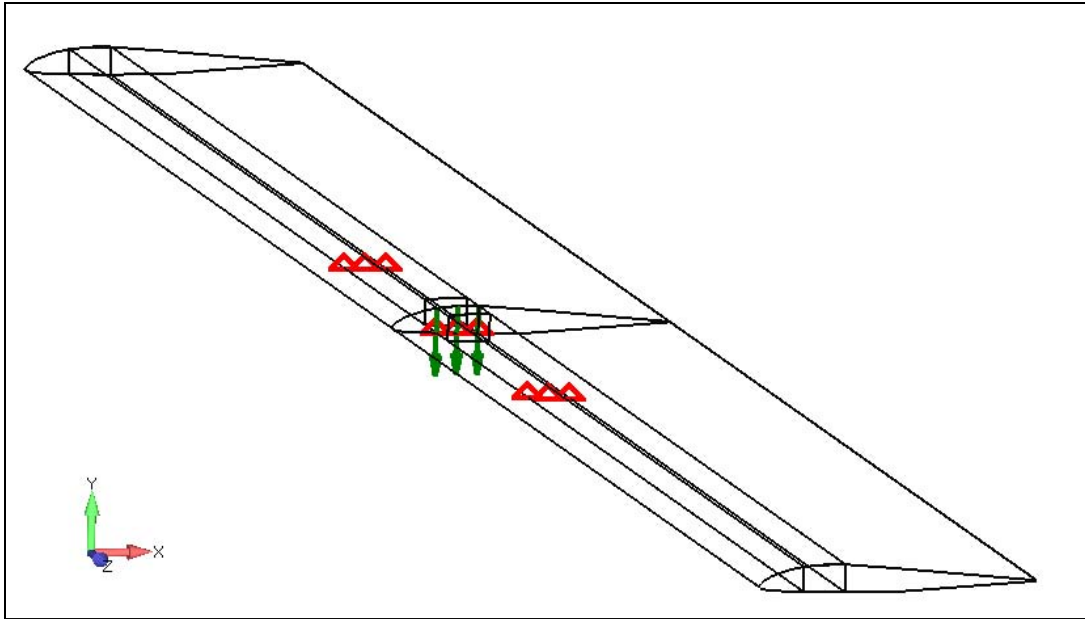


Figure 31. FE model constraints indicated by red triangles

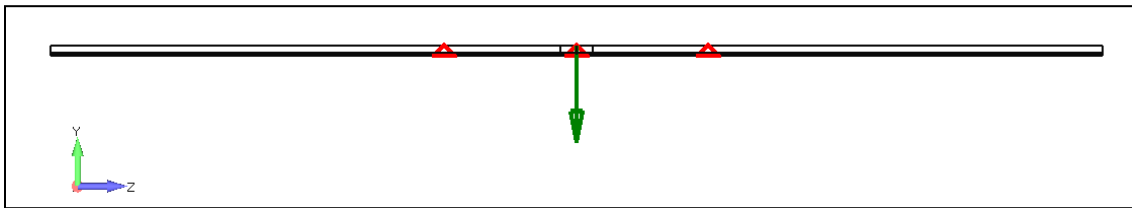


Figure 32. FE model constraints indicated by red triangles (front view)

FE meshes.

To begin the FE analysis, the X-HALE wing joint was initially simplified further. The assumption was made that the wing box provides the majority of stiffness to the overall wingspan and, for this reason, the actual airfoil was neglected. While building the initial FE models, the joiner block was also not included to allow the users to become comfortable working in FEMAP with as simple a model as possible. These models were

created as single 2-m structures without the complication of a connecting piece. The wing box was initially modeled using simple beam elements. By defining the beam cross section to be that of the wing box, or close to it, the beam elements would be a simple and efficient model of the wing span in a bending scenario such as this test. A subsequent iteration for the beam element mesh combined the airfoil with the wing box into one entity – that combined cross section, defined to be the shape of both the wing box and airfoil, was then meshed again using beam elements (see Figure 33). This seemed to be a good approach to mate the airfoil and wing box together while keeping the types of elements to be worked with minimal. This beam element type of model was accepted as a good first attempt at FE analysis within FEMAP but was discarded for more robust models. The beam element model was also discarded due to difficulty encountered when pairing beam and solid elements. Anticipating the use of solid elements to model the joiner block, beam elements were not used beyond these initial FEMAP models.

The next approach was to mesh the wing box using plate elements. The starting geometry remained the same as above, with the foam, airfoil, and joiner block geometry ignored, and analysis was conducted on the wing box alone (Figure 34). Furthermore, the initial analysis assumed a single wing box the length of two wing sections, as indicated in Models 1 and 2 from Table 1. Model 3 was the first iteration where the wing box was divided into two 1-m sections and the basswood joiner was added. The wing box was still meshed with the same plate elements, but “unzipped” in the center so there were two coincident nodes at each location along the joint centerline.

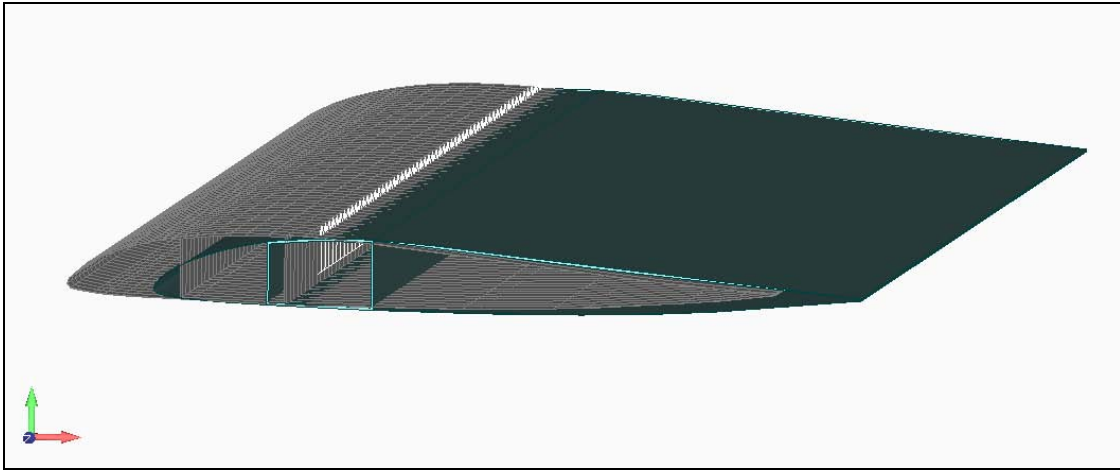


Figure 33. Overlapping wing box and airfoil geometry and mesh

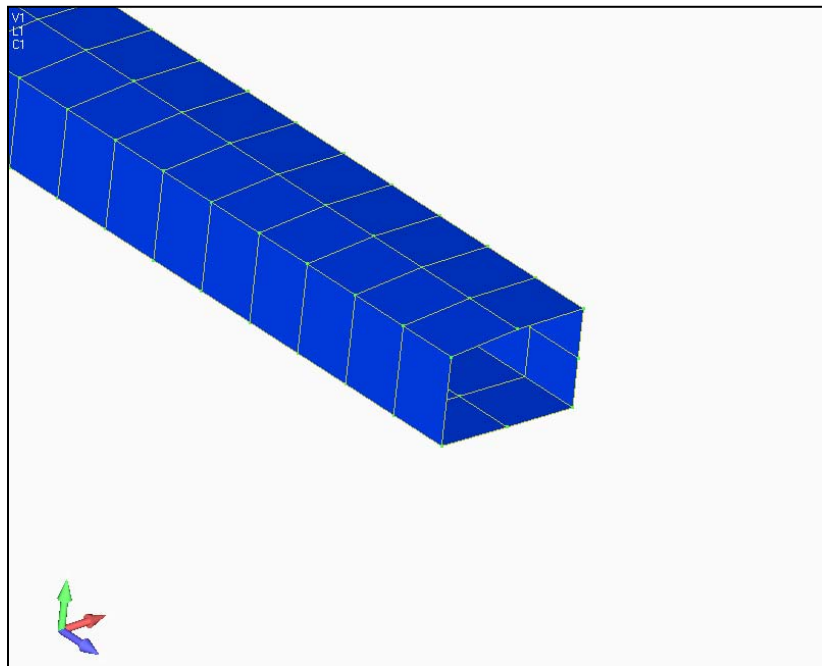


Figure 34. End of wing box model (only fiberglass wing box remains)

One method to "unzip" the wing box model utilized FEMAP's included "Unzip..." command, which is under the Mesh menu and the Connect submenu. The appropriate elements and nodes were then selected, and the desired connections were

selected within the Generate Connection Options dialogue box. To completely free the two portions of the model, None was selected as the connection type. Additionally, an effective method to "unzip" the center joint of the 2-m wing box model was to revert back to an earlier version of the model, before the coincident nodes at the center were merged, and leave them unmerged. Although the appearance of the model did not change, the number of nodes increased and the two 1-m sections of wing box were now separate structures. The basswood joiner was meshed as eight solid Hex elements. The properties of the basswood were assumed to be equal to those for commonly published woods [26]. During the laboratory test the joiner was secured to the structure with two vertical screws through the airfoil, wing box, and wood. In the FE model the wood-screw connections were simulated by merging the nodes where the screws were located on the joiner and wing box. In Figure 35, the merged nodes at the location of the screw connections are can be seen as the areas of higher stress concentration (lighter blue and green colors).

Model 4 used the same mesh as Model 3, except the Rohacell Foam was added into the wing box. Hex Solids were created from the geometry of the wing box to fill the space not already taken up by the wood joiner in the middle. The solid elements were defined with the same spanwise sizing as the plate elements (0.625 in.) so that the nodes of the wing box wall and the foam aligned. Once the foam mesh was created all the nodes within each 1-m sections were merged to model the epoxy between the foam and the fiberglass. The model now consisted of three materials: the fiberglass wing box modeled with plate elements, the basswood joiner block modeled with solid elements, and the foam core modeled with solid elements inside the rest of the wing box.

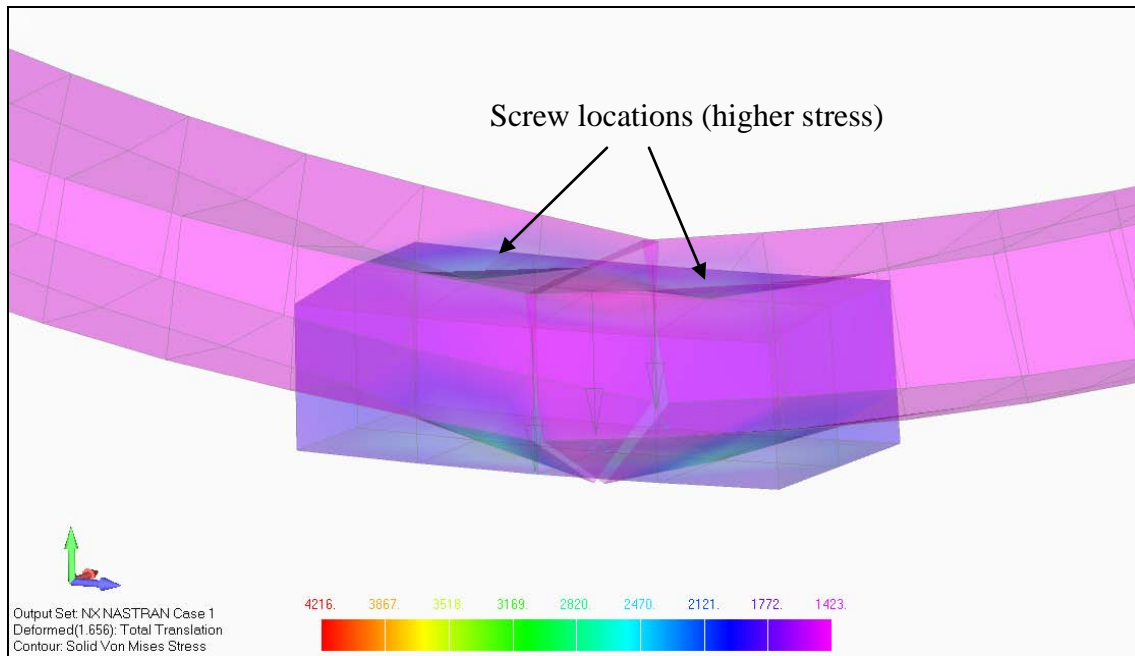


Figure 35. Model 3 deformed showing wooden joiner block inside wing box

Contact Problem.

A task of noteworthy difficulty encountered during the modeling process was that of the contact problem between the wooden joiner block and the inside of the wing box. In the actual wing, the wood essentially rested inside the otherwise hollow wing box and was only connected to the wing box by the two screws. This was repeated in the model by only merging the coincident nodes of the joiner block and wing box at the locations of the two screws, which in this case were individual points. When the FE analysis of the applied loading was performed and the model deformed, the outer solid elements of the basswood joiner protruded through the bent plate elements of the wing box (Figure 36). Obviously this did not occur during the lab test, but rather was a result of poor boundary conditions.

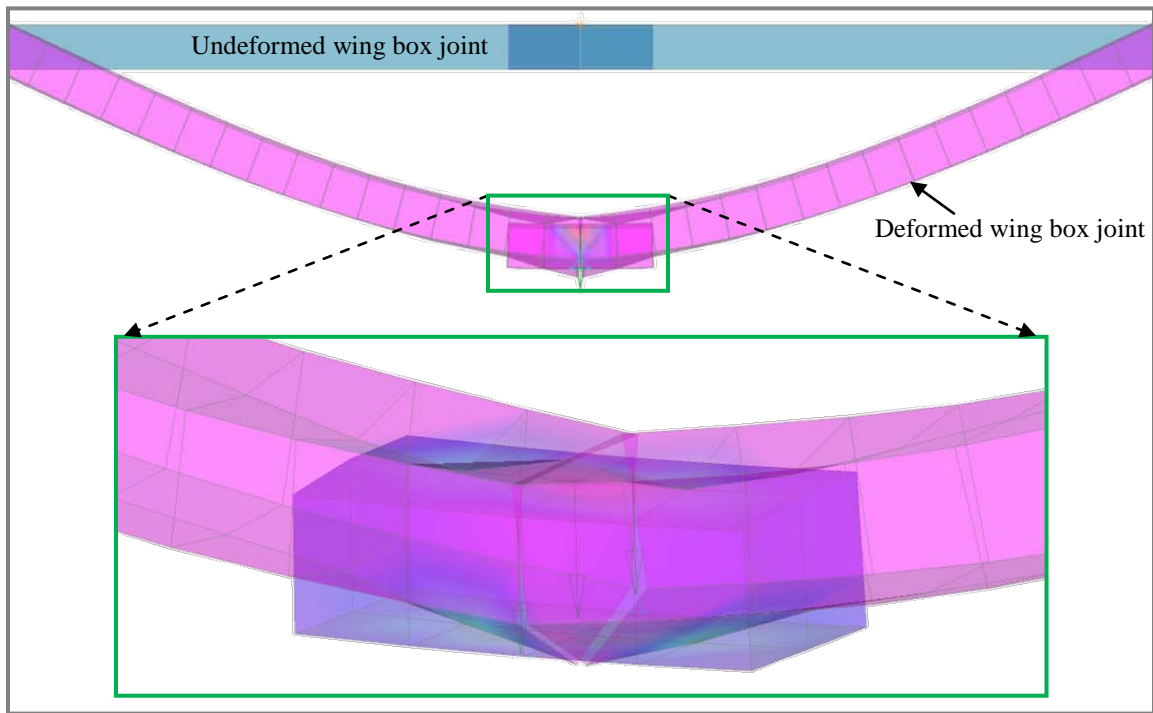


Figure 36. Wing box joint without contact surfaces defined showing protruding joiner (with close-up detail of joiner block)

To investigate this contact problem, a simple model of two cantilever square beams was created. Both beams were fixed at opposite ends, with one beam resting on the other. Finally, a load was applied to the free end of the top beam. However, without properly defining and/or activating a connector, when analysis of the model was performed the top beam deformed through the bottom beam (shown in Figure 37 by the blue transparent geometry of the original position and the deflected gray elements). While the method to solve this unrealistic behavior was not difficult, several steps were required to create a working contact problem. The following technique outlines the process used to model the physical contact of two surfaces for this research.

Within the Connections function of FEMAP, the following steps were taken:

1. A Connection Property was defined, with the following settings:
 - a. Connect Type was set to 0.Contact
 - b. Friction was set to 1
 - c. Min Contact Search Dist was set to 0
 - d. Max Contact Search Dist was set sufficiently high
 - e. Min Contact Percentage was left at 0
 - f. Initial Penetration was set to 3.Zero Gap/Penetration
2. Two Connection Regions were selected, with the following settings:
 - a. Type was set as Deformable
 - b. Output set to Elements
 - c. Defined By set to Surfaces
 - d. One region was defined for each beam – the bottom surface of the top beam and the top surface of the bottom beam.
3. A Contact Connector was defined. Within the Contact Connector definition the two previously defined Connection Regions were selected. The Connection Property defined above was selected as the property. One region was set as the Master and the other as the Slave.

Finally, the connector was Enabled by right-clicking its title in the Model Info window.

When analysis was again performed, this time the cantilever test model deformed as one would expect – the surfaces in contact deflected together, causing the bottom beam to also deflect (Figure 38).

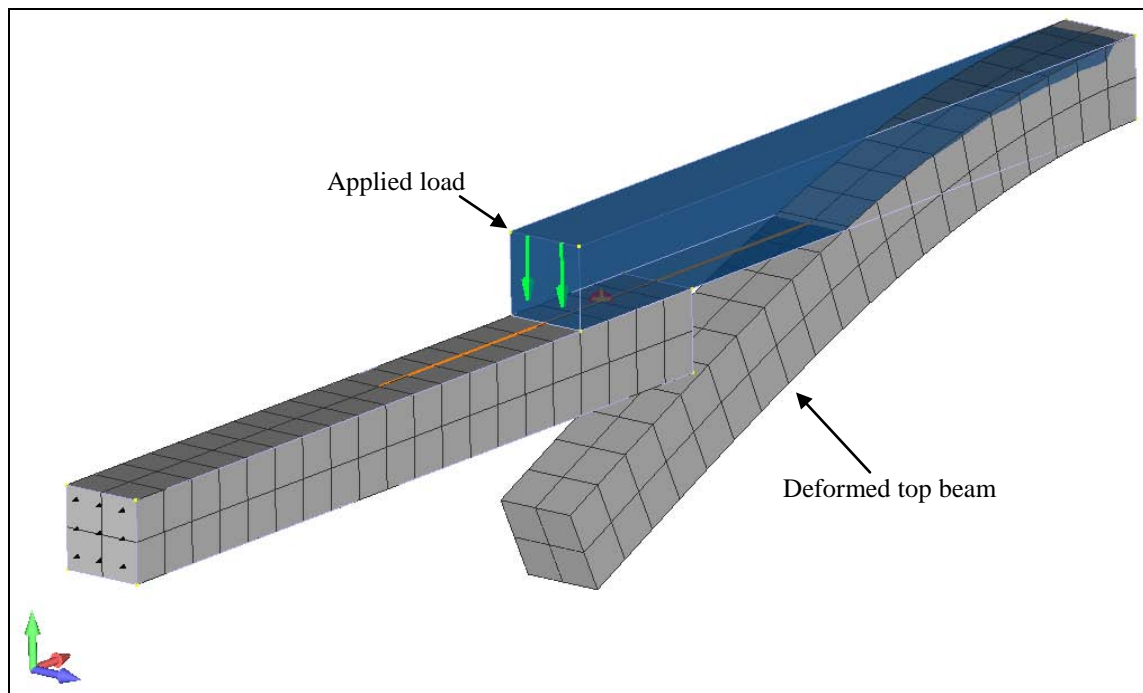


Figure 37. Cantilever Test Model, Contact Surfaces NOT Activated

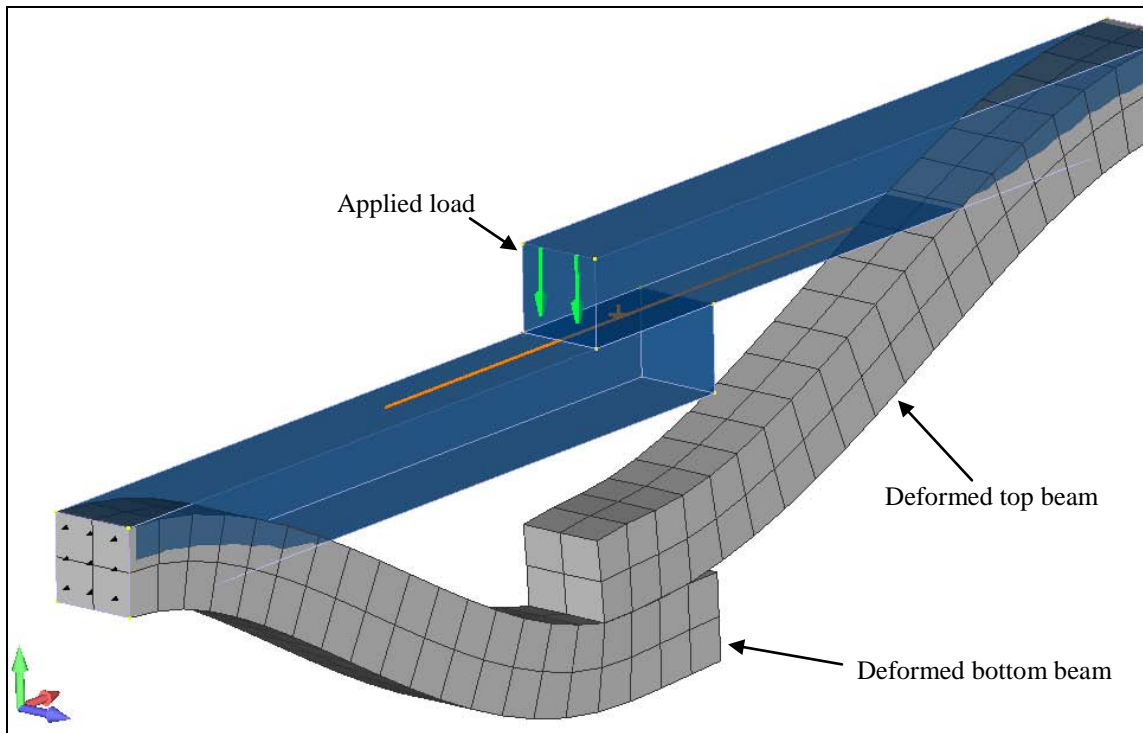


Figure 38. Successful Contact Test

After successfully testing the contact problem with the simple cantilever model, these steps were utilized for the final iteration of the simplified wing box model by adding contact connections between the wing box and joiner block, which became Model 5 (and the only model which utilized contacts). Two specific sets of connection regions were defined – the top surfaces of the wing box and the top surface of the joiner block; and the bottom surface of the of the wooden joiner and bottom surfaces of the wing box. These surfaces can be seen as the areas highlighted in yellow in the following series of figures. These figures depict the plate and solid elements along the entire span of the combined wing box and joiner model. The model is shown with transparent entities, allowing the solid elements of the joiner block to be visible inside the two sections of wing box.

By defining contact surfaces in FEMAP, contact properties can then be selected for the desired problem. The contact properties here were defined to prevent the solid joiner block from passing through the upper or lower walls of the wing box. Similarly, two connectors were defined and enabled. However, a successful analysis was only completed by selecting "22.Advanced Nonlinear Static" as the Analysis Type within the analysis sets. Finally, the deformed model resulted in the joiner block remaining inside the wing box (Figure 43).

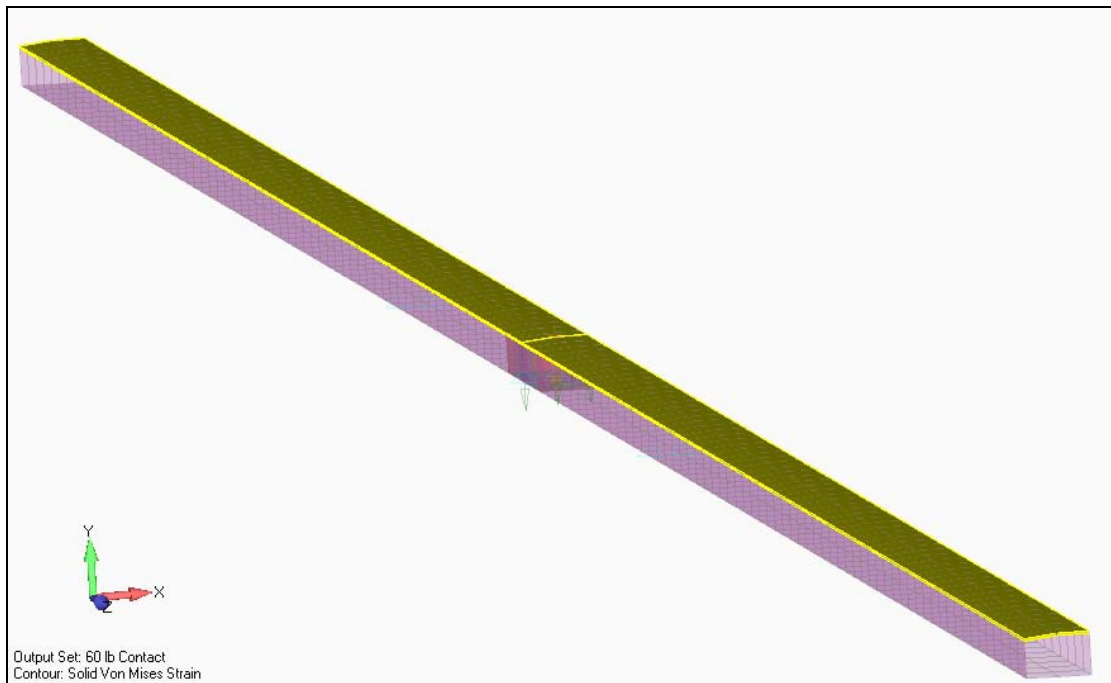


Figure 39. Joined wing box model showing top wing box surfaces highlighted

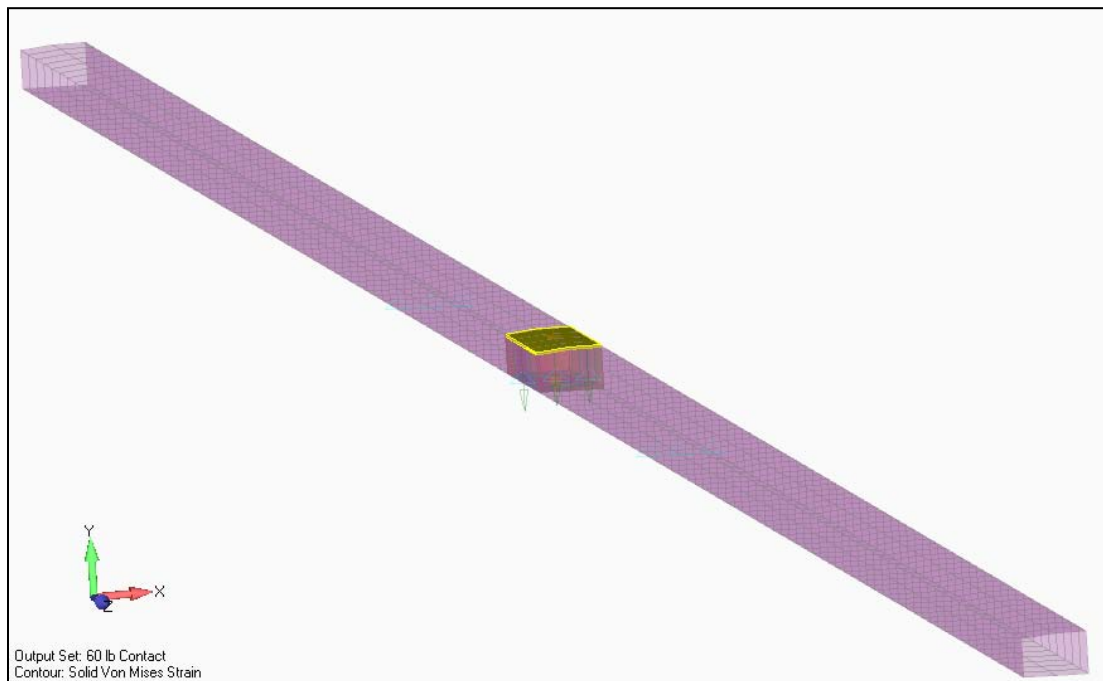


Figure 40. Joined wing box model showing top joiner block surface highlighted

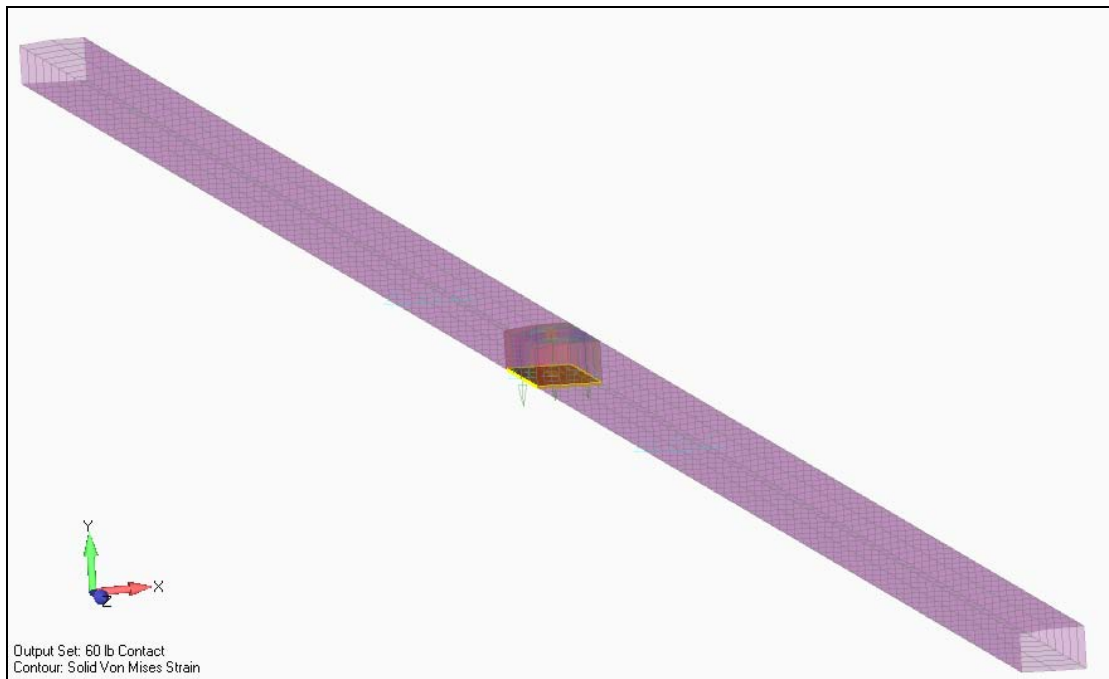


Figure 41. Joined wing box model showing bottom joiner block surface highlighted

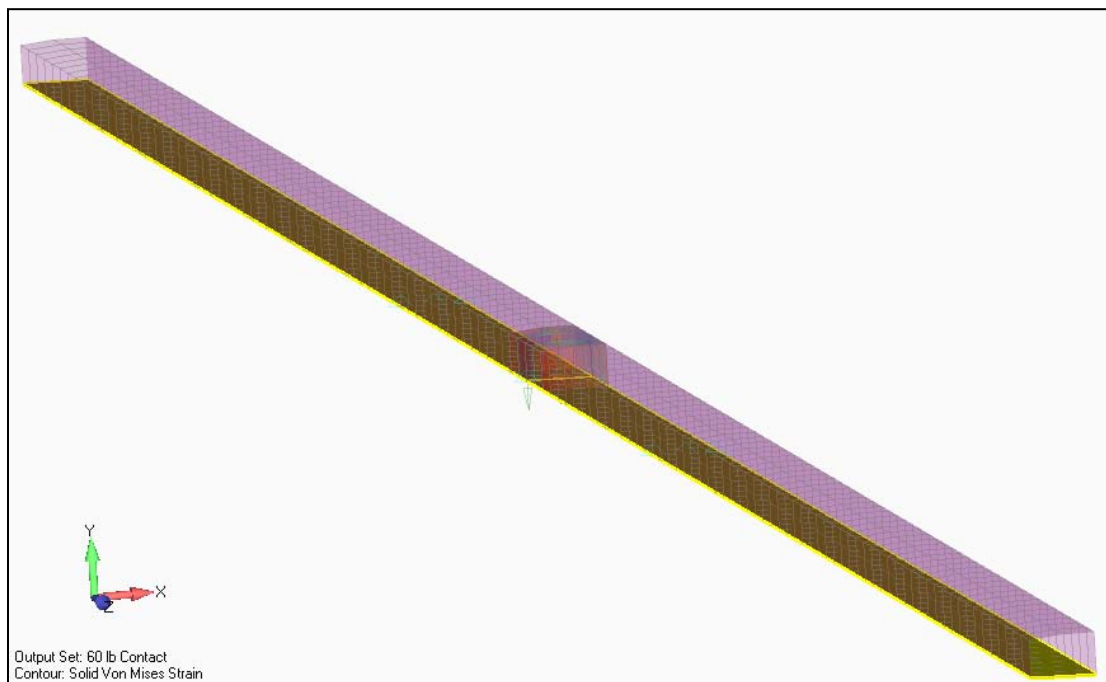


Figure 42. Joined wing box model showing bottom wing box surfaces highlighted

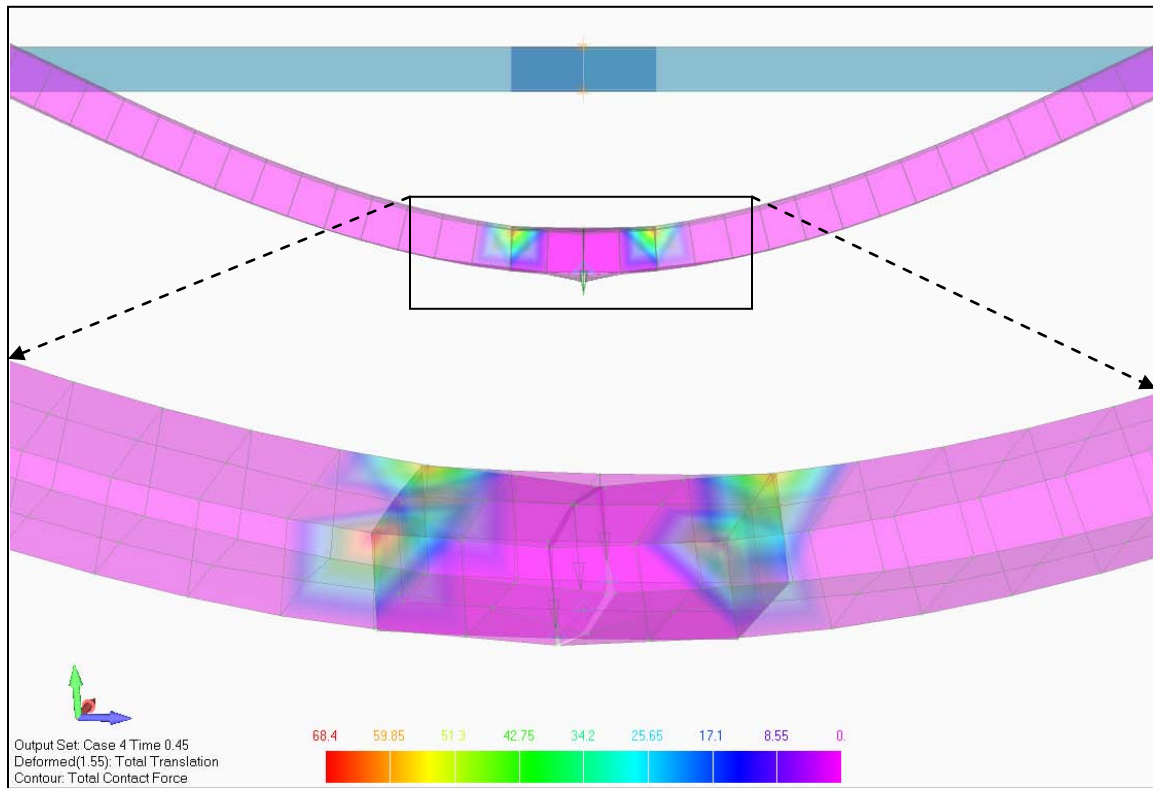


Figure 43. Wing box joint with contact surfaces defined showing resulting contact forces (detail of Model 5, color contours show contact force)

After progressing through five iterations of the simplified wing box model (Models 1 – 5), the airfoil structure was reintroduced. For the purposes of aligning portions of the airfoil with the previously developed wing box, it was determined easiest to divide the geometry of each wing section into six different pieces. For both the top and the bottom wing surface, the airfoil was separated into a leading edge, a wing box, and a trailing edge portion. The leading edge surface consisted of that portion of the wing surface forward of the wing box. Likewise, the trailing edge surface consisted of the portion of wing surface aft of the wing box. The wing box portion of the wing surface corresponded to the chordwise section of the airfoil that existed between the

forward and aft walls of the wing box. Once the geometry was broken up, each section was then meshed separately with plate elements spaced 0.625 in. apart (spanwise) so nodes between the different pieces of geometry would be coincident. Once meshed, all coincident nodes were merged. Utilizing his method makes the assumption that during fabrication of the wing section the fiberglass of the airfoil was perfectly connected to the wing box. However, since they were constructed at different times and due to the layup method used, it was realized that this assumption was not absolutely accurate. Ultimately, this degree of error was assumed to be acceptably small.

As with the creation of the wing box, development of the airfoil portion of the model began without taking into account the Rohacell foam. This was because of the assumption that the foam did not provide very much stiffness. While this would be shown to be relatively accurate, undesirable behavior of the wing model resulted when the airfoil was modeled as a hollow structure. Specifically, the airfoil portion of the wing model deformed in a fluid and wave-like manner, as seen in the depiction of Model 6 in Figure 44.

To prevent the unrealistic deformations observed in Model 6, the solid foam was added back inside the remaining open space of the model. Two variants of this more complete model were created – one consisting of a single piece of wing spanning the full 2 m (Model 7) and one consisting of two separate 1-m wing sections joined only by the wooden joiner block inside the wing box (Model 8). Because the solid foam geometry of the original CAD files did not fit well within the airfoil mesh, the solid elements of the foam mesh were created manually. First, elements along the chord line at the outer edge of the wing were created. Then, the elements and nodes were copied down the remaining

2-m length of wing span. The elements along the trailing and leading edges – those at the very leading edge and trailing edge of the wing – were created as wedge elements, while the rest of the solid elements within the chord of the airfoil were box elements. Finally, the coincident nodes of each wing section were merged to make each wing section an integral structure. In the case of Model 7, all coincident nodes of the wing structure (other than the joiner block) were merged, causing the model to exist as a single piece. In contrast, there remained coincident nodes along the joint chord line of Model 8 where the two wing sections came together. This more realistically simulated the actual assembly of the wing structure in the three-point bending test, which in turn made Model 8 a more realistically representative model of the joined test section than the preceding versions.

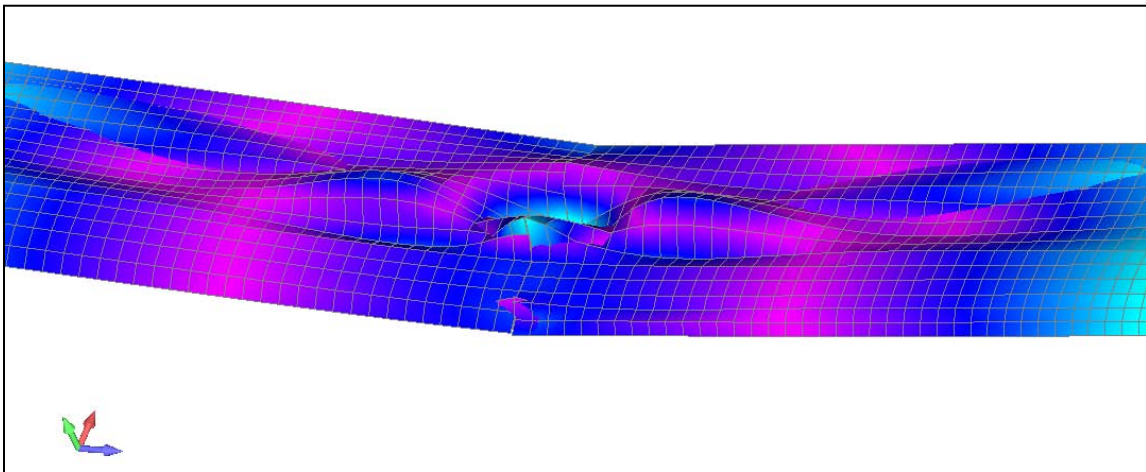


Figure 44. Deformed geometry (Model 6) with no foam in the airfoil

Lessons Learned.

Beyond discovering the procedures for defining contact surfaces between parts of the model, many lessons were learned for effective methods of performing all levels of tasks within the FE modeling process. An issue encountered early on in this effort dealt with coincident nodes. There were many instances when meshing geometry resulted in end nodes farther apart than the default value of 0.008 in. For example, the bottom and top section of the trailing edge of the airfoil were approximately 0.023 in. apart. This produced some unrealistic performance in the airfoil (see Figure 45) where the upper and lower surfaces separated at the trailing edge and deformed individually. To avoid these kinds of results, the tolerance for coincident node checks needed to be noted and adjusted as necessary.

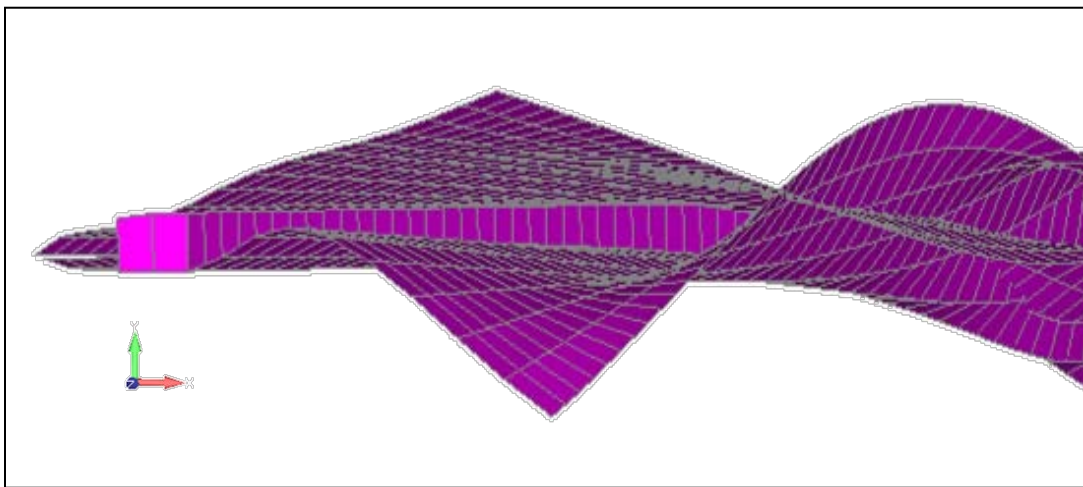


Figure 45. Behavior resulting from trailing edge mesh separation

Another issue encountered involved unzipping nodes, which was briefly mentioned previously. Without a full understanding of the model, this function can be difficult. When attempting to reassign nodes to two or more separate meshes it was often easier to redo a mesh or series of meshes than to unzip nodes. For example, the first time the foam was added to the airfoil it seemed easiest to merge all coincident nodes and then unzip the wing joint center line to reacquire two separate wing sections. However, the unzipping process produced additional nodes along each wing edge. It was very difficult to determine to which element the “new” nodes were assigned. In this case, the first analysis after unzipping resulted in zero deformation of the structure because the nodes where the force was applied were not connected to any elements. After this failed attempt to unzip the nodes along the centerline of the two wing sections, the entire mesh was deleted and reconstructed. It was often advantageous to construct the elements of a model by hand, such as in the procedure used when foam needed to be added to the structure to stop the strange deformations of the airfoil. Construction by hand ensured nodes of different mesh types actually line up. It was simpler and faster to match the nodes by hand and copy the elements rather than attempt to control the size of elements through the mesh control menu.

Another lesson learned was that the color of portions of the model change within FEMAP to indicate the number of elements at a particular location. This could easily be interpreted as a graphical error or attributed to a missed step while creating the model. Instead, it usually represents a clue pointing towards an unusual or undesired condition within the model. The following figures show the graphical difference between a doubled element at the leading edge (which appears transparent) and the correct condition

of a single element (colored green like the other similar elements). The wedge element at the leading edge appears to be missing (Figure 46), but the selection shows it is actually present, as indicated by the circle. Test runs with this model were asymmetric; the side of the wing with overlapping duplicate elements deflected less than the side with the correct elements. Further inspection revealed the overlap, with some plate elements being repeated as many as three times. Figure 47 shows the leading edge after the extra element was deleted. In this case the overlapping elements were probably the result of the copying procedure used to create the foam elements. The selection was likely not cleared prior to copying a new selection, ultimately resulting in some elements being copied twice.

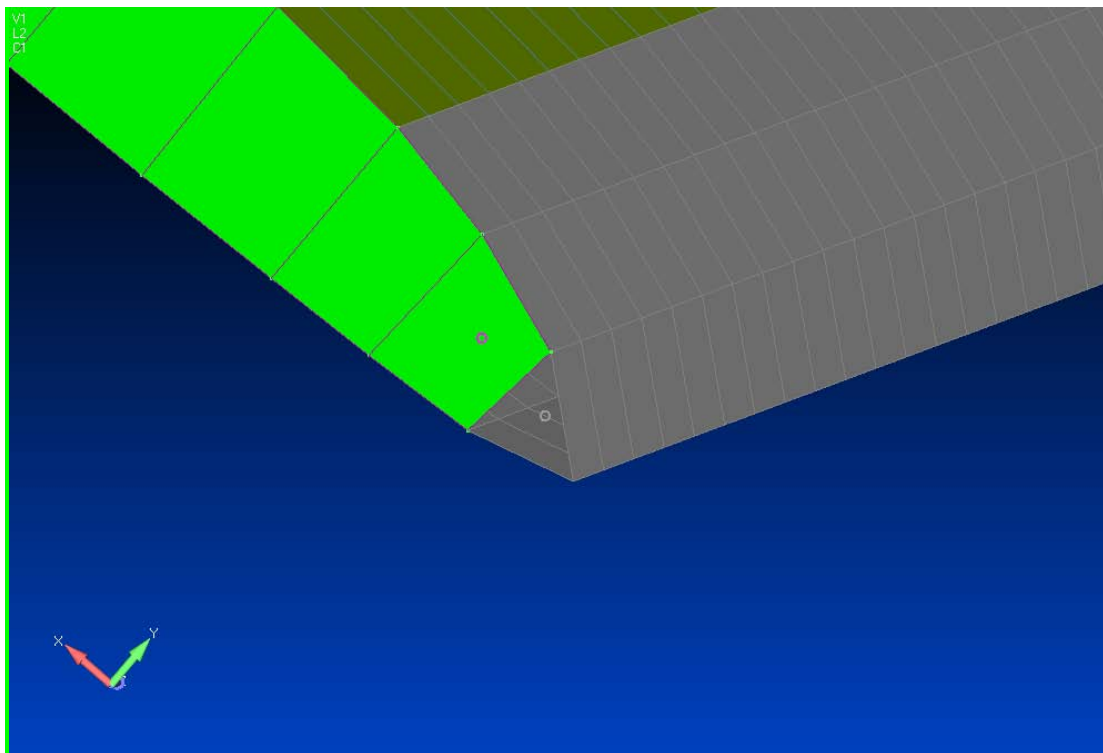


Figure 46. Overlapping foam elements at leading edge of wing

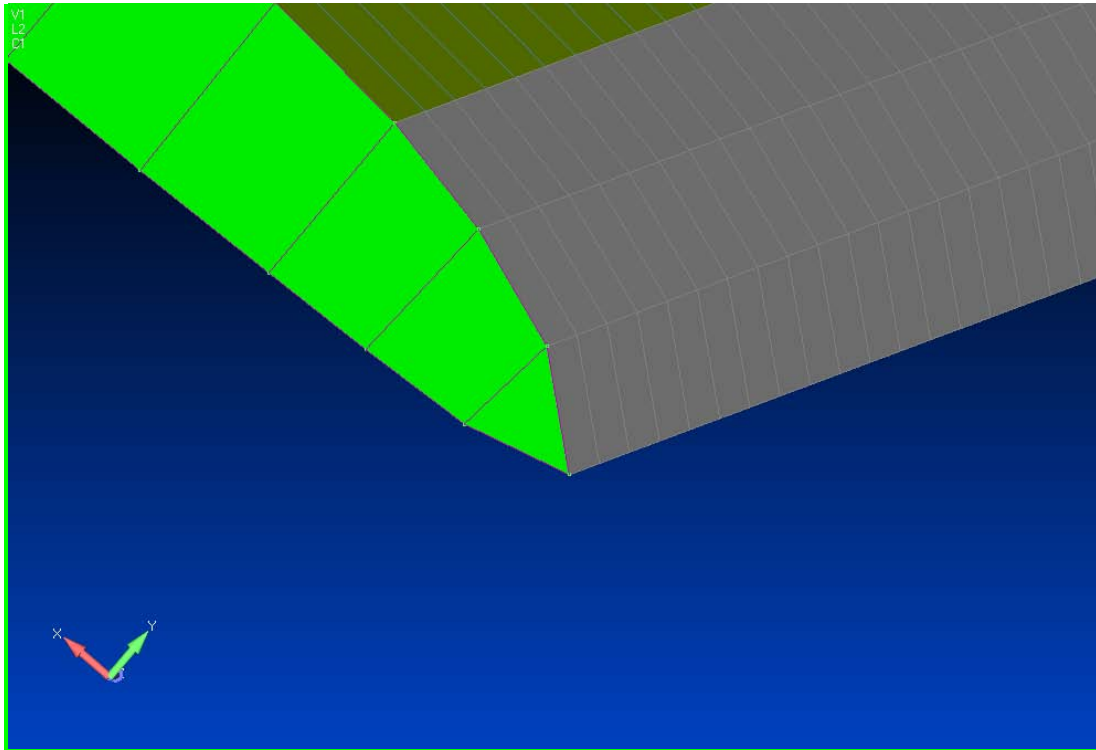


Figure 47. Corrected leading edge foam element

Finally, it was important to carefully note to which nodes constraints and loads were applied. It was often easy to apply loads to nodes rather than geometry depending on how the mesh was developed. A significant challenge occurred when a load was applied where multiple pieces of geometry were co-located. Figure 48 depicts the resulting nonsymmetrical deformation when the load was applied only to the nodes on the right-hand wing box. In order to more accurately apply the load, it was easiest to make a group for the joiner and its elements. With the elements of the joiner active, it was very simple to select only the nodes of the joiner and apply the load to those nodes rather than the wing box.

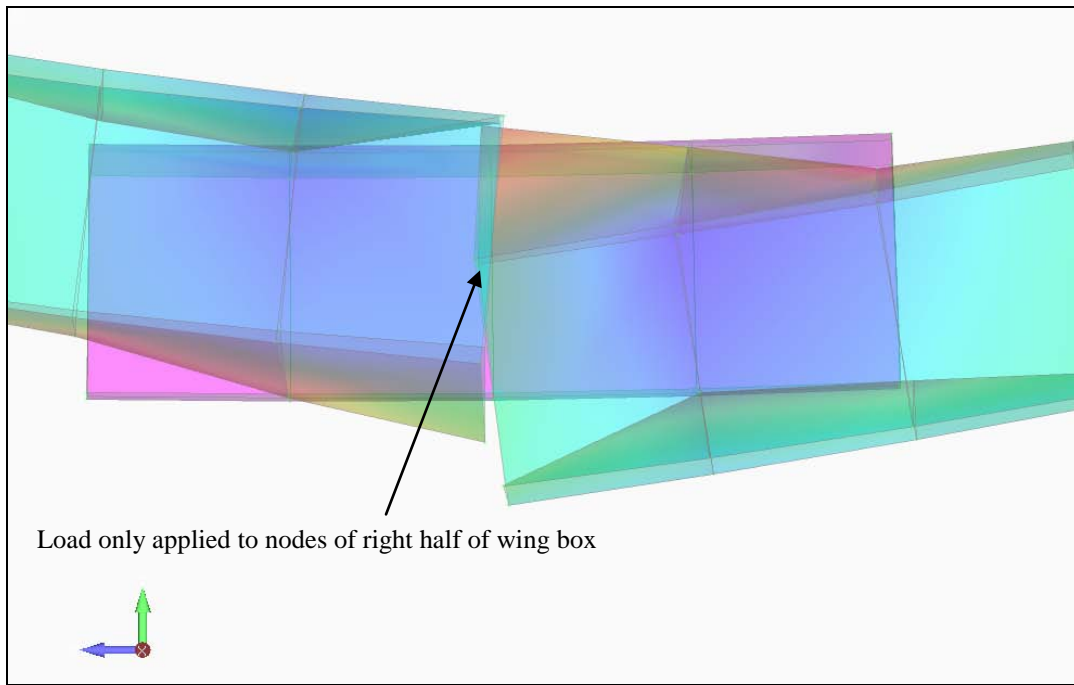


Figure 48. Deformed model with load applied to nodes on the right wing box section

Bending and Torsion Test Rig

To model the bending tests of the wing sections conducted in the University of Michigan's test rig, finite element work again started with the original CAD geometry of the X-HALE wing structure. An orthogonal coordinate system was again defined about the model such that the positive X direction was along the wing chord out the trailing edge of the wing, the positive Y direction was in the direction of the applied load of the test rig, and the positive Z direction was along the span of the wing out the left end of the wing section (from the aircraft's perspective). A depiction of this coordinate system with the CAD representation of a full single wing can be seen in Figure 49.

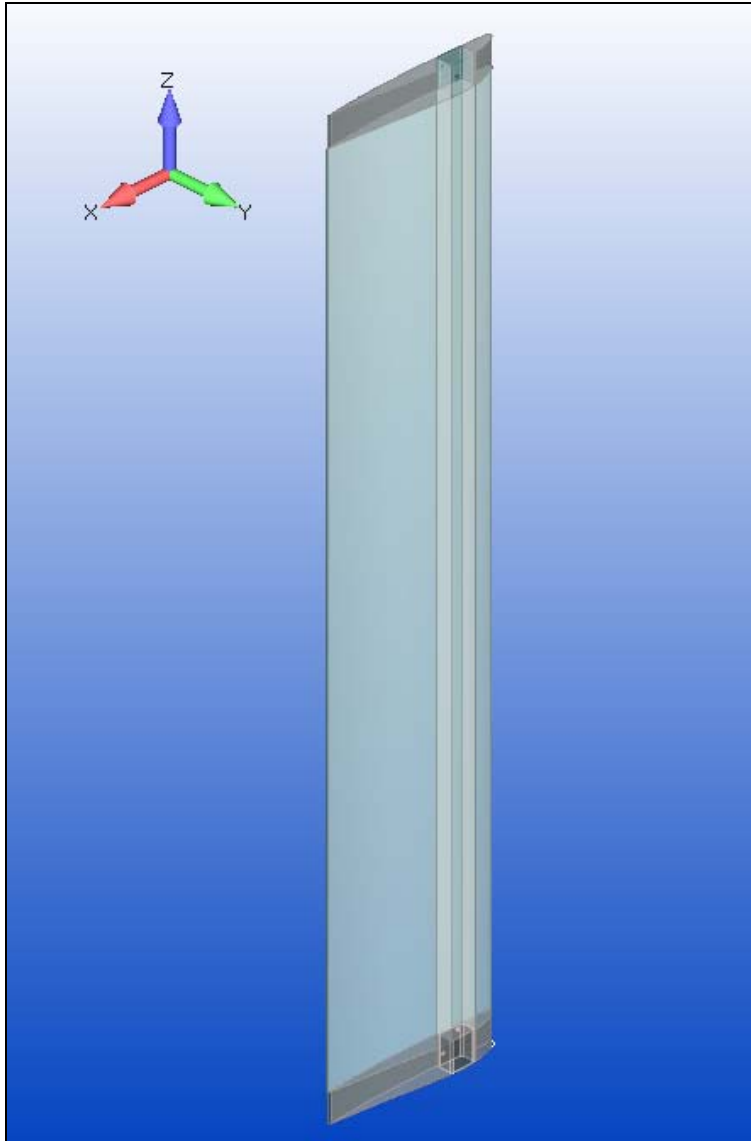


Figure 49. CAD drawing of single wing showing coordinate system

Simplifying Assumptions.

Again, motor fairings were not included in these tests and were therefore neglected from the FE model. Joiner sleeve geometry was also not included in any of the models. In the case of the single wing bending tests, no joiner sleeves were attached to the wing and could therefore be ignored. In the case where bending was performed on a

joined section of two wings, the purpose of the sleeve was to transfer torsional loads between wing sections through the joint, which again gave cause to neglect it from the bending model. Similar to the process used to model the three-point bending test, all carbon IM7 and foam material was neglected to simplify the model. The solid foam would again be added into the FE model once sufficient refinement of the fiberglass portion had been achieved. The starting point of the model looked like the single wing in the Figure 50 – a hollow airfoil consisting of a single layer of fiberglass wrapped around a hollow wing box consisting of five layers of fiberglass.

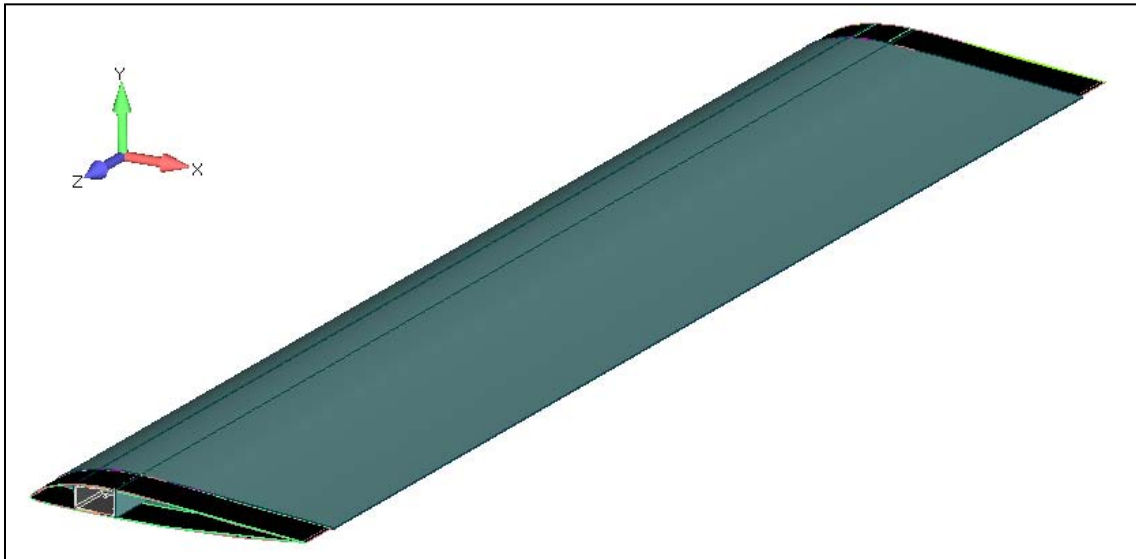


Figure 50. Single wing span representing only fiberglass structure

Loads and Boundary Conditions.

The real world loading and boundary conditions for the bending tests were again straight-forward. One end of the wing section was fixed to the bottom of the rig while a system of pulleys applied loads to the opposite end of the wing. Several early attempts to

apply these loads and constraints were changed prior to the final variants of the model. The most complicated part of applying the loads and constraints related to the size of the wing clamps used to hold the test article in the test rig. As detailed in the previous chapter, the sizes of the two sets of wing clamps used in the test rig differed slightly, resulting in different spanwise areas of wing being covered at each end. The approaches used to address these differences are detailed below.

FE Model Development.

Similar to the process used in the earlier FE modeling effort described previously, this work began by first modeling only the wing box. When some confidence was gained with the wing box model, the airfoil portion of the wing was then modeled by itself. Finally, the elements of the wing box and wing were combined, with varying success.

To begin the wing box model, an extremely simplified version of the wing box geometry was created. The true geometry of the wing box can be seen in Figure 51. Even after the foam and carbon portions of the wing box had been removed, some overly complicated geometry remained. The bolt holes were ignored, and the taper at both ends was removed. Although the design of the wing box is close to square, the top and bottom surfaces of the box actually match the curvature of the airfoil. These walls were removed and replaced with flat surfaces that connected the front and back (or leading edge and trailing edge) walls of the wing box.

The simplified wing box model was then meshed with plate elements. A very coarse mesh of only 12 elements per span was used initially (Figure 52) followed by a much finer mesh (Figure 53). These models were primarily used to investigate methods

of applying loads and constraints, and to confirm that static analysis would run correctly. For both of these models, the test load was initially applied to the nodes on the bottom surface at the top (i.e., free) end of the wing box. The green arrows in these figures indicate the applied loads. For the coarsely meshed model, only the nodes of the element at the end of the wing box were used for loads, while many elements at the end of the finely meshed model were used for selecting elemental nodes for load locations. These were both early attempts to simulate the coverage of the applied bending load based on the size of the wing clamp. A single element of the coarse mesh was longer (spanwise) than the actual wing clamp, and so only the nodes of one elements were used. In the finely meshed model an area of elements more closely matching the spanwise length of the wing clamp (1.457 in.) were used for nodal loading. Similarly, fixed constraints were applied to all of the nodes of the elements corresponding to the area of the bottom wing clamp (these are indicated as light blue triangles in Figure 52 and Figure 53).

Regardless of the coarseness of the mesh used, the applied forces and constraints needed to be more accurately modeled to mimic the wing mounts used in the bending rig. To help with this, the dimensions of the rig mounts were marked on the model inward from each end. Specifically, curves in the X-Y plane were placed on the wing box at the distance along the wing span in from each end that corresponded to the end of each wing clamp. The original four surfaces of the wing box were then separated at these curves, creating twelve separate surfaces. Eight surfaces (four at each end) then corresponded to the wing area held within the wing mounts, with the remaining four surfaces being the main part of the span not held by mounts. This allowed for applying loads and constraints to surfaces rather than nodes, as well as defining different mesh sizes for the

separate sections along the wing span. Creating groups within FEMAP assisted in viewing and selecting the appropriate surfaces. In Figure 54, the differing mesh sizes of the two ends and middle portion of the wing box can be seen in the deformed mesh of the wing box model by the varying spacing of the white border lines of the elements.

With the model divided into separate surfaces, the load was then applied to the “back” surface (which corresponded to the bottom airfoil side of the wing box) of the “top” wing mount group (the free end of the wing box), while the fixed constraint was applied to the surfaces of the “bottom” wing mount group. Figure 55 shows the outline of the free end of the wing box with loads defined on the back surface of the wing mount and the deformed mesh (with color contours) resulting from an applied load of 0.674 lb (3 N). Although a relatively coarse mesh of 132 elements (with an element size of 1.17326) was used for this model, experimenting with meshes of double the number of elements and greater indicated little, if any, change in deflection data. Thus, the coarse 132-element mesh model of the wing box was considered sufficient at this point in the development process.

Turning from geometry and mesh sizing, the physical properties of the wing box model were evaluated next. The plate thickness of the elements comprising the wing box model was adjusted to equal that of five plies of fiberglass, further refining the model and yielding noticeable changes in the total translations of its elements. This simplified model of the wing box produced deflection results which matched the lab results close enough to move forward with analyses. A multi-set analysis was performed on this model for all five load cases conducted in the laboratory tests.

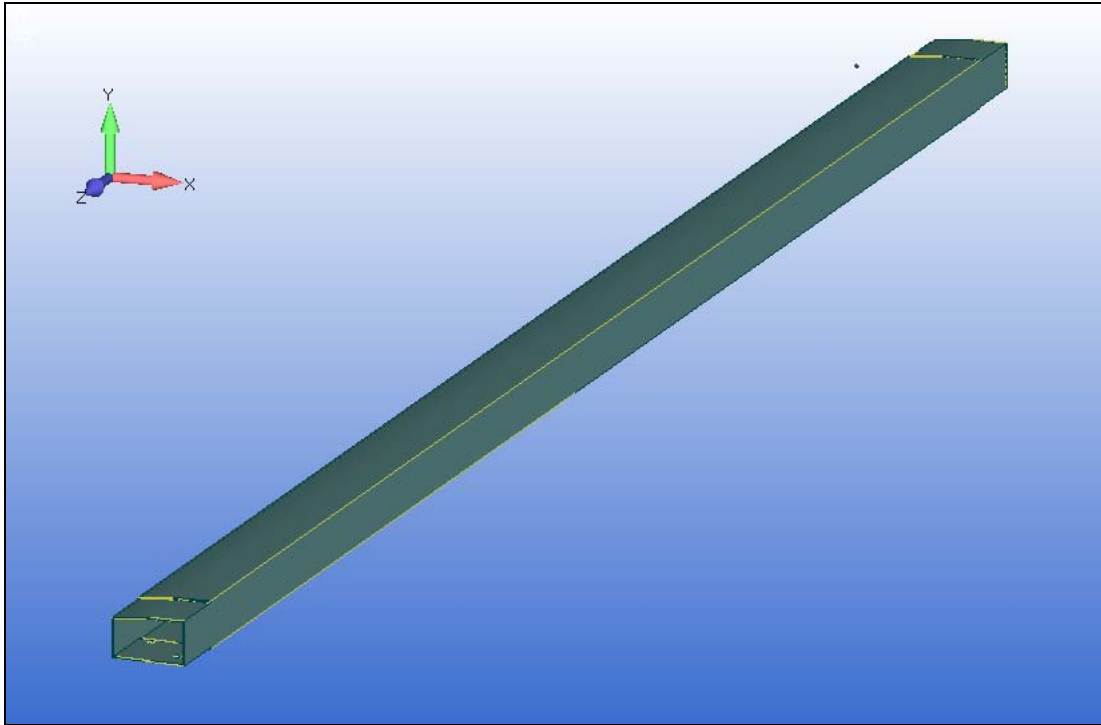


Figure 51. Original CAD geometry of single wing box

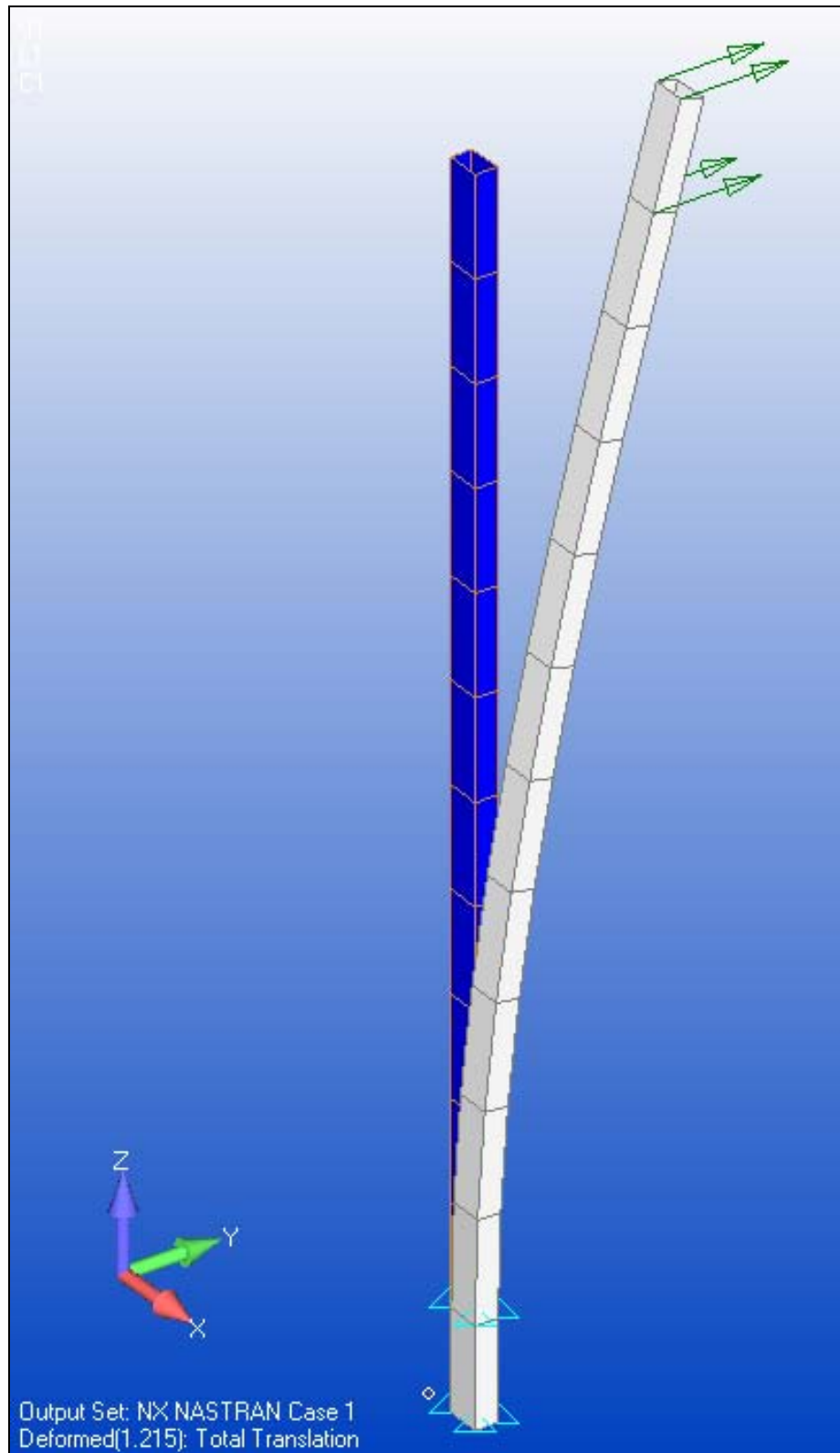


Figure 52. Undeformed (blue) and deformed (white) coarse mesh of wing box

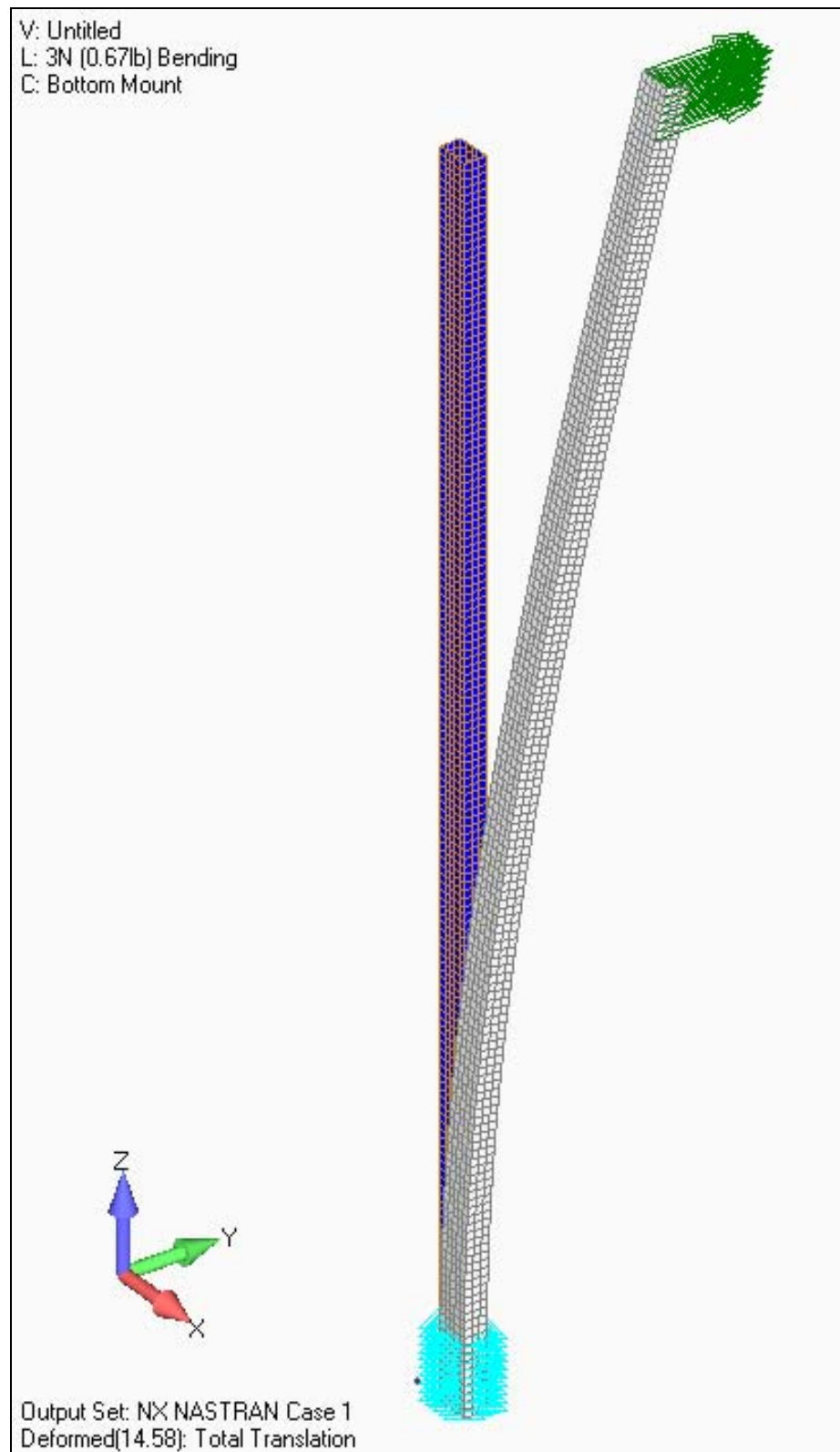


Figure 53. Undeformed (blue) and deformed (white) fine mesh of wing box

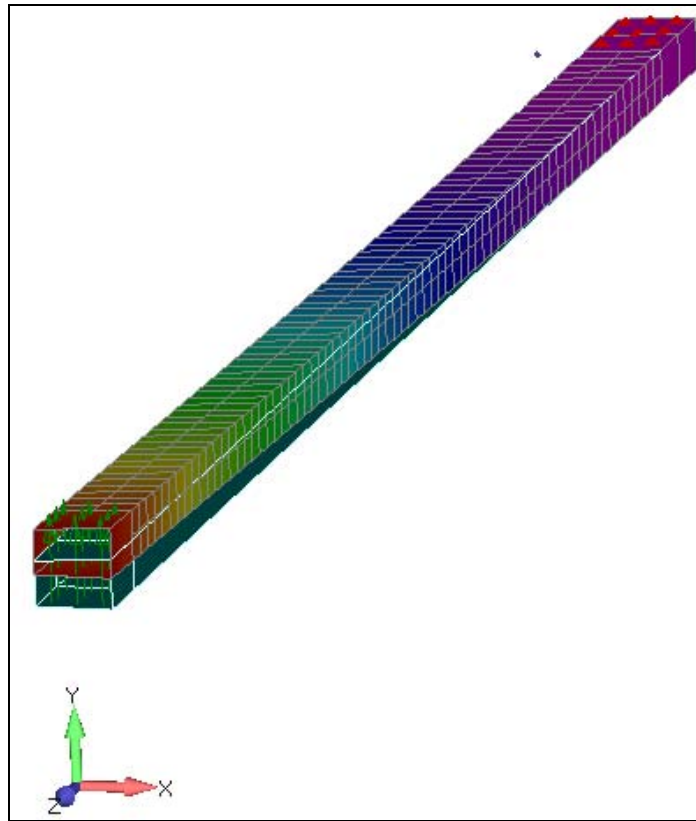


Figure 54. Wing box mesh showing 3 different mesh sizes along span

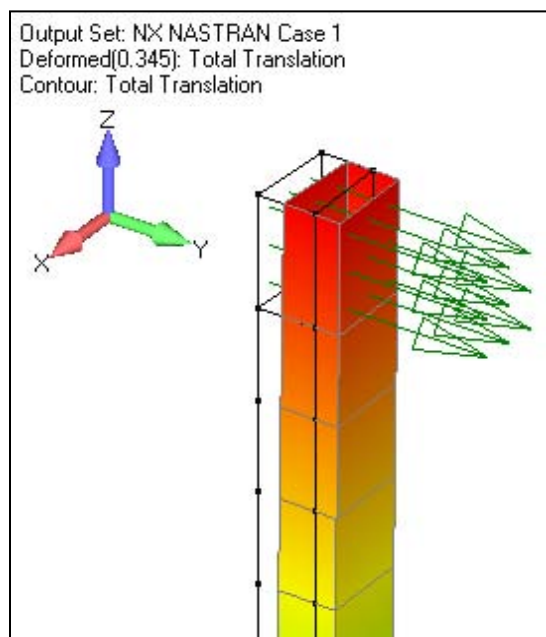


Figure 55. View showing placement of load at free end of wing box with deformed mesh

The process used to model the airfoil portion of a single wing was similar to that of the wing box described above. Starting with the same geometry (Figure 50), all foam and tapered ends were removed. The wing box was also removed, leaving only the outermost curves and surfaces of the wing skin. A surface was added along the trailing edge of the wing to connect the top and bottom surfaces of the wing, capping what was otherwise a gap where those surfaces ended. Finally, these basic surfaces of the airfoil were divided such that separate surfaces corresponded to the wing mounts at both ends.

Loads were again applied to the bottom surface of the wing within the top wing mount and constraints were applied to all surfaces within the bottom wing mount, as can be seen in Figure 56. The mesh for this airfoil-only model used a element sizing of 0.5, resulting in 2640 elements. As compared to the true geometry shape of the airfoil this mesh was still relatively coarse, but was fine enough for this purpose.

After initial analysis was performed on this model, unexpected deflection results were noticed. Loads applied to this version of the wing model caused the bottom wing surface to displace in the +Y direction through the top surface. This was difficult to detect without activating the contour plot function of FEMAP. Once activated, the elements experiencing the maximum translation of the model were clearly evident as those along the bottom wing surface colored red in Figure 57.

These displacement results were caused by the lack any elements connecting the top and bottom surfaces together, which makes sense rationally after visually inspecting the deformation of the model. With the two surfaces only connected at the leading and trailing edges, the edge of the bottom surface deflected the farthest when the loads were applied to only that surface.

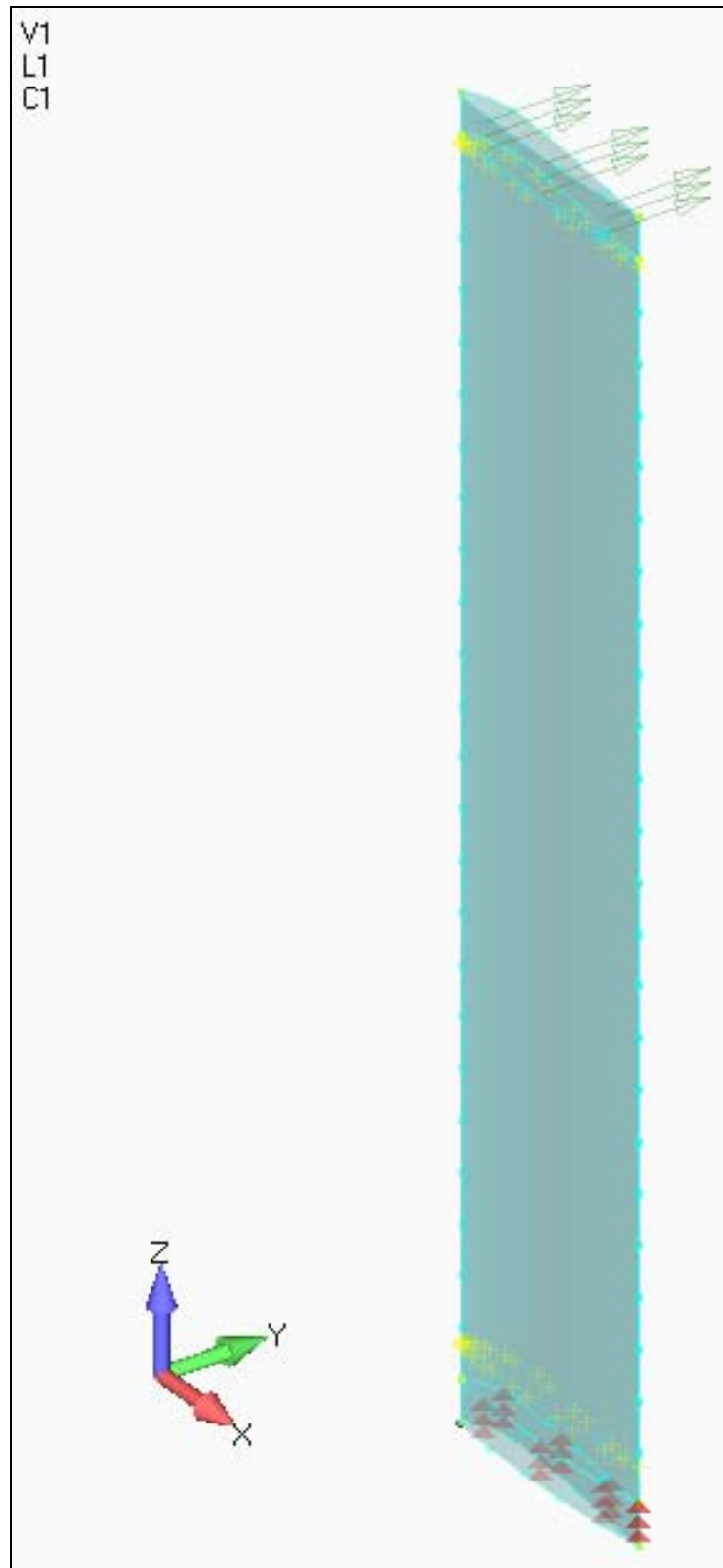


Figure 56. Airfoil-only model of single wing showing applied load and constraint

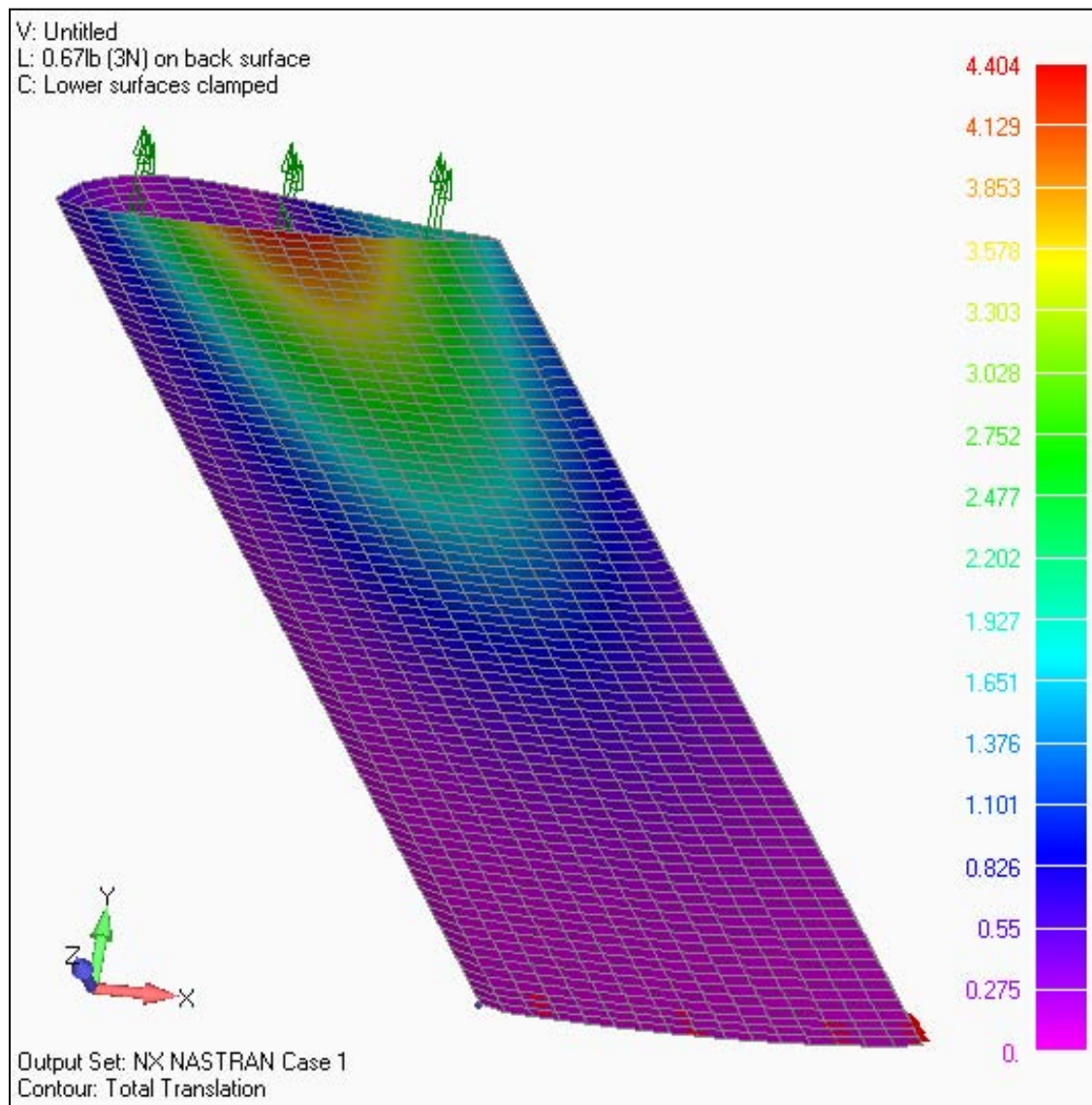


Figure 57. Single wing model with color contours showing total element translation

Further investigation quickly confirmed that connections between the upper and lower wing surfaces would prevent the behavior seen above and be required to increase the realism of the model. The nodes along the free edge of two meshes of the wing model, one coarse and one finer mesh, were connected with rigid elements. While the coarse mesh was ultimately discarded for reasons discussed later, it was useful to quickly explore techniques for applying rigid connections between sets of nodes. Depictions of these two meshes with rigid elements added along the free edge can be seen in Figure 58. Post analysis, setting the color contours to Total Translation revealed both upper and lower surfaces were deflected by the applied loads. Elements within the red and orange contour are those which experienced maximum displacement. The added rigid elements are represented as white lines drawn between nodes of the two surfaces along the wing's edge.

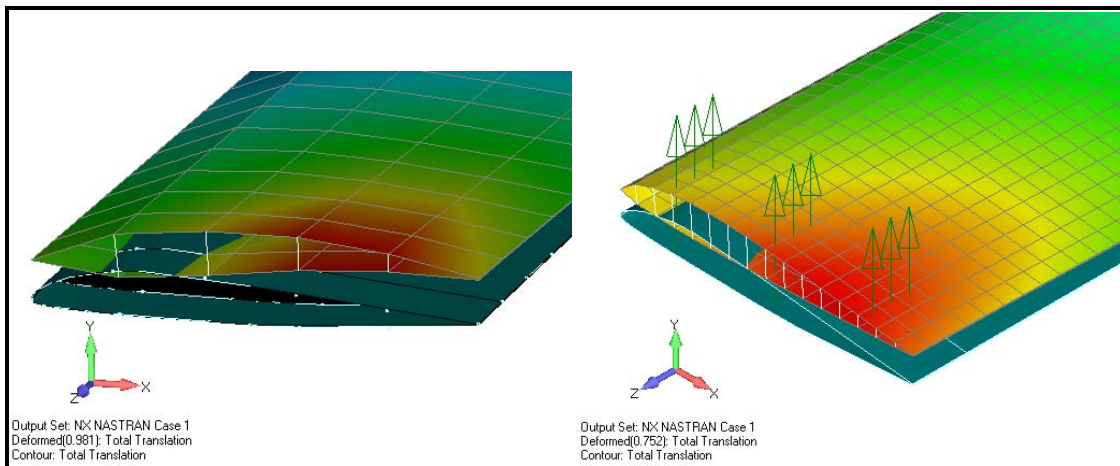


Figure 58. Two single wing meshes with rigid elements (white lines) along free edge

A multi-set analysis of all five loads sets which had been performed in the laboratory was conducted on the single airfoil model. At this point, the wing box and airfoil models had been analyzed for the range of loads subjected during static testing in the laboratory. The results for each loading condition on the two individual models were compared with those of the laboratory test and will be discussed in the next chapter.

The next step in the evolution of the model was to combine the wing box and airfoil structures into the same model. This began by merging the simplified geometries of both parts, as previously described, into one model (illustrated in Figure 59). The models of both the wing box and airfoil with wing mount areas defined on their ends were used for this combined geometry.

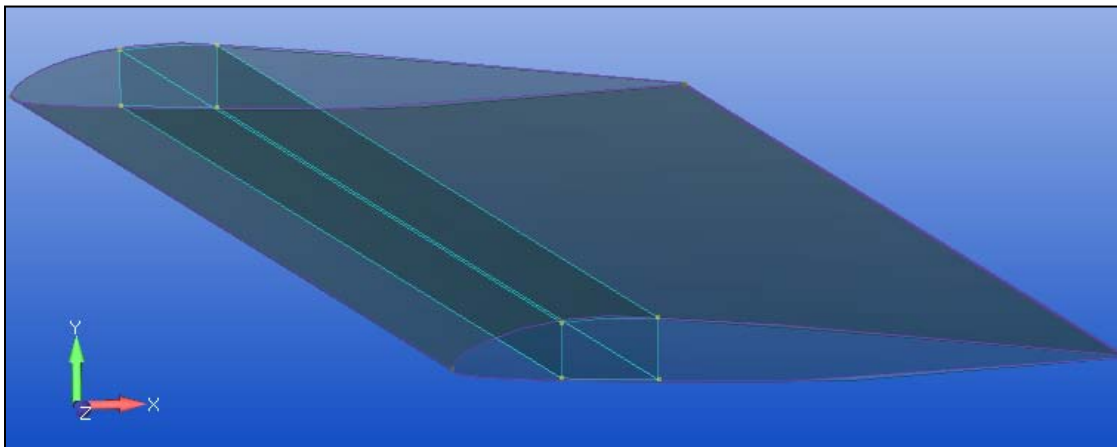


Figure 59. Transparent view showing wing box and airfoil geometries merged

Once merged, the top and bottom surfaces of the wing box (those surfaces which were roughly parallel with the airfoil surfaces) were removed. The remaining vertical surfaces of the wing box were extended to intersect both top and bottom wing surfaces.

This resulted in a model of the wing with the leading edge and trailing edge surfaces of the wing box inside and “connected” to the wing surfaces, both with areas for the wing mounts marked off. Using the "Mesh Control Along Curve" command on both the airfoil and wing box span edges, the model was set with ten spanwise elements for the main portion of the wing (inward of both mounts), one spanwise element for the top wing mount, and two spanwise elements for the bottom wing mount. This mesh control was beneficial because the rows of elements along the span lined up between the airfoil and wing box. However, FEMAP’s automatic mesh sizing of only five elements per chord along the airfoil portion of the wing resulted in wing box nodes too far away from the corresponding nodes of the upper and lower wing surfaces. The resulting mesh of this geometry can be seen in Figure 60, with green dots indicating the positions of nodes.

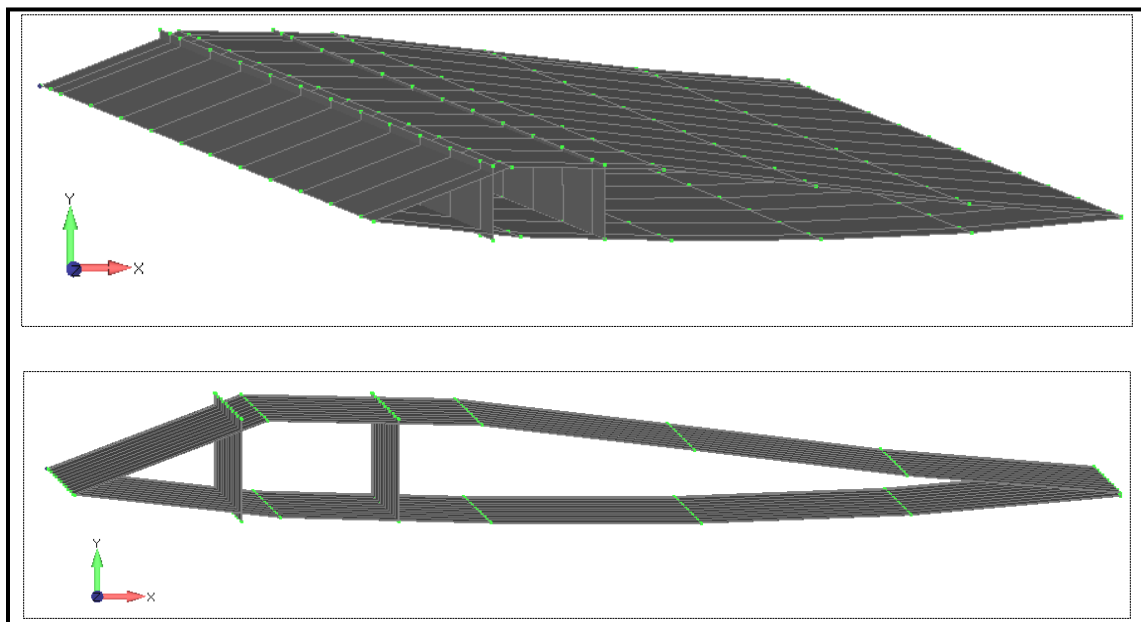


Figure 60. Initial mesh of combined wing box and airfoil model (top); and view showing poor chordwise alignment of airfoil and wing box elements (bottom)

The alignment between wing box and airfoil nodes improved greatly by adjusting the chordwise mesh control to 50 elements. This mesh resulted in a maximum distance of 0.06 in. between any wing box node and wing surface node along the cross section. While this was sufficiently close along the wing box portion of the wing chord, it was noted that nodes at the trailing edge of the wing surfaces were less than 0.06 in. apart. If all nodes within 0.06 in. of each other were merged together this would have changed the mesh at the trailing edge to a sharp edge, which was deemed undesirable at this stage. Instead, only those nodes near the wing box area of the model were selected and merged – 56 nodes in total.

With an approximate wing box now successfully added to the airfoil-only model, an initial 3N test load was applied to the wing mount surface at the free end of the wing and the model was analyzed. As anticipated, the resulting deflection was concentrated along the trailing edge half of the wing (see Figure 61). This behavior seemed appropriate for a model consisting of only wing skin and wing box elements. Without rigid links between the upper and lower wing surfaces, the lower surface of the wing (where the load was applied) again deflected through the upper wing surface (see Figure 62). Adding rigid links between the wing surfaces forward and aft of the wing box, as shown in Figure 63, once again prevented this unrealistic deformation.

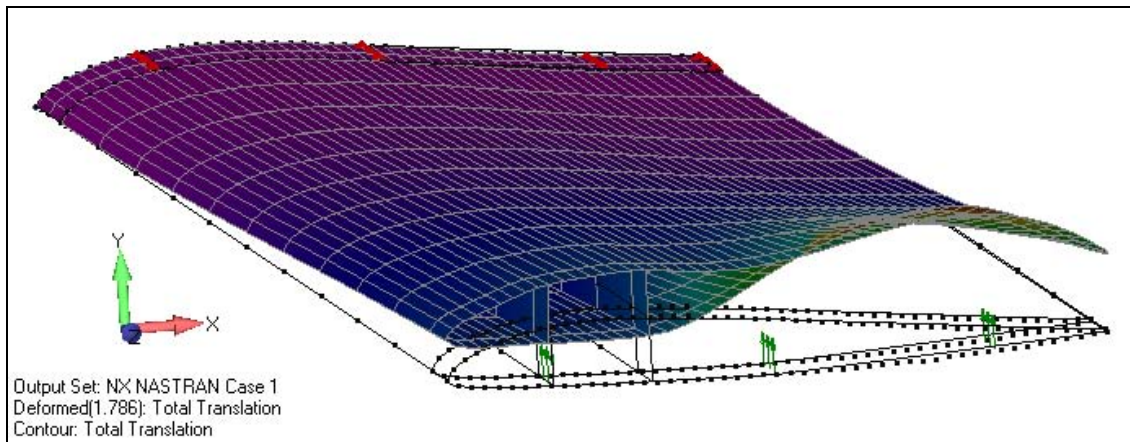


Figure 61. Outline of undeformed wing and deformed color contour mesh showing concentration of translated elements along trailing edge half of free edge

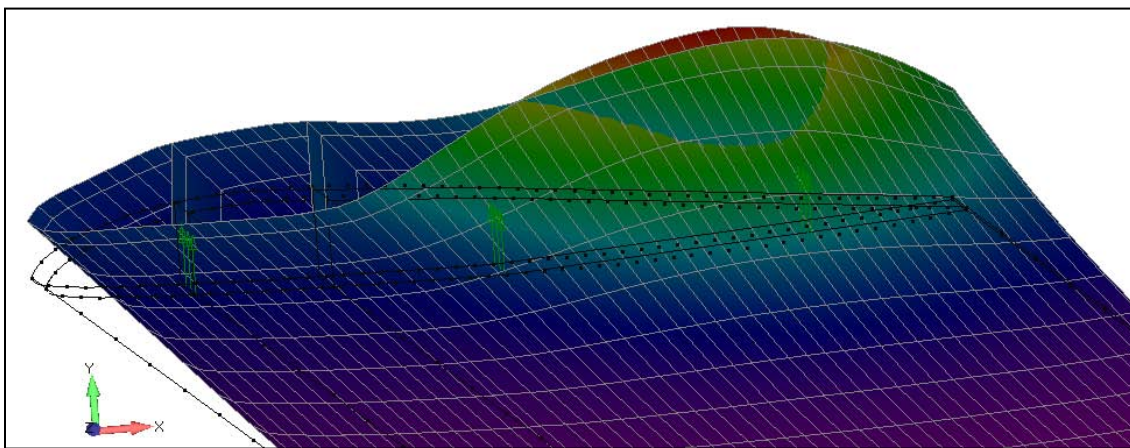


Figure 62. Outline of undeformed wing and deformed mesh showing elements of lower wing surface deflecting through those of upper wing surface

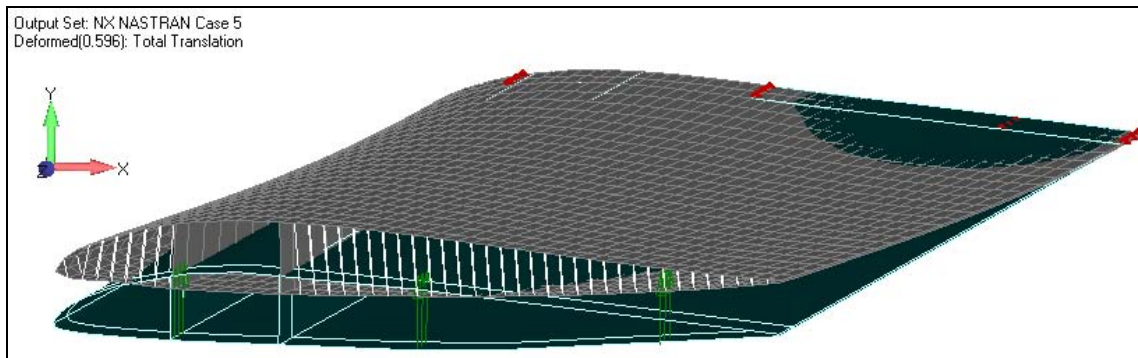


Figure 63. Undeformed wing (dark green) and deformed mesh (gray) with rigid links added between wing surfaces along free edge (white lines)

Focus was turned to the material properties of the model. The current Wing Box properties had not been changed to account for the five layers of fiberglass used in the manufacturing of the wing box. Material properties were examined and adjusted to improve the fidelity of the combined airfoil and wing box model. Two new properties were defined – one with a thickness five times that of a single layer of fiberglass and a second with a thickness six times that of a single layer of fiberglass. Using the Modify... Update Elements... Property ID command, the elements along the leading edge and trailing edge walls of the Wing Box were selected and their Property changed to the one with a thickness five times greater than the original PLATE elements. Additionally, the elements on the top and bottom wing surfaces in between the leading edge and trailing edge Wing Box walls were selected and their Property changed to the one equaling a thickness of six fiberglass layers. These six layers corresponded to the five layers used in constructing the wing box plus the additional layer of the airfoil. Using this Airfoil and Wing Box model, a multi-set analysis for all five load cases for the Single Wing Bending was performed and will be discussed further in Chapter IV.

This iteration of the model was still a relatively simple approximation. It did not accurately model the true manufacturing of the wing structure, where a fully constructed wing box made of five layers of fiberglass and filled with foam was then wrapped inside the single-layer airfoil with foam forward and aft of the wing box. The method described here almost certainly created a more perfect connection than actually resulted during construction of the wing. However, any errors produced by this difference were assumed to be small and therefore neglected.

The next step to improve the wing model was to add solid foam elements inside the hollow structure of the wing, including both the wing box and areas inside the airfoil forward and aft of the wing box. This process was started by going back to the simple model of only the wing box. Solid geometry was added to fill the inside of the wing box cross section. The areas at each end of the wing box within the wing mount sections were left hollow, as was done 1.25 in. inward from each end in the physical construction of each wing box section to allow room for the wing joiner to fit. This variant of the model can be seen in Figure 64. The mesh control was kept the same as the previously meshed walls of the wing box, producing solid elements with the same spacing as the plate elements of the wing box. The solid foam portion of the model was meshed using HexMesh Solids. All corresponding nodes along the meshed solid foam were coincident with those of the wing box wall and were subsequently merged. Finally, once individual test analyses had been conducted to check its overall behavior, a multi-load analysis was performed on this most complete version of the foam-filled wing box model. Figure 65 depicts a view of one of the results from this analysis.

Modeling work continued by adding solid foam elements to the FE model of the wing which included both the wing box and airfoil. The rigid elements previously added along the free edge of the wing, which had been a temporary fix to keep the airfoil shape of that model, were first removed. Solid foam elements were then added to each of the three sections of the wing chord – the portion between the leading edge of the wing and the forward wall of the wing box, the area inside the wing box, and the remaining area between the aft wall of the wing box and the trailing edge of the airfoil. Figure 66 shows the mesh with a full span of solid elements added to the leading edge portion, solid elements added inside the wing box area with the exception of the outer edge row, and almost all of the solid foam added within the trailing edge section of the airfoil before the final row of elements were added along the outer edge.

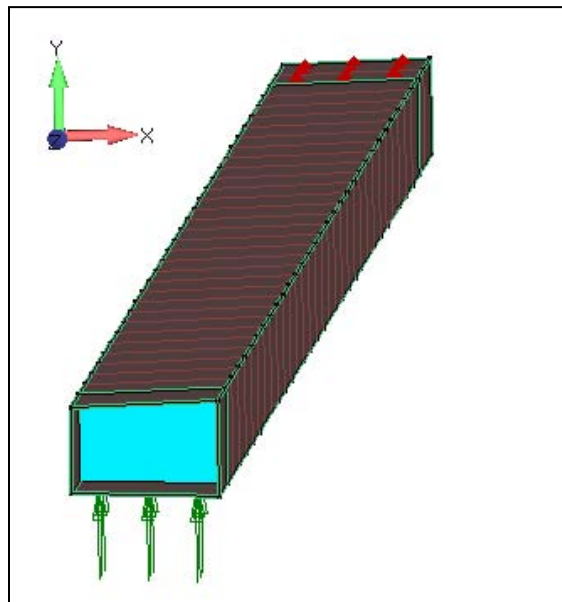


Figure 64. Wing box model with solid foam (bright blue) inside fiberglass walls

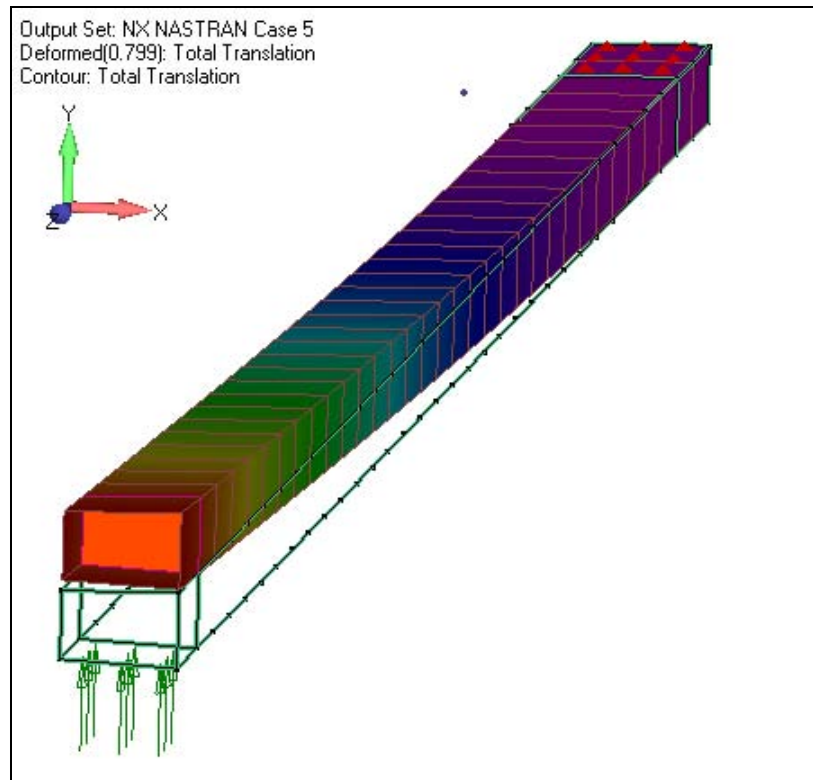


Figure 65. Undeformed outline and deformed color contour mesh of wing box with solid foam (bright orange)

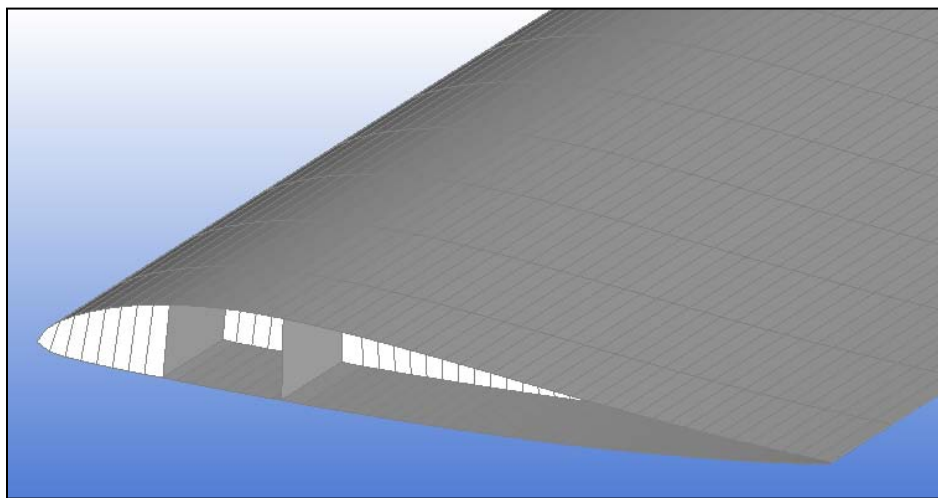


Figure 66. Wing mesh in the progress of adding solid foam elements (white) within fiberglass plate elements (gray)

The technique used to incorporate the solid elements into the model involved breaking the process down into steps, each step relating to the portions mentioned above. To begin each step, a chordwise row of solid elements were added by hand at the end of the wing section. Using block elements, the four nodes of the plate element on the top surface of the wing and the four nodes of the bottom surface of the wing were selected to define each solid element. Once a chordwise row of solid elements were added to each of the three sections of the wing, those elements were copied throughout the remaining span of the wing. A visual inspection of the wing model from a "top down" perspective confirmed that solid elements and the plate elements of the airfoil and wing box were all equally spaced along the span of the wing. Checking for coincident nodes also confirmed this requirement, and was necessary to "attach" the newly added foam to the previously created fiberglass portion of the model. For the wing box area, the section of the model corresponding to the wing mounts used in the bending test were again left hollow, roughly corresponding to the portion of the actual wing section where the joiner fits into each end of a wing to join the wings together. For the leading and trailing edge portions of the airfoil, solid elements were added all the way to both edges.

With solid foam elements added throughout the single wing section and coincident nodes merged, the multi-set static bending analysis using NX NASTRAN was conducted again. The results appeared realistic and closely matched the deflections from the static laboratory tests, as will be discussed in the following chapter. A view of this full single wing model's mesh, combining fiberglass plate elements and foam solid elements, is shown in Figure 67.

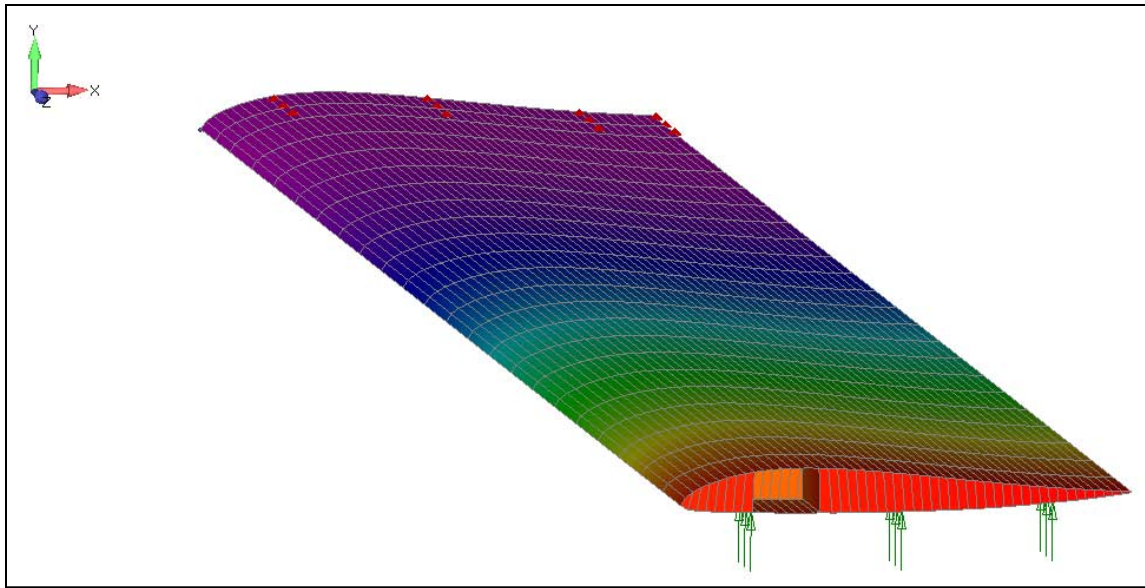


Figure 67. Color contour mesh of foam-filled single wing model

With a fair amount of confidence gained in the fidelity of the wing model, additional checks were performed to further investigate the qualities of the model. First, a modal analysis was conducted, producing results for the first ten modes. Overall, the general behavior of the wing model was acceptable. No unusual or physically impossible deflections were detected, indicating the construction and connection of the model was accurate. However, the depicted modes were at extremely low frequencies – all less than 1 Hz. Modes of such low frequencies would not have been likely for such a structure, and indicated that the mass properties of the model were not correct.

Two final loading conditions were applied to the model to confirm realistic behavior. A constant set of loads along the trailing edge nodes were added to simulate a chordwise load, and similarly a set of loads along one end of the wing were added to

simulate a spanwise load. Although very large loads were applied and will not likely be experienced by the actual aircraft, the deflection behavior of the model further confirmed that the physical representation of the combined finite elements were accurate to an acceptable level. Figure 68 and Figure 69 show the resulting deformation (graphically exaggerated to highlight relative translation) of the above mentioned chordwise and spanwise test loads, respectively, and confirm the desired continuous behavior of the developed FE model.

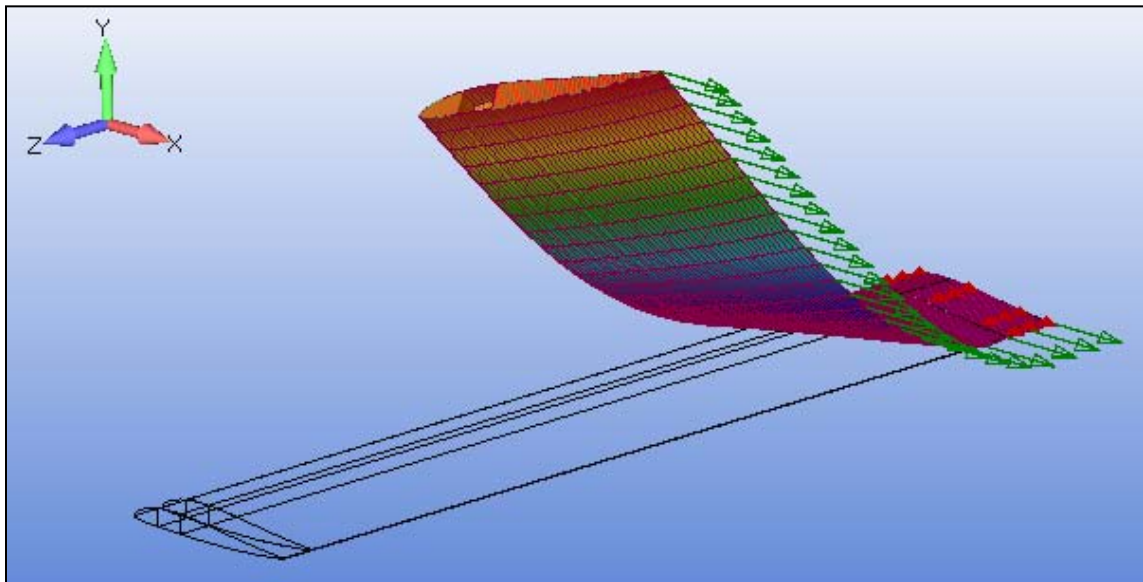


Figure 68. Outline of single wing and deformed mesh resulting from test load applied to trailing edge of wing

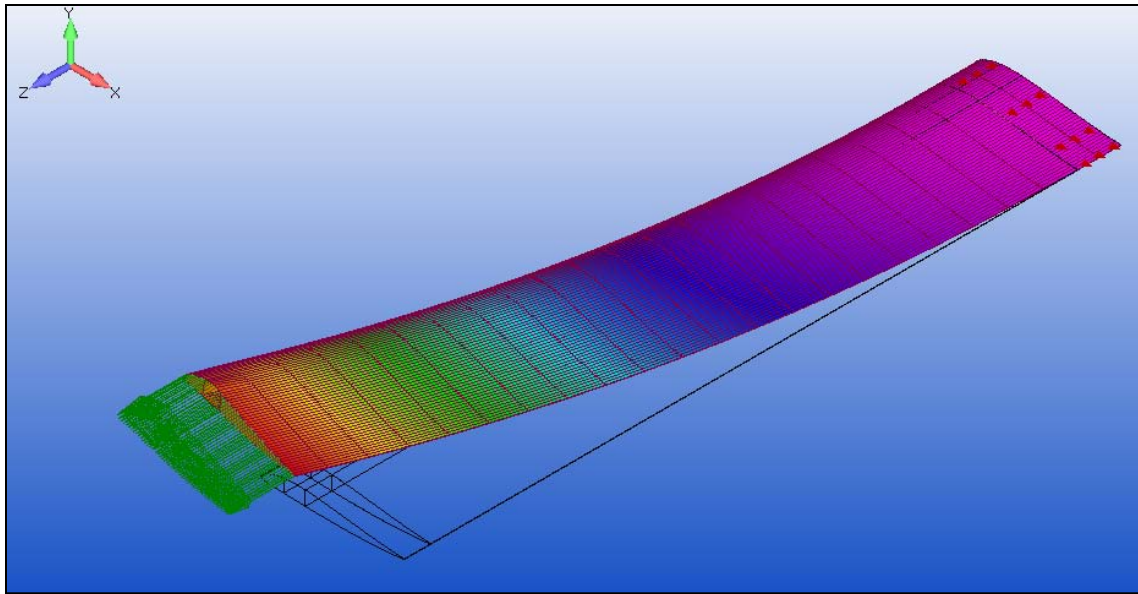


Figure 69. Outline of single wing and deformed mesh resulting from test load applied to free edge of wing

With the creation of a satisfactory single-wing model, the immediate next step was to expand the model to be able to represent those tests that were conducted on the joined two-wing section of the X-HALE structure. The first two structural elements of this expansion were a second wing section and the aluminum joiner used to connect the two wing sections. Before attempting to model the complex aluminum joiner block, a simplified two-wing model was created without any joiner geometry.

The full geometry and FE mesh of the single wing model discussed above was copied and placed 39.37 in. in the Z direction relative to the original mesh. This, in effect, attached the second wing section to what had been the free end of the first wing section. The plane of attachment can be seen in Figure 70 as the line of nodes highlighted yellow. Although this two-wing model was not symmetric about its new center, it kept the end clamp areas of the mesh the same. Loads were then removed from

the original single wing and defined at the new free end of the two-wing model (the highlighted surface of Figure 71 indicates the lower wing surface where loads were applied). In order to associate the surface loads with the mesh, the copied fiberglass plate elements within the "wing clamp" were deleted and recreated. Finally, all coincident nodes were merged, effectively connecting the elements of the double span into one continuous model.

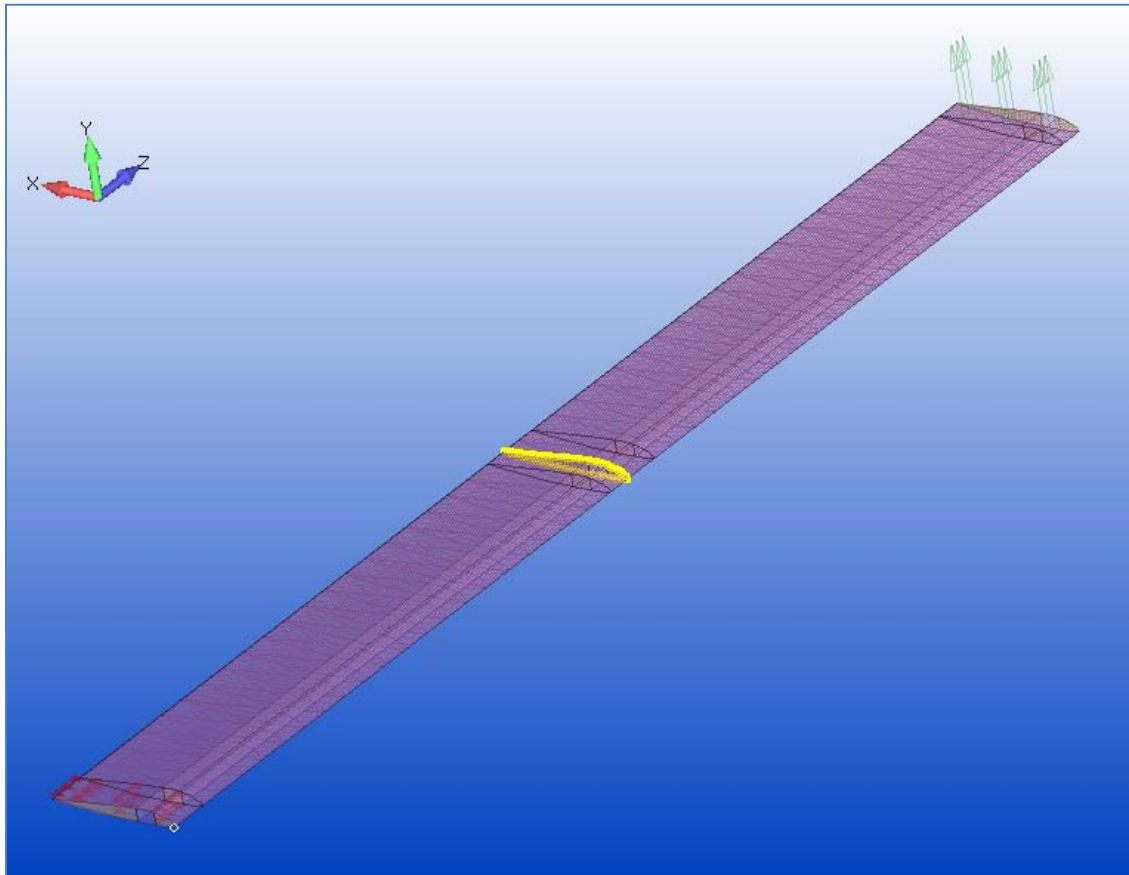


Figure 70. Two-wing model with coincident nodes along joint highlighted

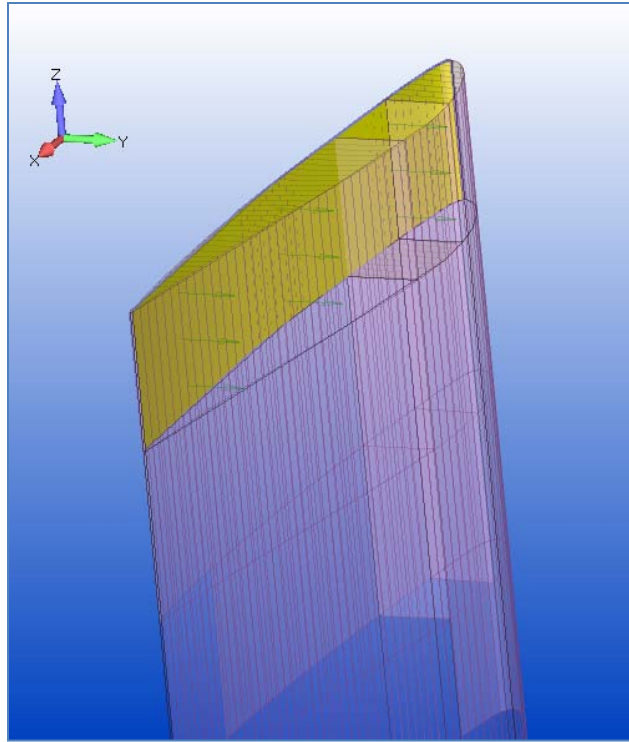


Figure 71. 2-wing model showing surface where loads were applied (highlighted yellow)

After obtaining promising deflection results from the first attempt at a model of the two-wing test section, the joiner block was incorporated. First, the original CAD geometry of the machined aluminum joiner (see Figure 72) was imported into the model of the single wing. An initial check of the mass of the joiner was easily performed using FEMAP's Mass Properties tool. Although this was long before a mesh had been created for the joiner and no materials or properties had yet been defined for the aluminum piece, FEMAP allowed for calculating the mass of solid geometry by the user defining the density of the piece. Using a density of 0.0975 lb/in.^3 for 6061 aluminum, the mass of the joiner was calculated to be 0.04445 lb [5, 14]. To compare, a machined aluminum joiner to be used in the X-HALE aircraft was weighed and found to be 0.04736 lb.

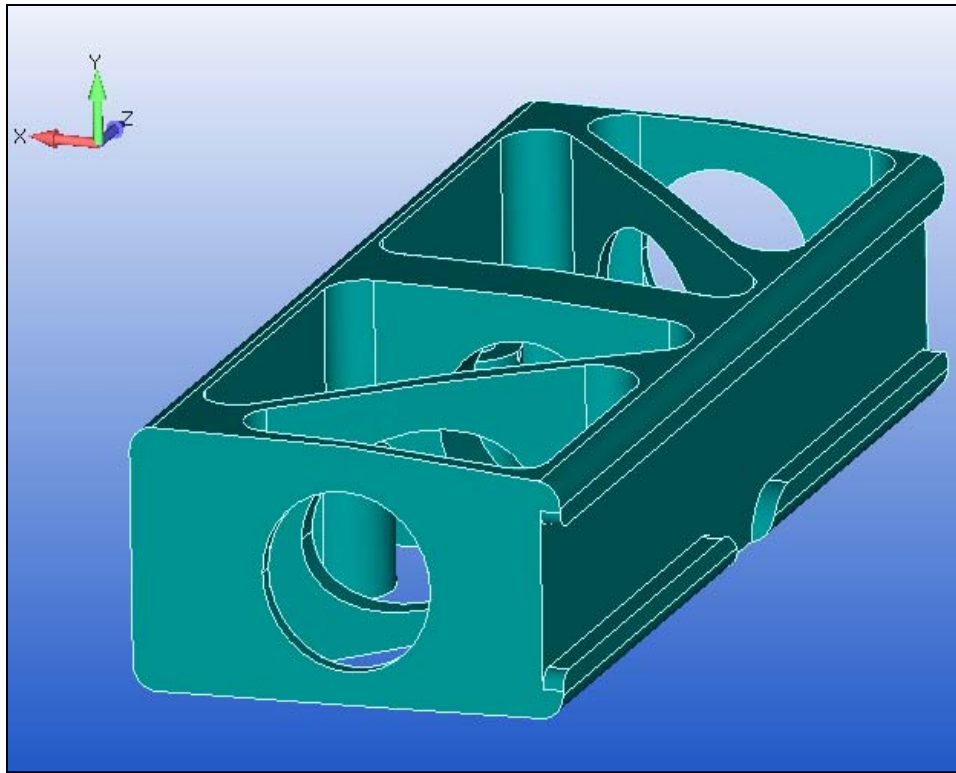


Figure 72. Original CAD geometry of aluminum joiner

Initial importation placed the joiner at the end of the wing that corresponded with the fixed constraint of the bending rig. Even though the actual wing box thickness was not depicted in the FE model, it was apparent that the true geometry of the joiner piece would likely be a poor fit for the opening of the wing box mesh, as can be seen in Figure 73 through Figure 76. Finally, a copy of the imported joiner geometry was projected to the opposite end of the single wing (see Figure 77).

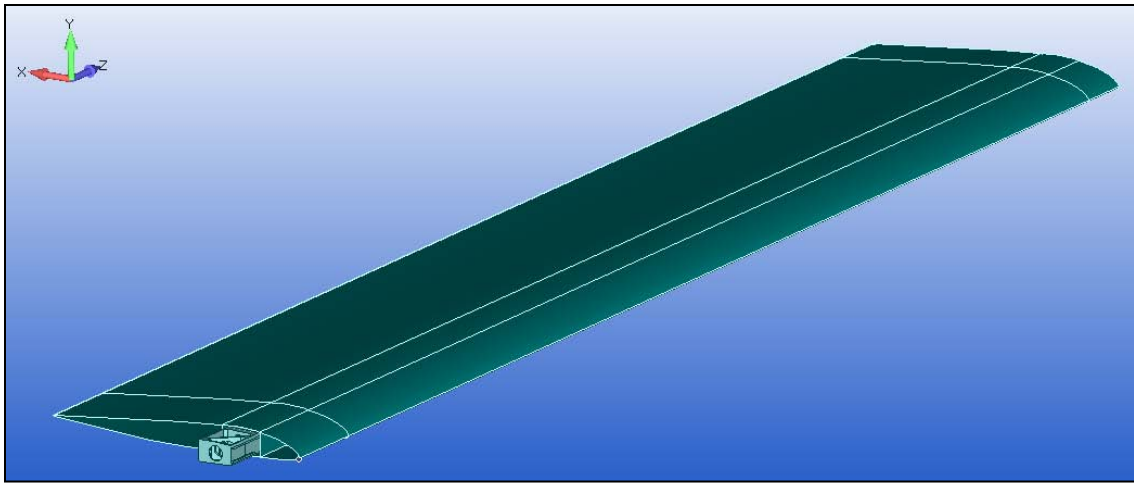


Figure 73. Single wing model with AI joiner imported from original CAD

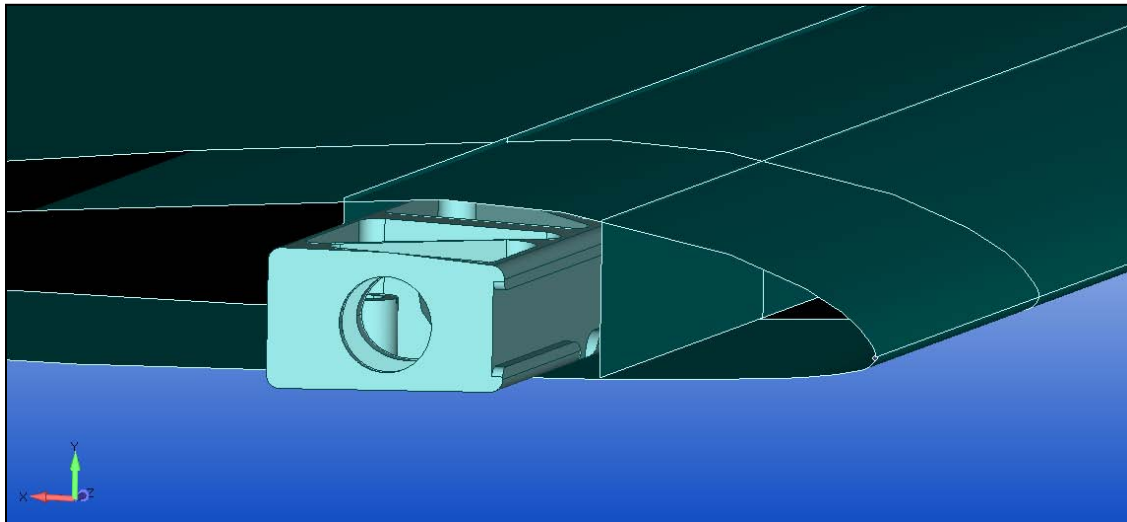


Figure 74. Single wing model with AI joiner imported from original CAD

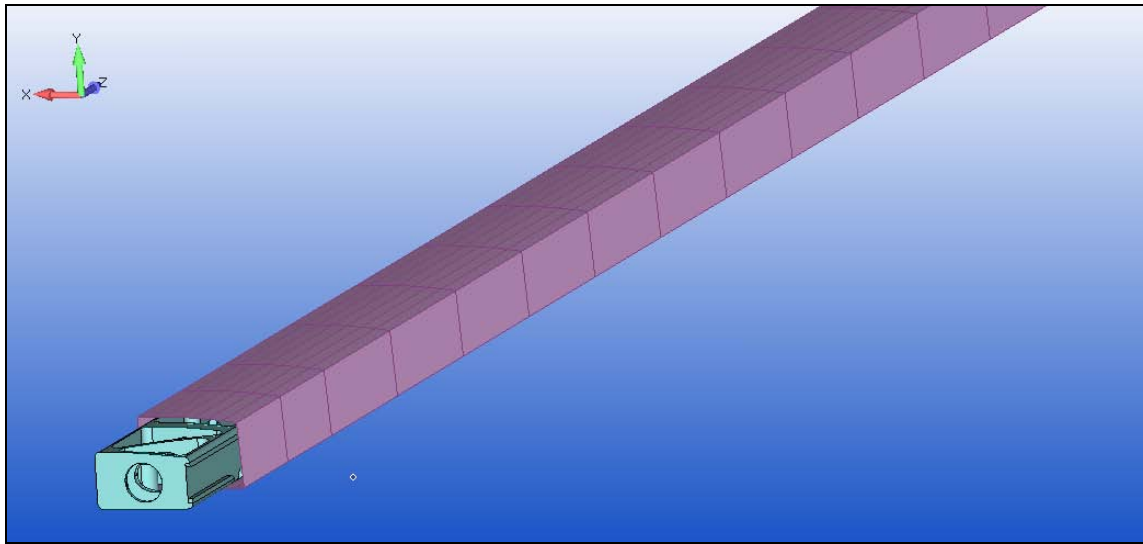


Figure 75. Single wing box mesh with Al joiner imported from original CAD

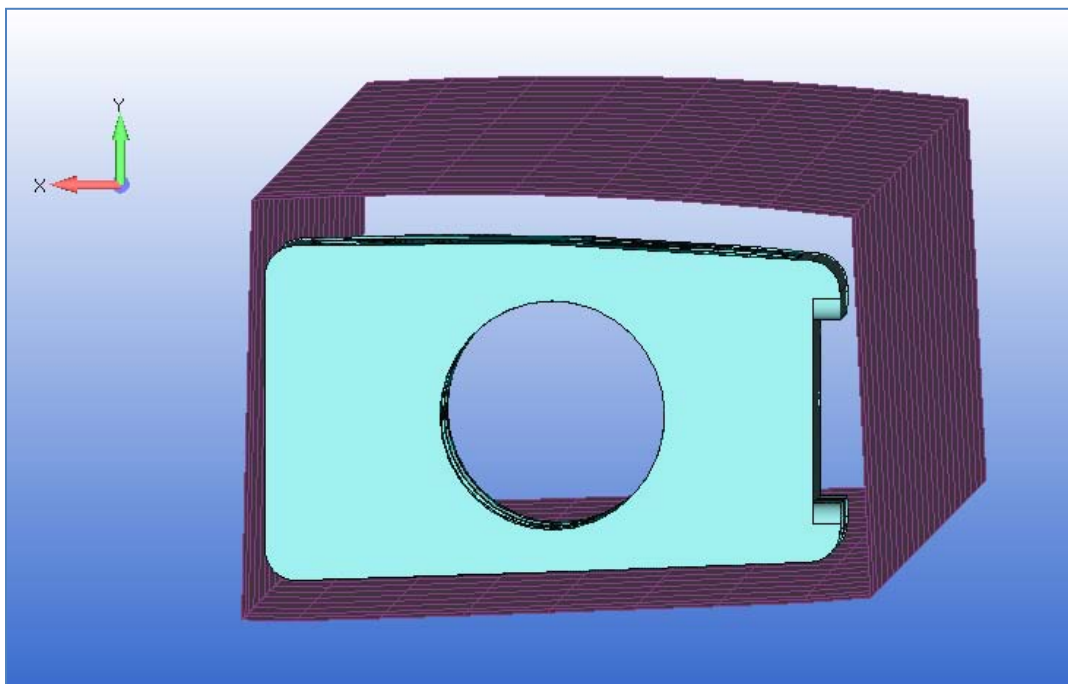


Figure 76. Single wing box mesh with Al joiner imported from original CAD

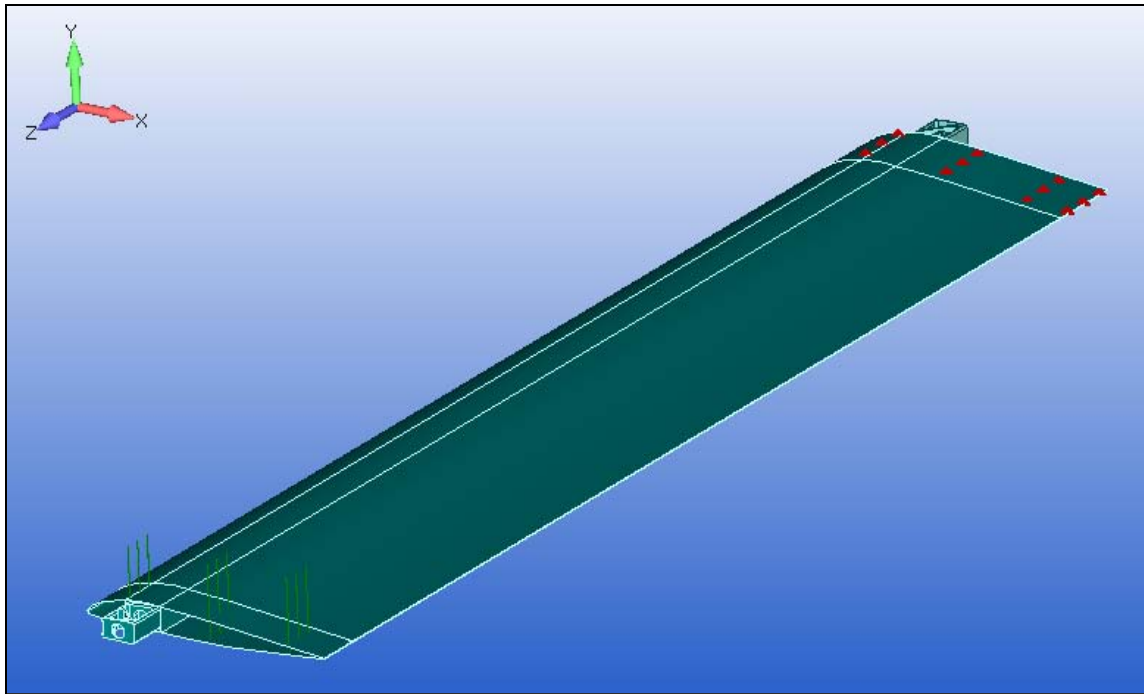


Figure 77. Single wing model with Al joiner copied to free end of wing

The geometry of the joiner was confirmed at the intended location within the model and the first copy was removed. Next, the mesh of the wing was copied about a plane corresponding to the edge of the wing where the force had been applied in the bending tests of the single wing. While the original model was not symmetric about its center, this process of mirroring the mesh about its end produced a mesh with twice the span length which was then symmetric about its new center. This new center of the FE mesh was also the location of the aluminum joiner geometry, as can be seen in the following figures. Finally, elements of the wing model were separated into groups to aid in isolating various portions of the model.

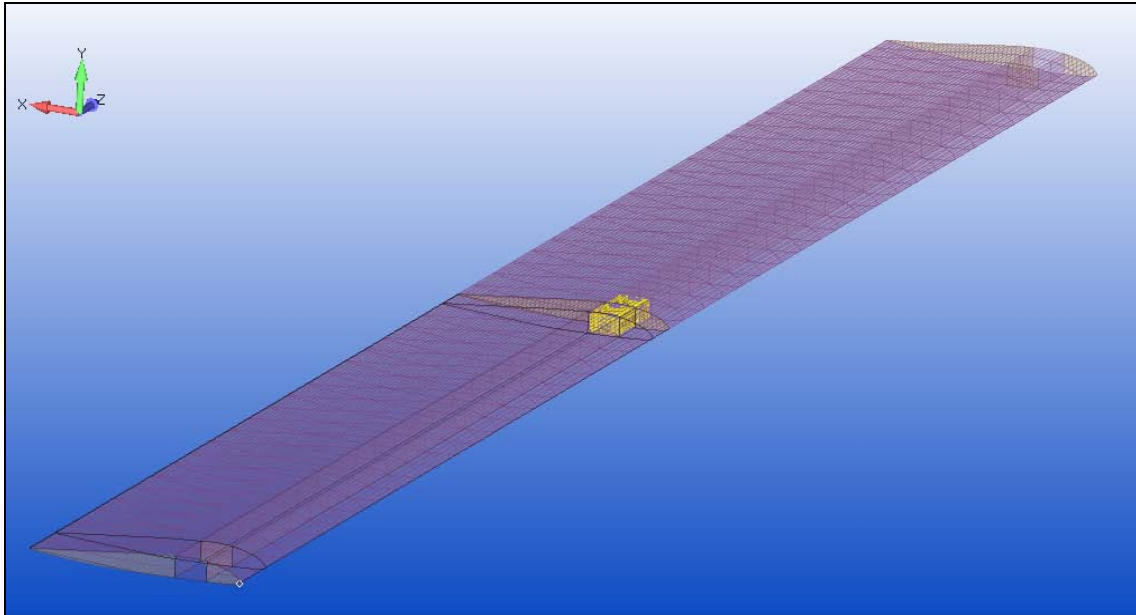


Figure 78. FE mesh of two wing sections with Al joiner (highlighted yellow)

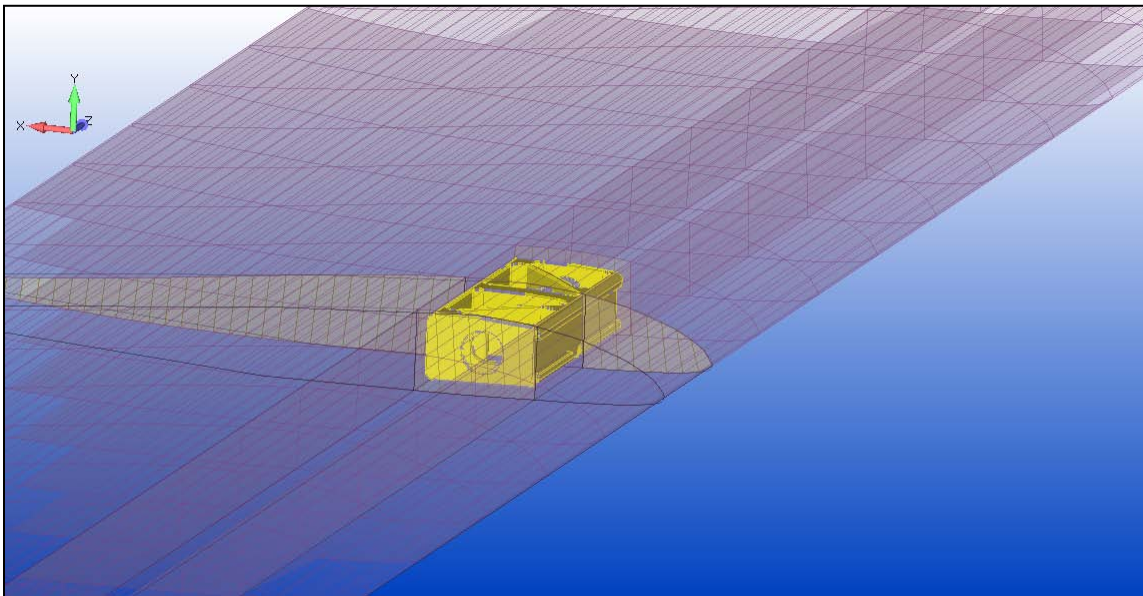


Figure 79. FE mesh of two wing sections with Al joiner (highlighted yellow)

The finite element mesh for the single wing was refined to the point of segmenting the end portions of the wing section such that the spanwise area contained within the respective wing clamps of the bending rig could be defined as separate surfaces and groups of elements. These areas also became the definition for those portions of the wing box which had no solid foam elements within the interior cross section, allowing for the ends of the wing sections into which the wing joiners are to be inserted. For the purposes of accurately isolating, defining, and locating the forces and constraints applied to the wing sections in the test rig, these segmented areas at the wing ends worked quite well. However, the areas did not correctly depict the true openings of the wing box. Specifically, the area where the bottom wing clamp constraint was defined was noticeably larger than the true opening. Upon initially adding the wing joiner into the model, these segmented areas did not provide ideal areas to represent the receptacle portion of the wing box.

Lessons Learned.

Throughout the modeling work conducted here several specific techniques were discovered which warrant mentioning. First among these was the choice to ultimately define loads by applying them to model surfaces instead of nodes. Once the model was created with areas representing those on the wing onto which the loads and constraints were applied, this method prevented the user from having to determine which nodes and elements of a mesh fit within a desired area. This was useful when adjusting the mesh sizing within a model and prevented having to redistribute loads among newly created

nodes or elements after each adjustment. However, this method necessitated caution when copying portions of the model, as the following discussion highlights.

When the modeling work progressed from the single wing to the two wings joined together, much of the previously created model was merely copied and pasted alongside the first half. While this effectively saved time and effort, the order for which items were copied became quite important. The original geometry and mesh of the single wing could be copied and placed in the new location. The loads used to bend the model could also be moved by defining them on the new end of the double wing section. However, since the copied mesh had not been meshed from the copied geometry, the loads that had been placed on the end of the copied wing surface weren't actually associated with the copied mesh underneath them. This portion of the new mesh where the loads were applied had to be recreated in order to be effectively associated with the copied surface and for the loads to have any effect on the finite element mesh.

A few limitations of the graphical interface were encountered during this effort. When attempting to combine the wing box and airfoil models it had been assumed that many key points or curves of the respective geometries were located at the same points within the modeling environment. But what often appeared to the user as coincident points or curves often were actually offset by a very small distance. Many different techniques, some more successful than others, were attempted to join portions of the model when necessary. Ultimately, realizing this difficulty early on in the modeling process may allow the user to prepare and allocate suitable time and energy to address these illusions.

In contrast to the above limitation, many graphical details were extremely helpful in analyzing various behaviors of the model. Specifically, when the color contour plots were activated and set to Total Translation they allowed the user to identify exactly what parts of the model deformed. When the lower wing surface of the single wing model actually deflected through the upper surface, the maximum translation results were initially assumed to be those of the upper surface. It was only upon activating the color contours when it became obvious which portion of the model was experiencing maximum deflection.

During the meshing process, the "Mesh Control / Size along Curve..." command proved most useful. Even when meshing solids or surfaces, this technique of defining the mesh size was preferred. When attempting to align the mesh sizing along the span of the wing model between two or more pieces of geometry, such as the wing box and airfoil, this command created meshes of both plate and solid elements with coincident nodes located as desired.

The methods used for simple acts such as selecting entities within the model were important. For example, selecting by element TYPE was used often. When removing rigid elements along the wing edge it was a significantly easier and faster method to use the toolbar and select Delete... Model... Element, Method... Type, and choose the intended element (in this case, "29. L Rigid") instead of selecting them individually. As another example, using a box to select portions of the model instead of individually selecting elements or nodes was a significant aid. When merging nodes within a certain distance between the wing box and airfoil, the box selection method prevented the accidental selection of those nodes along the trailing edge of the wing. This also helped

when modifying the properties of the elements of the wing box. On that note, the use of multiple property definitions, even for the same material definition, was extremely helpful for modeling the wing box. By using the "Modify / Update Elements / Property ID" command, the properties of the wing box plate elements were easily changed to reflect their increased layer thicknesses.

IV. Results and Discussion

The overall quality and utility of the FE models that were created is discussed here. Results are presented first for the model of the three-point bending test and second for the model of the bending rig test. Modeling of the bending rig tests included joined two-wing test sections, although the majority of FE work conducted dealt with the single wing models.

Three-point Bending Test

As described in Chapter II, a joined two-wing portion of an early X-HALE design was subjected to bending loads from a three-point test set up. The wing structure was subjected to loads of 20, 30, 40, 50, and 60 lbs via the loading cycle shown in Figure 22. The distance the joint section of the wing translated was measured from a horizontal reference line connecting the trailing edge wing tips, as seen in Figure 80. Deflection data were measured throughout loading by the University of Michigan team and are shown versus time in Figure 81. In order to compare these data to those produced from the FE models, deflection results of the three-point bending test were extracted from the loading and deflection plots shown here.

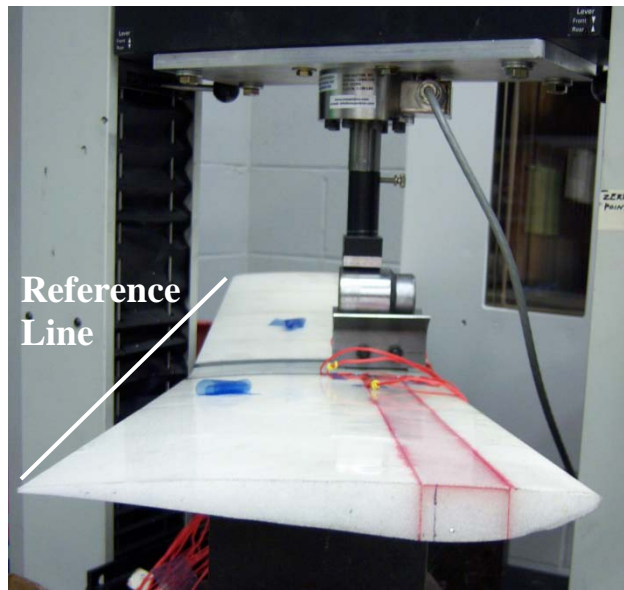


Figure 80. View of 2 m wing section subjected to 3-point bending test showing deflection reference line between wing tips

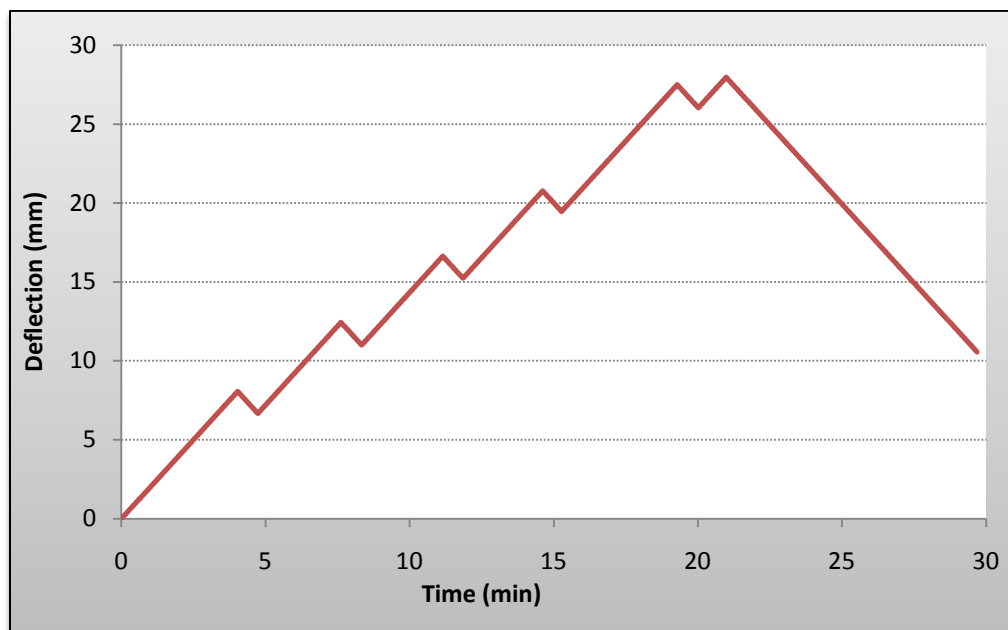


Figure 81. Deflection of wing joint vs. time resulting from 3-point bending test

Deformed Geometry.

The final model developed for this section, Model 8 included the fiberglass wing box, airfoil, foam core, and joiner block. As expected, this wing model deformed symmetrically, which can be seen in Figure 82. Also unsurprising was the realization that the inner elements of the two wing sections separated slightly at their joint, as shown in Figure 83. This figure also shows the protrusions of the lower surface of the joiner block through the bottom surfaces of the wing box and airfoil. This occurred because the solution to the contact problem was not implemented in this model. While it is not visible in these figures, the deformation of the wing model was uniform throughout the wing chord from leading to trailing edge.

Stress Contours.

Stress was also calculated for many of the wing FE models. Viewing stress levels throughout the model helped to confirm that the FE models developed behaved in a realistic and anticipated manner. Evaluating stress concentrations may also be used in future analyses to determine if the design configuration of X-HALE should or could be changed. The stress contours for the plate elements of Model 8 are shown below in Figure 84. Stress was highest near the joiner and decreased to essentially zero at the roller locations and beyond. The high stress region near the center of the airfoil is shown in Figure 85. These stress concentrations closely matched expectations and provided a confidence check of the validity of Model 8. The maximum stress was determined to be approximately 18 ksi, well below the tension yield limit of 78.9 ksi for the E-Glass.

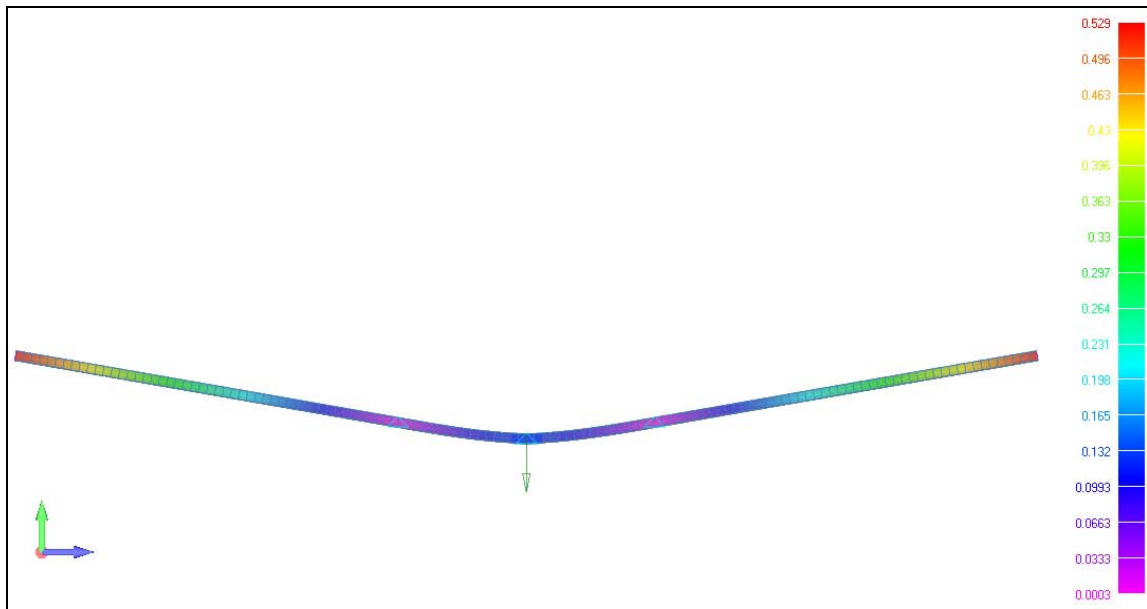


Figure 82. Front view of Model 8 showing deformed mesh geometry (color contours indicate total translation)

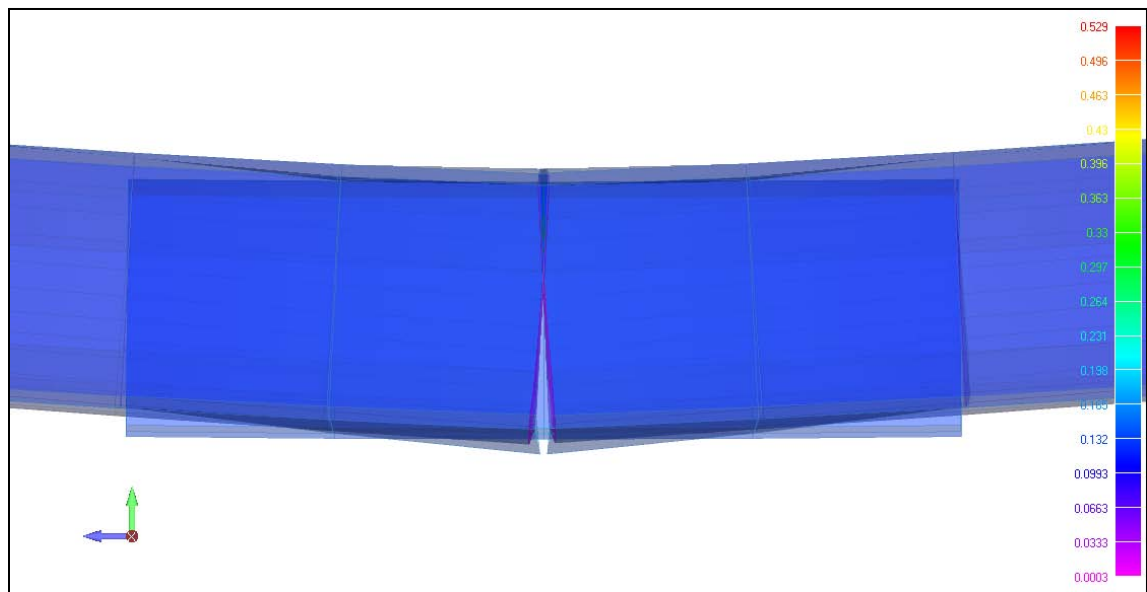


Figure 83. Close up view of Model 8 mesh at the joint showing separation between elements of each wing section as well as joiner protrusion

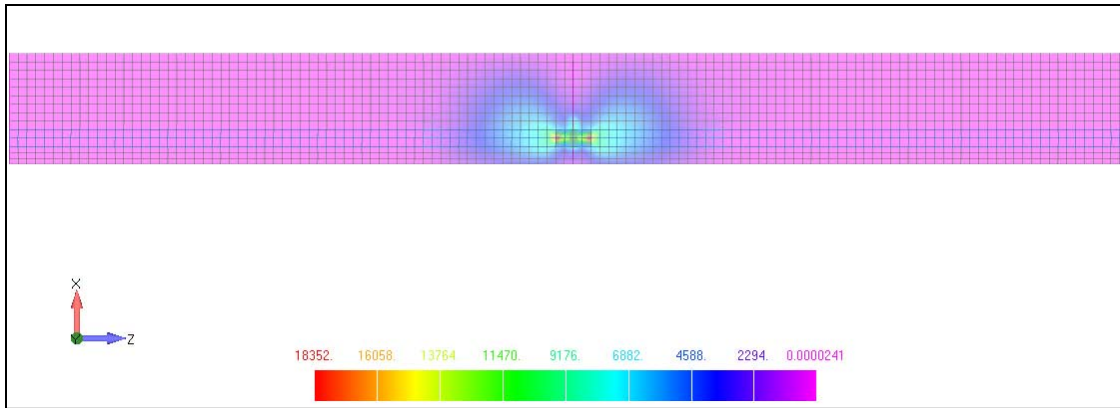


Figure 84. Plate Stress Contour (Model 8, 60lb load)

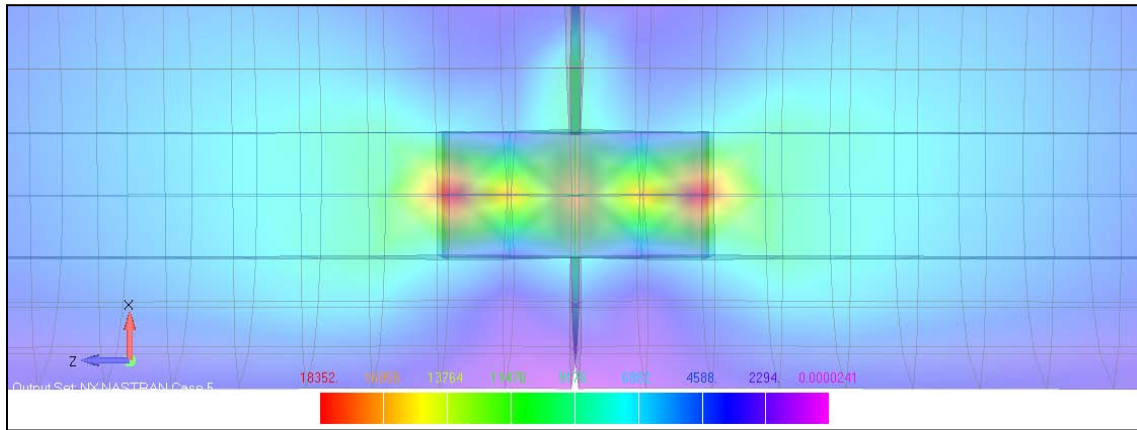


Figure 85. Plate Stress at Center of Airfoil (Model 8, 60lb load)

Comparison to Laboratory Data

The development of the models was discussed in detail in the previous chapter. A summary of the eight major FE models used to analyze the three-point bending test is again shown in Table 2 for reference. As a reminder to the reader, all variations include characteristics from the previous model, except for the contact surfaces which were only utilized in Model 5.

Table 2. Summary of FE models and descriptions

Model 1	Single 2m Wing Box section with pinned roller constraints
Model 2	Single 2m Wing Box section with fixed X & Y constraints
Model 3	Two 1m Wing Box sections with a wood joiner bolted to the wing box
Model 4	Two 1m Wing Box sections with foam added to wing box
Model 5	Two 1m Wing Box sections with contacts between the joiner block and wing box
Model 6	Two 1m Wing Box sections with airfoil added
Model 7	Single 2m Airfoil section with foam core added to airfoil
Model 8	Two 1m Airfoil sections

The actual test subject deformed linearly throughout most of the test. Therefore, a linear analysis was applied to the models. Figure 86 presents the deformation of each model with respect to the applied load as compared to that of the lab test.

As the model of the wing evolved from Model 1 to Model 8, its physical representation became more like that of the actual test article and it should have become more realistic. However, none of the model results closely matched the measured displacements from the laboratory test, but rather indicated the models were stiffer than the actual test wing section. Despite this, the general trends from these results did make sense among the versions of the wing models. Models 1, 2, and 7 were all created as single models, 2 m in length. The elements at the center joint were connected (i.e., coincident nodes were merged), producing one spanwise group of attached elements. It would make sense that such a model would act stiffer than a similar model separated into two 1-m sections joined together only by the joiner block within the wing box. And in fact, Models 1, 2, and 7 displaced less than the other models.

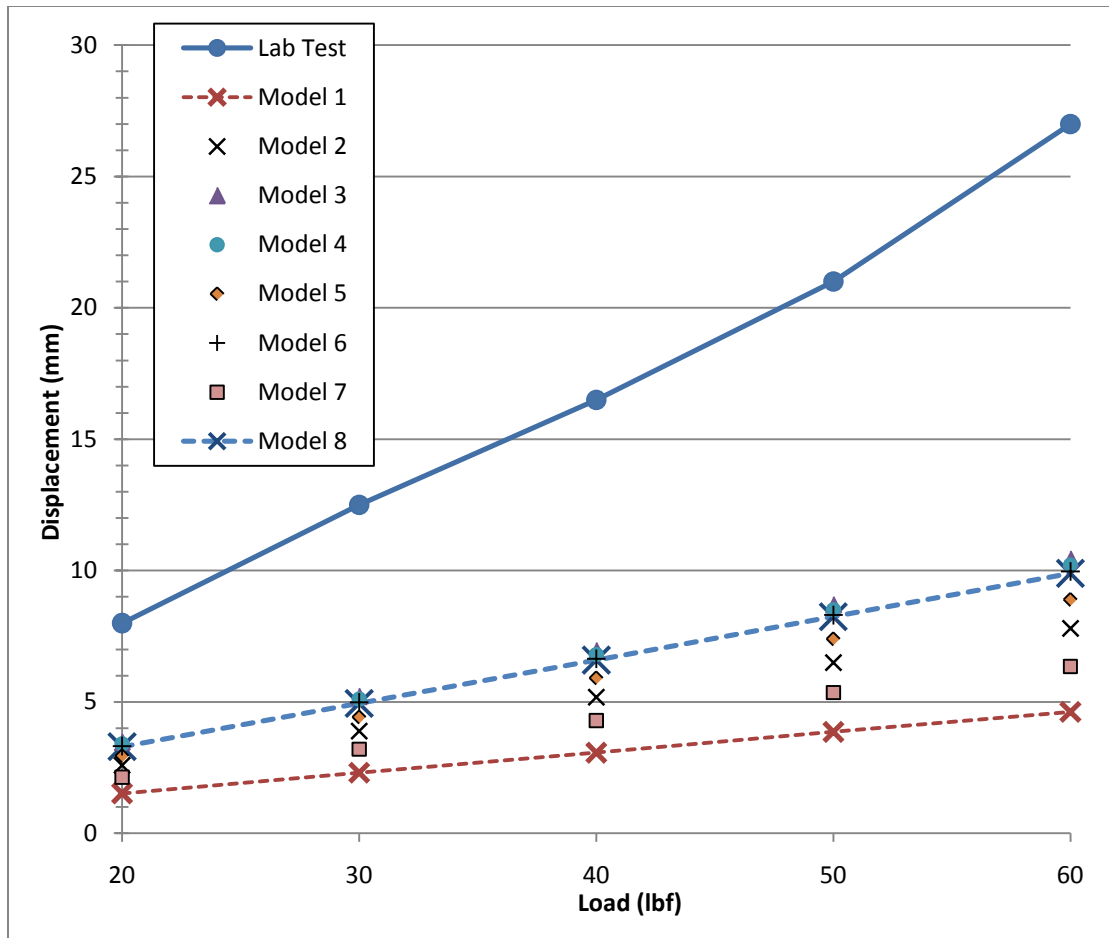


Figure 86. Comparison of load vs. displacement results amongst lab and 8 FE models

Although it was shown that including the solid foam within the airfoil was important for the behavior of the wing skin at specific points along the wing, the data indicated the inclusion of foam did not provide much additional stiffness. The only difference between Models 3 and 4, and likewise between Models 6 and 8, was the addition of foam to the later of each pair. Yet displacement results for Models 3, 4, 6, and 8 were nearly identical, as can be seen by their overlapping data in the graph. This not only seemed to confirm that the inner foam core had little effect on the stiffness of the

overall wing section, but also indicated that the wing box indeed contributes most of the structural stiffness to the wing section.

Finally, the inclusion of defined contact surfaces in Model 5 seemed to slightly increase its stiffness as compared to Model 4. Again, this would make sense as constraining the joiner block and surrounding wing box elements around the joint location in such a way would be expected to increase the stiffness of this area of the wing section.

When considering the significant difference between the bending results of the lab test and the FE model, the material properties were again examined. If the effective properties of the fabricated wings were not the same as those defined for the FE models, errors such as those seen above could result. The fiberglass material used to manufacture the wing sections used in the lab test may have been difficult to manufacture to the listed properties. Regardless of the reason, the X-HALE wing sections which were physically produced may have turned out having material properties which made them more flexible than those published by the manufacturers of the composite materials. Two possible examples of such different material properties are 1) a reduced thickness of each fiberglass layer and 2) a reduced effective modulus of elasticity (Young's modulus). FEMAP allows for the modification of such material properties without otherwise needing to change the FE model. A cursory analysis of how adjusting these two properties would affect the wing was performed.

First, the thickness of the wing box was reduced to 80% of its design value. The model was then re-analyzed for all loading conditions. Second, the Young's Modulus value was reduced to 80% and the model was again analyzed. Finally, analysis was

performed for all loads with both the wing box thickness reduction and the Young's Modulus reduction applied to the model. These analyses did result in a somewhat more flexible structure. The 80% thickness and 80% modulus versions of the model each produced approximately 20% more deformation, and the combination of these changes resulted in 50% more deformation (see Figure 87).

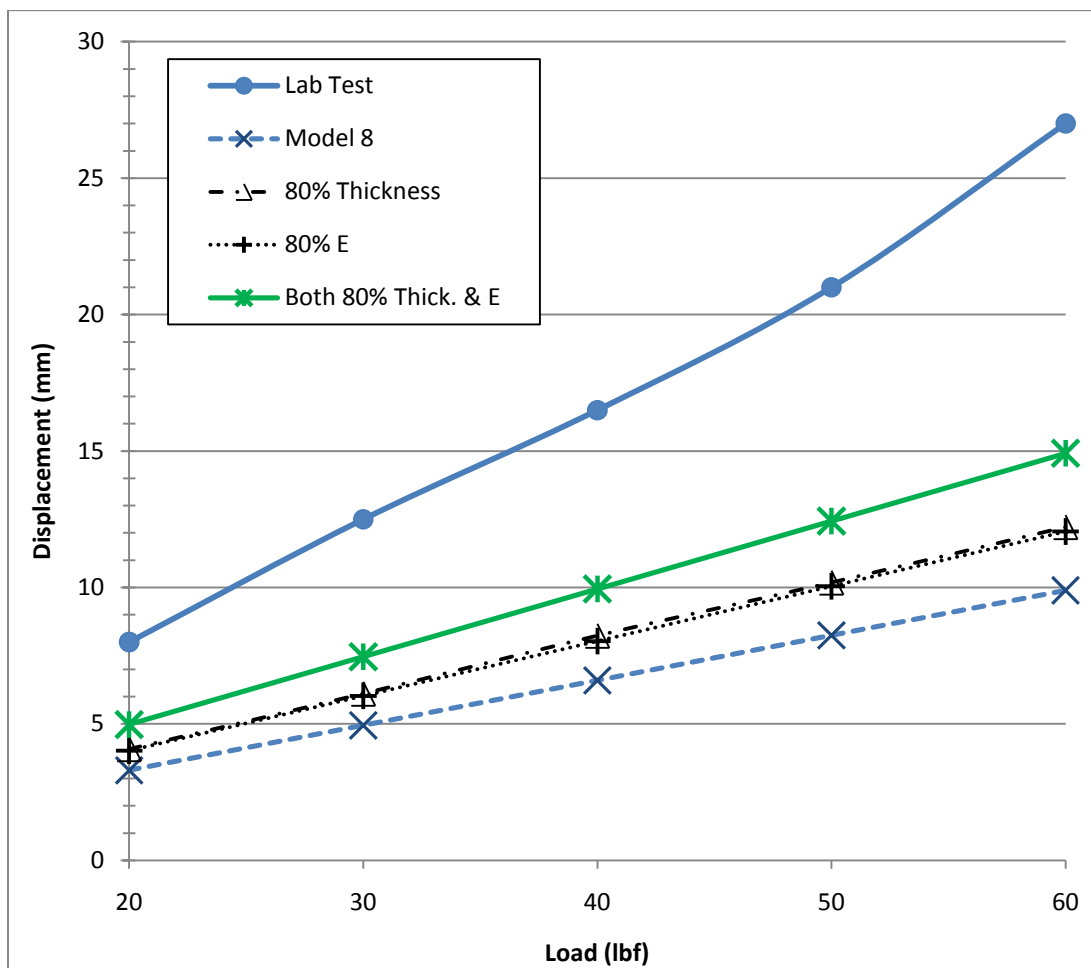


Figure 87. Comparison of displacement results between lab test, Model 8, and 3 versions of Model 8 with modified material properties

The results above suggested the material properties of the fabricated wings were not equal to those prescribed by the material manufacturers. These modifications to layer thickness and Young's modulus were the only property changes made to Model 8. Additional adjustments are required to determine the degree of difference between these material properties. There may also be additional explanations for the deflection differences, such as poorly defined connections and overly simplified assumptions. Likewise, these possibilities would need to be investigated to determine their affect on the deflection results.

Quality of Load and Boundary Condition Definitions.

Some improvements could have been made to how the loads and constraints were defined in the FE models. One such improvement would have been obtaining actual dimensions of the load and roller devices, specifically in the direction of the wing chord. The placement of the loads and constraints could then be refined. As it is, the model assumes that the load and constraints are distributed across the wing box section alone. This was mainly done to simplify the modeling process. Another area for improvement would have been changing nodal loads to nodal deflections. Using deflections would more closely simulate the actual test conditions in which a solid bar loaded the wing box. Also, increasing the number of wing box nodes in the chord direction would more evenly distribute the load, further increasing the accuracy of the model.

Additional Comments Regarding FE Model Quality.

While numerous simplifying assumptions were made to allow immediate and rapid modeling of the three-point bending test, many of these could be removed or modified to further refine the model. For example, including the pieces of the wing which were constructed from carbon fiber would allow the model to account for interactions between more materials and, in turn, improve the fidelity of the model. Also, appropriate contact surface definitions should be included in the model. This could allow for the discovery of issues within the wing joint where the wing box and joiner block are fastened and results in a redesign. A more mature model of the screws which fasten the wing sections should also be added. This could be as simple as adding spring elements to account for the play at the joint or as complex as actually modeling the physical screws and defining contact surfaces between the screws and the joiner block material. Regardless of the approach, testing of the physical connection should also be conducted in order to properly refine the screw model.

Regarding the various materials which comprise the wing section, their properties should be tested enough times to yield confident values for the actual wing box strength and stiffness. This is especially true for the composite materials, as many variables exist which can affect their end state properties. Testing representative parts of the X-HALE structure is probably the most effective way to address the differences between model and laboratory test results. Vibration testing could also be conducted. This would provide additional data which could be compared to modal results from FEMAP. Finally, the correct mass of the model should be accounted for. While this would likely

not significantly affect the results of static testing, it would allow for accurate dynamic tests to be performed and would further increased the validity of the model.

Bending and Torsion Rig Test

As described in Chapter II and the report by Matthews, four X-HALE wings sections were subjected to bending and torsion tests in the characterization rig at the University of Michigan [21]. Once a standardized test procedure was finalized, the resulting wing tip deflection measurements were recorded for applied loads of 3, 4, 5, 6, and 7 N. For purposes of comparing to the FE models developed here, only bending test data will be referenced. Additionally, the data collected by Matthews has been separated and only the average wing tip deflection measurements for the tests when bending was conducted towards the top surface of the wing will be discussed in this section. The graph in Figure 88 displays the average deflection at the free end of the wing section for each of the four wing sections tested as single wings spans. Similarly, the graph in Figure 89 displays the average deflection at the free end of the wing section for each of the two sing sections tested as joined double wing spans.

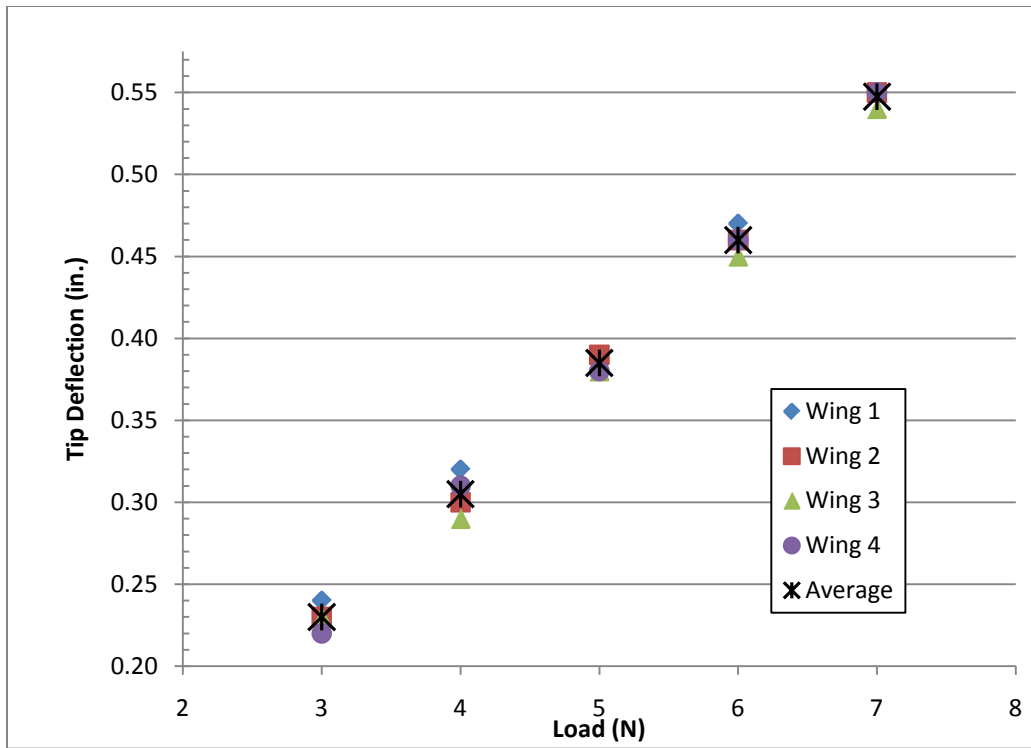


Figure 88. Wing tip deflections for 4 single test wing sections under loading conditions

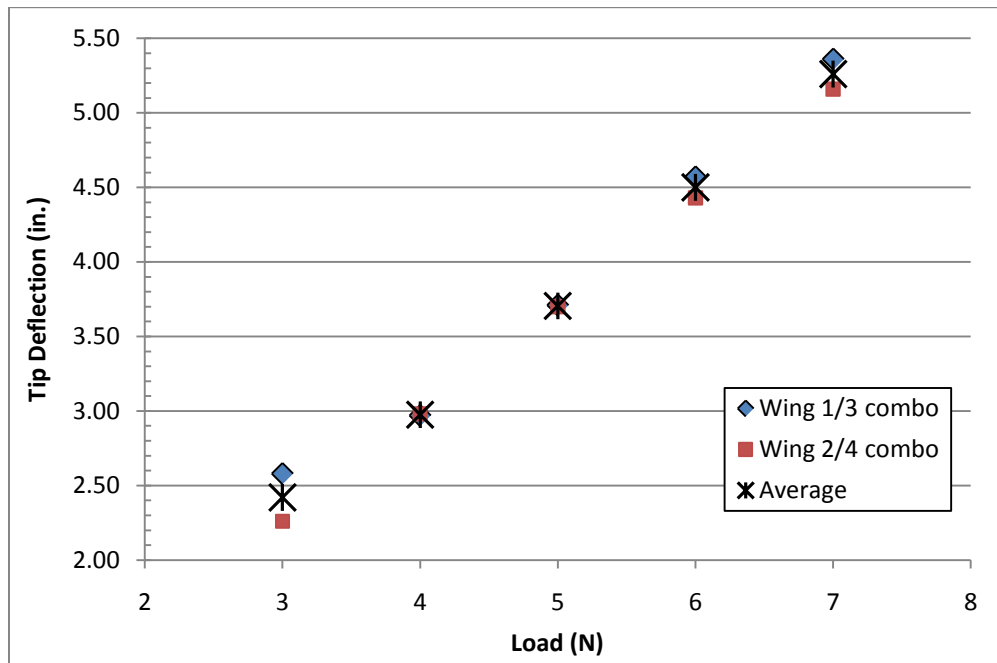


Figure 89. Wing tip deflections for 2 joined test wing sections under loading conditions

Deformed Geometry.

After separate finite element models of the wing box and airfoil had been developed, they were each subjected to the bending loads used in the laboratory bending tests. For all load cases, the maximum total translation occurred at the free end of each model. This was readily apparent when viewing the deformed FE mesh of each model with color contours set to Total Translation. Figure 90 shows the post-analysis results of the wing box model under the 3 N load, indicating a maximum 0.345 in. total translation.

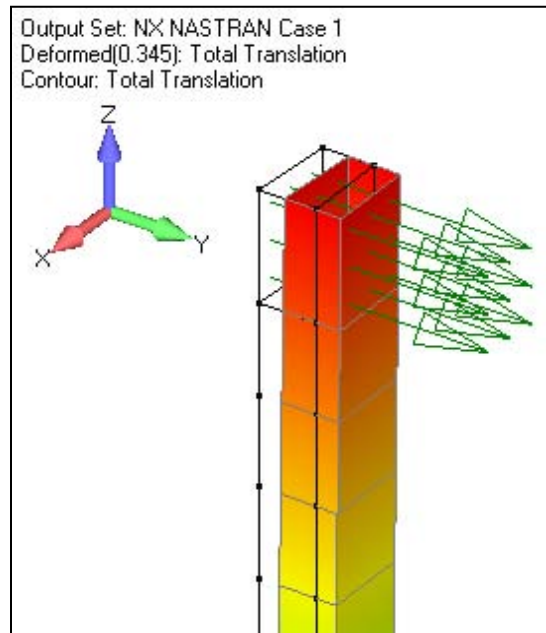


Figure 90. Free end of wing box model showing total translation under applied load with original position of wing box outlined

The maximum values were recorded for all five load cases. Table 3 compares results from the laboratory tests with those of the FE models. The average of all four single wing section tip displacements recorded in the lab are shown along with the

maximum tip displacement value for both models. The percent error between results from each model and the laboratory value was calculated and is also presented in the table. These deflection figures agreed with initial expectations that the wing box would be the primary source of structural stiffness for the wing. While the tip deflections of the wing box model were greater than those of the laboratory tests, they were much closer than the airfoil model tip deflections. There was no intention to use either of these models alone; rather, this point in the modeling process served as another sanity check. If, of the two models, the wing box model behaved more closely to that of the actual test article, then it was assumed the model with wing box and airfoil combined would behave even closer to the true wing section.

Table 3. Comparison of laboratory and FE model wing tip deflections for five load cases

	.674 lb (3N)	.899 lb (4N)	1.12 lb (5N)	1.35 lb (6N)	1.57 lb (7N)
Lab Results (Average)	0.23 in.	0.31 in.	0.39 in.	0.46 in.	0.55 in.
Wing Box only model results	0.345 in.	0.461 in.	0.576 in.	0.692 in.	0.805 in.
(% error)	50%	51%	50%	50%	47%
Airfoil-only model results	0.752 in.	1.009 in.	1.262 in.	1.515 in.	1.762 in.
(% error)	227%	231%	228%	229%	222%

When analysis was performed on the initial model of the combined wing box and airfoil the overall deflection at the wing tip was still larger than the lab results, and in fact very similar to the 0.752 in. wing-only result above. However, the Wing Box properties had not yet been increased appropriately as discussed in the previous chapter. Once the material properties of the wing box walls were increased to more accurately represent their fabrication thickness, significant effects were seen in the deflection results. In fact, the increase in thickness of the fiberglass elements along the top and bottom surfaces to account for both airfoil and wing box had the greatest effect in the model. While increasing the leading and trailing edge wing box wall thicknesses to five layers did slightly reduce the bending of the wing, the change to the top and bottom surface elements reduced the bending by almost 50%. For an applied force of 0.67 lb (3N), this combined wing box and airfoil model now produced tip deflection results of only 0.276 in., which corresponded more closely with the lab results shown above. Figure 91 shows the post-analysis results of the improved model under this applied load, with the undeformed structure represented in blue-gray and the deformed structure represented by the color contour FE mesh. Deflection results using this Airfoil and Wing Box model were much closer to the lab results for all five load cases. The difference between the deflection results did increase as the applied load increased.

The number of elements along the wing span inward from the mount sections was increased from 10 to 20 and, as expected, the differences between FEMAP results and those from the lab test increased somewhat. This was likely due to the added effective flexibility resulting from increasing the mesh size spanwise. When reviewing the results of the five cases (turning off Actual Deformation and looking at the exaggerated

deflection) it was discovered that some of the lower surface of the wing was still protruding through the top surface. This occurred along the trailing edge portion of the wing where the load was applied. Another row of rigid elements was added inward from the edge of the wing. This prevented the lower wing surface from deforming through the top surface. In order for the portions of the model forward and aft of the wing box to match, rigid elements were also added at the free end of the model forward of the wing box. Figure 92 compares two exaggerated views to illustrate the effect of the rigid elements.

After running analysis on this updated model, the differences between FEMAP and lab deflections were between 0.01 and 0.02 inches. Next, full multi-load analyses were performed for the simple wing box model with solid foam elements added. Total tip deflection results for this combined model were 0.343 in., 0.458 in., 0.572 in., 0.687 in., and 0.799 in. for loads of 3N, 4N, 5N, 6N, and 7N, respectively. Referring to Table 3, the wing box tip deflections with and without solid foam are nearly identical; all are within 0.006 in., differences of only 0.6 to 0.8 %. Finally, the combined wing box and airfoil model with solid foam elements added throughout was analyzed for all loading conditions. Immediate observations of the resulting deflections showed logical and expected behavior, as illustrated by the evenly distributed translation contours seen in Figure 93.

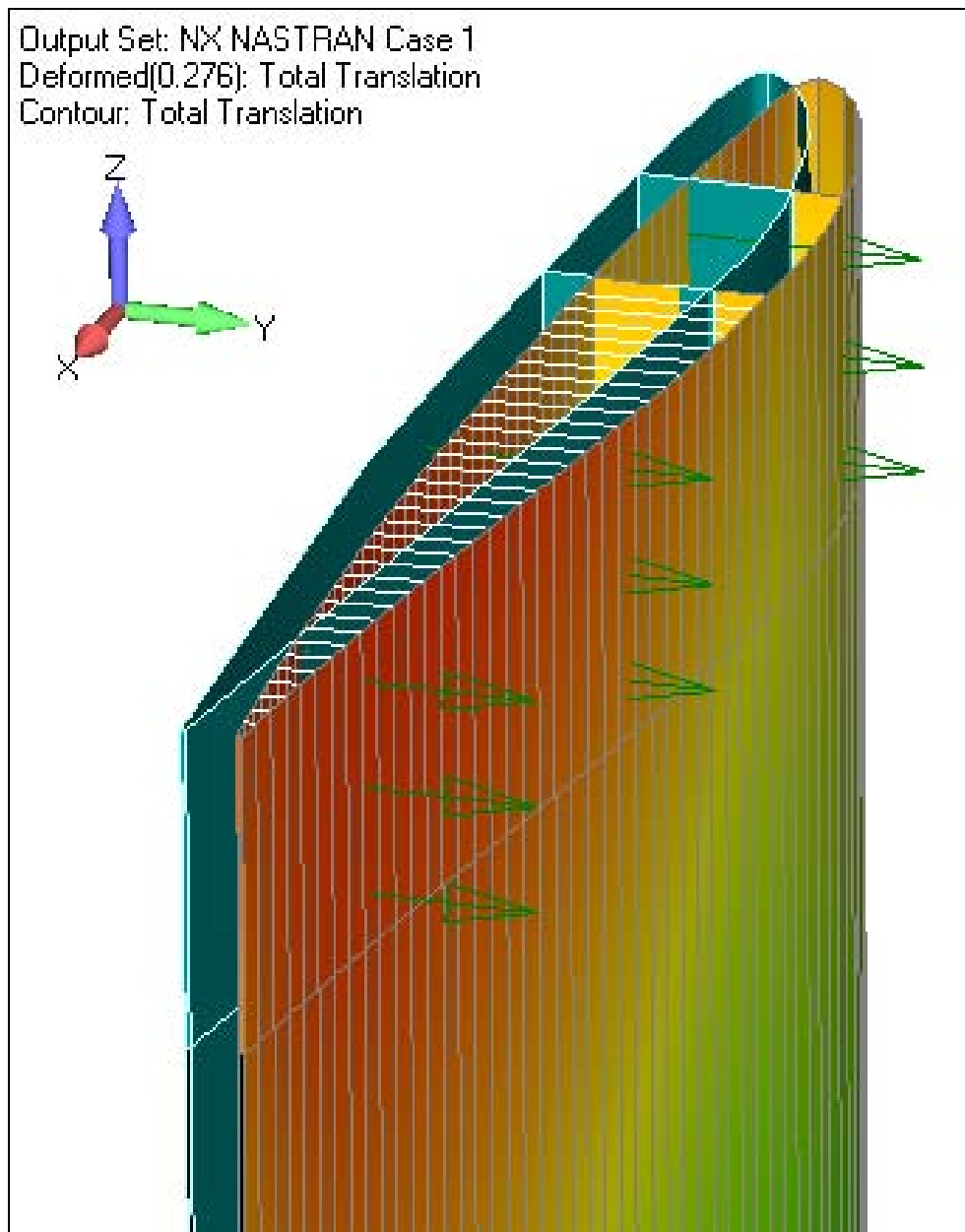


Figure 91. Deflection of combined wing box / airfoil model for 0.67 lb (3N) applied load (0.276 in. maximum deflection indicated)

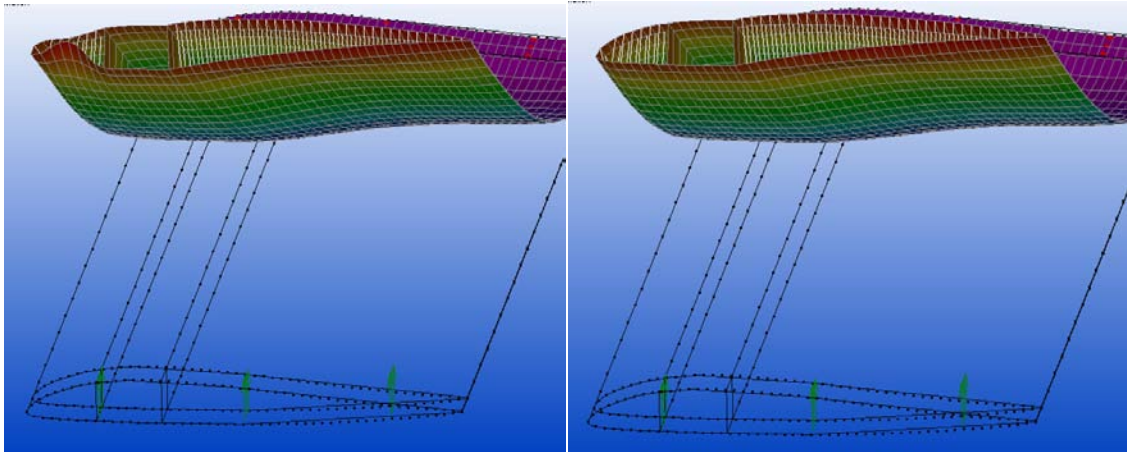


Figure 92. Exaggerated deflection of wing mesh showing deformation without (left) and with (right) rigid links between airfoil surfaces forward of the wing box

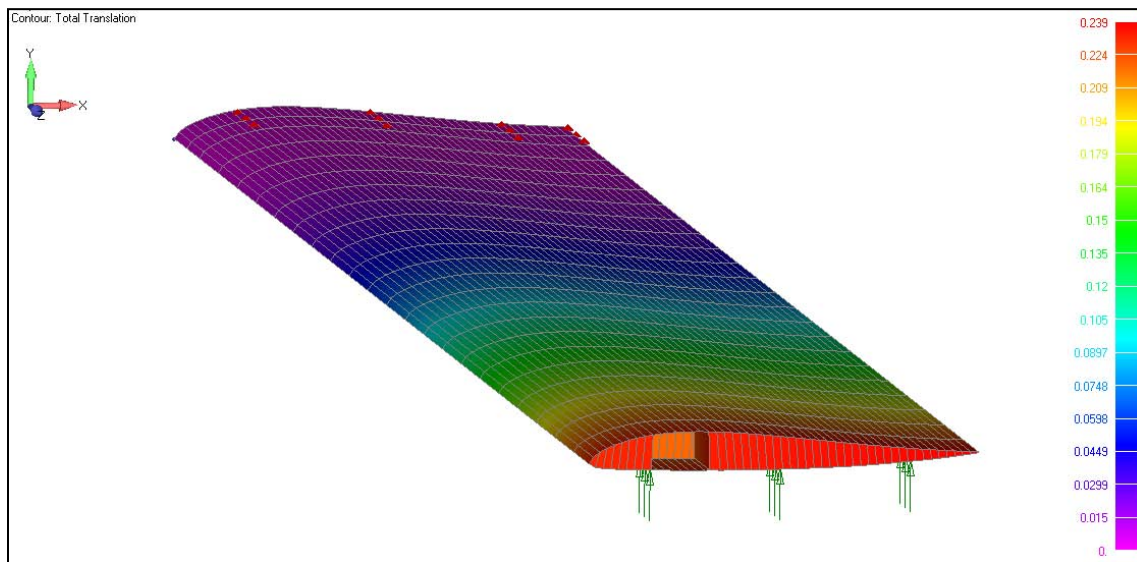


Figure 93. Mesh of full wing model showing translation contours

The deflection calculations of this final wing model closely matched the deflections from the static laboratory tests. Specifically, the results of the linear analysis for the wing subjected to 3, 4, 5, 6, and 7 N loads yielded deflections of 0.239, 0.319, 0.399, 0.478, and 0.558 in., respectively, all of which were less than a 5% error from the lab result averages. Post-analysis depictions of these actual deformations can be seen in the series of FEMAP screen shots in Figure 94. To further check the reality of the wing model produced to this point, the additional loads described in Chapter III and depicted in Figure 68 and Figure 69 were applied to the model. These were not loads representative of any laboratory test previously conducted. Rather, these were intended to subject the wing model to relatively extreme loading conditions to test the overall connectedness of the finite element mesh.

Using the NX NASTRAN linear static solver, the simplified two-wing model was analyzed for all five loading conditions in the same manner as the single wing model. Post analysis inspection indicated results closely matching those from the two-wing laboratory tests. The tip displacement of the model corresponding to a 3 N load was 2.091 in. – a 13.6% error, and the largest of the five cases. Displacements for the 4, 5, 6, & 7 N loads were 2.806 in., 3.508 in., 4.21 in., and 4.913 in., respectively – all errors of only 5% to 7%. The extremes of these tip deflections for the simple two-wing model under a load of 3 N and 7 N are shown in Figure 95 and Figure 96, respectively.

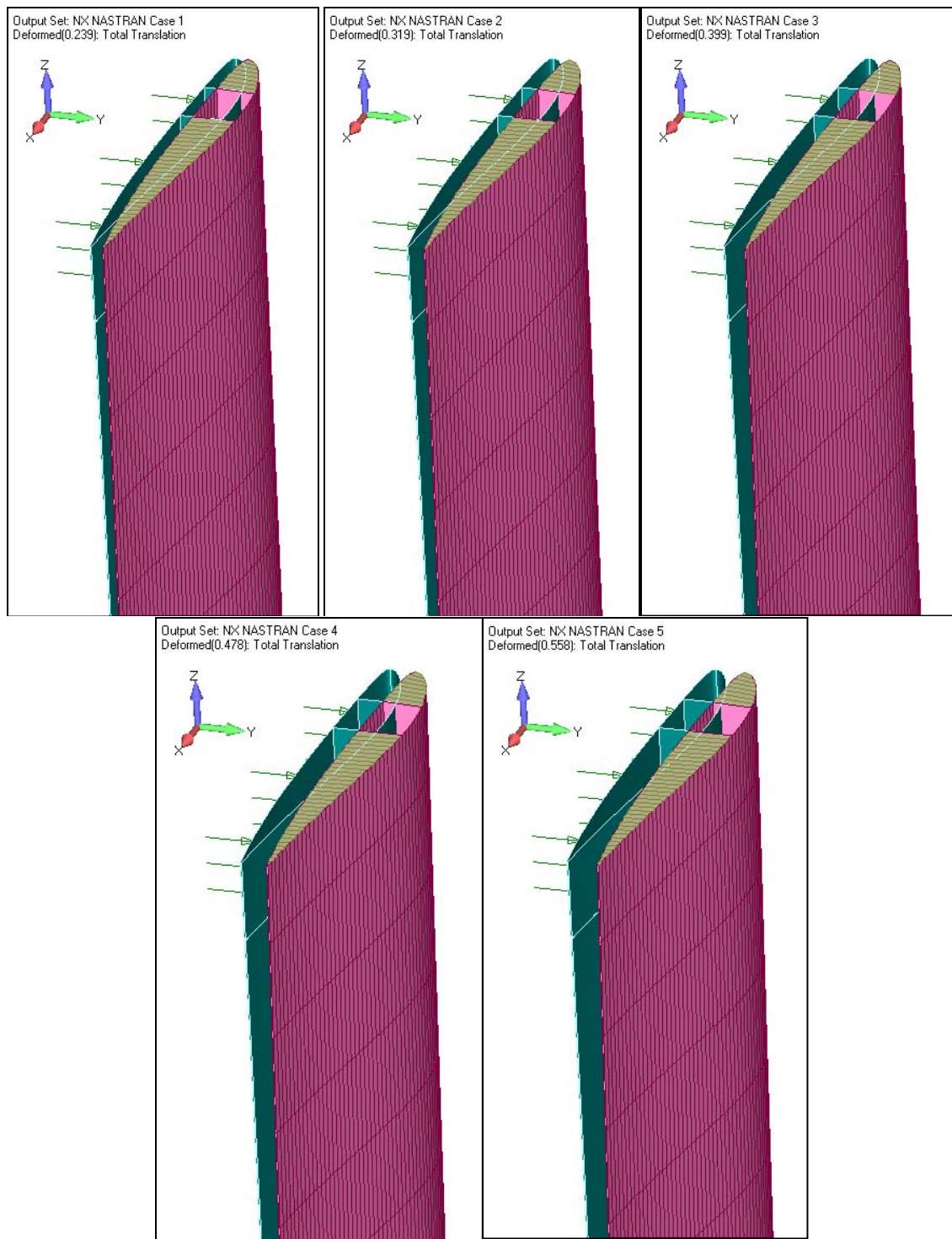


Figure 94. Deformations of the final single wing model under 5 loading conditions (undeformed wing in blue/green)

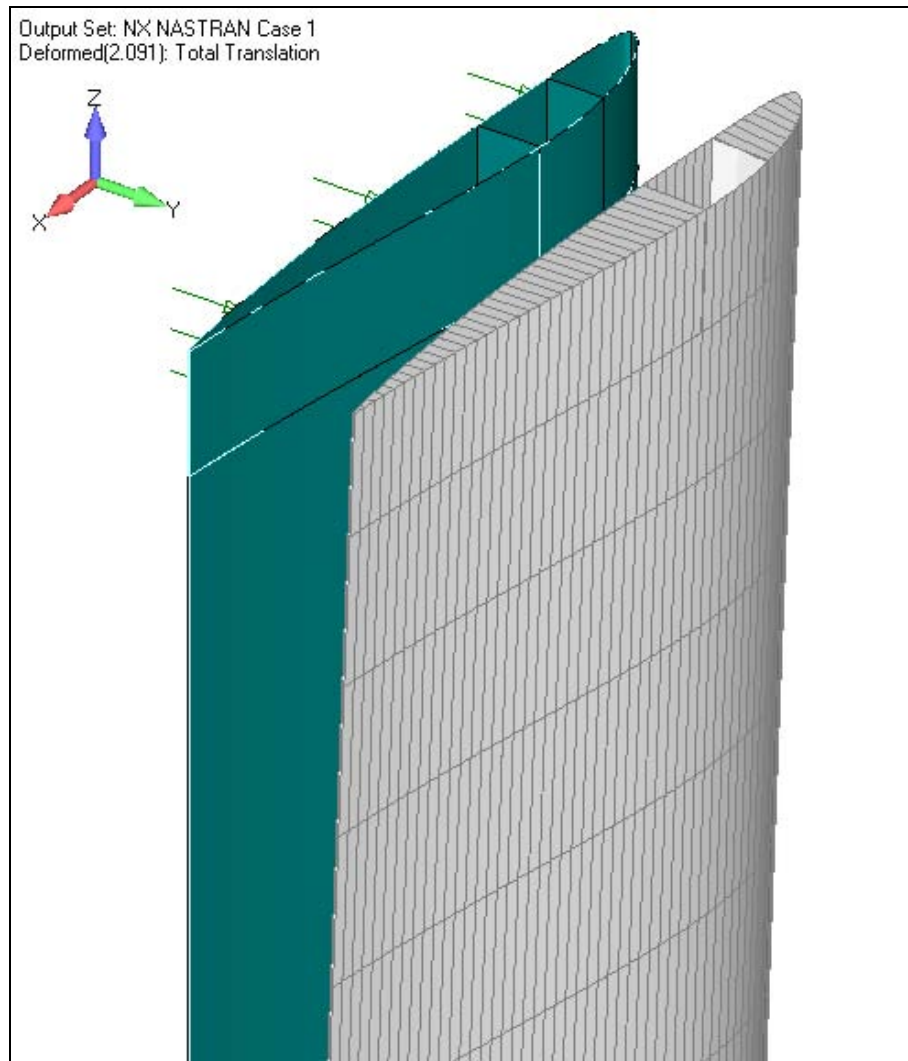


Figure 95. Simple 2-wing model under 3 N load showing original position (blue/green) and deformed position (gray mesh)

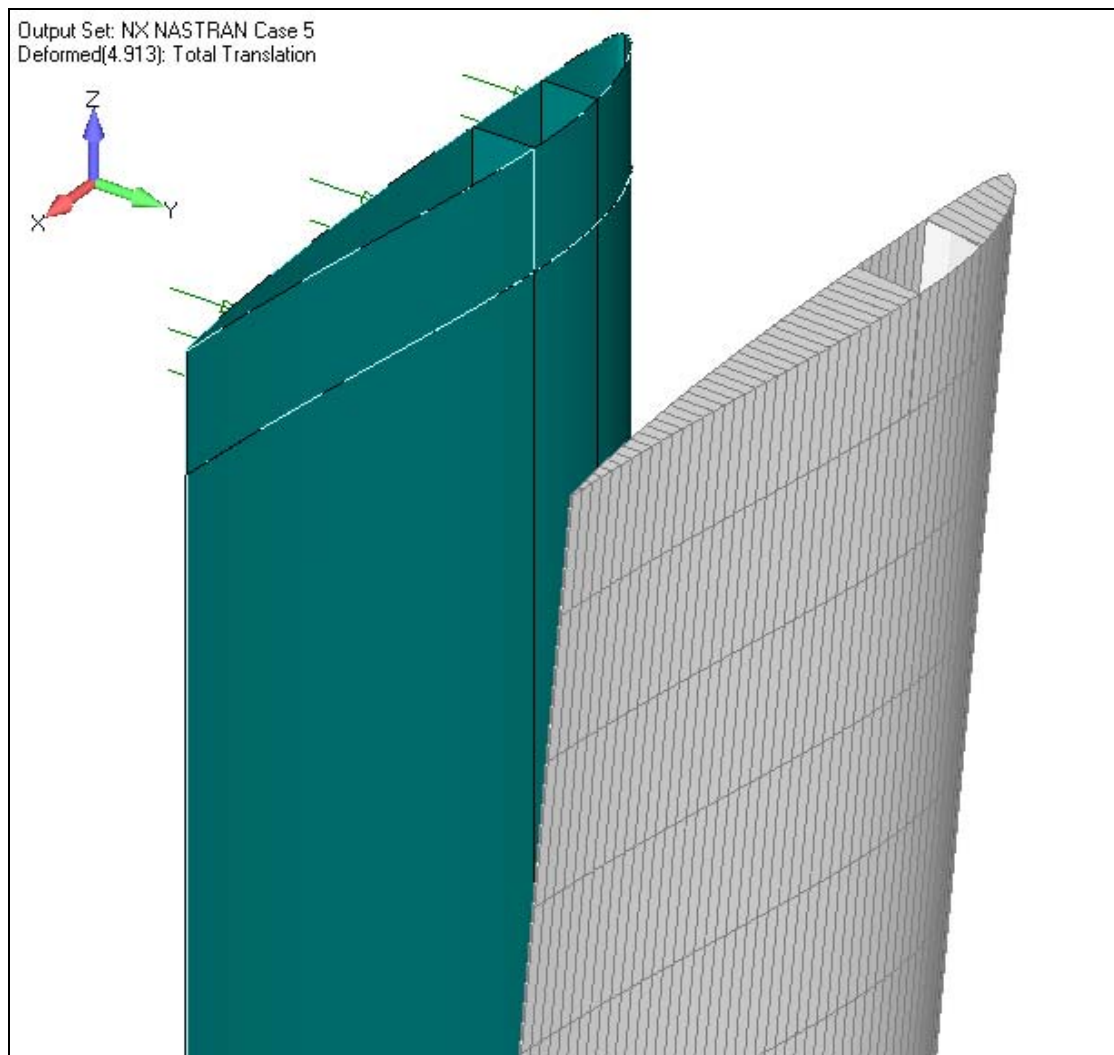


Figure 96. Simple 2-wing model under 7 N load showing original position (blue/green) and deformed position (gray mesh)

V. Conclusions

This work centered around finite element (FE) modeling and analysis of static laboratory bending tests conducted on wing sections of the X-HALE aircraft designed by the University of Michigan's Department of Aerospace Engineering. Results obtained for the initial set of tests indicated that there were possible errors between the material properties of the X-HALE wings tested in the lab and the FE models created within FEMAP. At the same time, the source(s) of the discrepancies between laboratory and FE displacement results could not completely be isolated to material properties – details such as connections and contact surfaces will have to be investigated further in order to determine their role in the behavior of the model. Regarding the analysis of the later tests performed with the characterization rig, results for wing tip displacements obtained from the FE models closely matched those from the laboratory. While the similarity in behavior between the models created and actual wing sections are promising, further work will be required to be able to truly describe the accuracy and validity of the FE models created.

The work conducted on the three-point bending test will likely not be extended beyond level described here. That test was performed on a joint section of the X-HALE wing which has subsequently undergone significant design changes. From a test perspective, subjecting the two joined wings to those bending loads revealed weaknesses in the original joint design, and as such was a successful test. From a FE modeling perspective, that test provided an initial set of data to which FE modeling data could be compared. The level of refinement of this initial FE modeling certainly left room for

improvement and further work. For example, the loading and boundary conditions could have been implemented more realistically by obtaining measurements of the actual load and roller devices, especially of their length in the direction of the wing chord. The model presented here assumes that the load and constraints are distributed across the wing box section alone, which may not be accurate. Many other examples of oversimplification exist. However, the additional effort that might have been put towards improving the model of the three-point bending test section will not be discussed here. Instead, additional modeling steps and insight into the modeling process which apply to the current FE model of X-HALE are offered below.

The assumptions made throughout the modeling process served various purposes. Why the assumptions were made, as well as the validity of the assumptions themselves, should be assessed as future work progresses. For example, the mass of the wing components were neglected. The gravitational forces on such a small composite and foam structure was assumed to be much less than the applied loading, and therefore would not impact the results. However, if additional tests are to be modeled the mass of X-HALE may come into play. Also, the assumptions regarding material properties may be invalid. Composite layup techniques may result in properties varying significantly from their published values. Regardless of the results obtained here, such variables could be a large factor in differences between test and model results. With additional time, and certainly before further modeling work is conducted, the material properties of the fabricated X-HALE structure should be determined. Primary focus should be on the wing sections, especially the composite materials, which should be tested enough times to yield a statistically significant value for the actual wing strength and stiffness. A

drawback to this recommendation is the requirement to manufacture additional wing sections for the sole purpose of performing material property tests, as these test section would like be damaged and therefore unusable in the aircraft.

Contact surfaces were discussed for the three-point test, but remain applicable for the later model and may likely prove to be a challenging detail of any FE model of an aircraft like X-HALE. For any work that continues on the joined wing version of the bending rig model, the contact definitions throughout the joint between the two wing sections will require significant focus. The early lessons learned regarding contact surface definitions should be applied to the portion of the two-wing model where the aluminum joiner block is fastened inside the open wing box sections of both wings. And unlike the original design of the wing joint where wood screws were used to connect the wooden joiner block to the wings, the current X-HALE joint employs a nut and bolt design which may present additional levels of complexity throughout its components. Regardless, appropriate contact surfaces will surely play a role in the fidelity of the model and adequate time should therefore be allocated towards that work.

Overall, this effort resulted in improved levels of confidence in how to appropriately apply the crucial steps of creating and working with FE models. Although important, these are only the early steps of the FE modeling process. Much work remains before a model can be used to fully analyze X-HALE's behavior in its anticipated environment. Work on the model of the joined two-wing section should be extended to a level at least equal to that which was conducted on the sing wing model. Finite element analysis could also be performed for the torsion tests to which the single and joined wing sections were subjected. And analysis of the bending and torsion tests should be

performed for both directions, as was done in the laboratory. However, the ultimate goal of creating a FE model of X-HALE was to compare its results to those obtained from actual flight tests. As with most flight test programs, delays prevented gathering any flight data at the time of this writing. But this end goal should not be ignored, and work should be continued to provide a more mature model by the time flight tests commence. While this limited set of finite element models cannot be considered validated for the purposes of characterizing X-HALE or its components, it does provide a starting point from which to continue as well as a set of lessons learned which will hopefully save time as this effort progresses.

Appendix

X-HALE Design Components

Fairings were used to aerodynamically shroud all five X-HALE motor pods. Figure 97 shows an off-angle and front view of the fairing design.

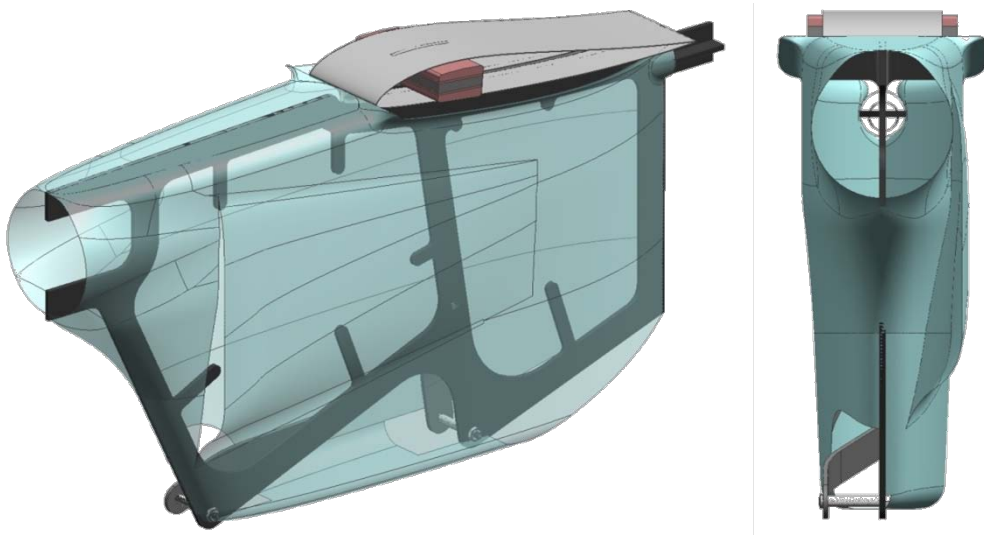


Figure 97. Off-angle and front views of fairing [28]

Connected to each motor and extending from the front end of each fairing was a propeller to provide X-HALE with the required thrust. Each propeller has a ground clearance of 1.5 in., while the bottom of each spine and fairing has a ground clearance of 1.0 in. A front and side view of a fairing connected to the aircraft can be seen in Figure 98 and Figure 99, respectively.

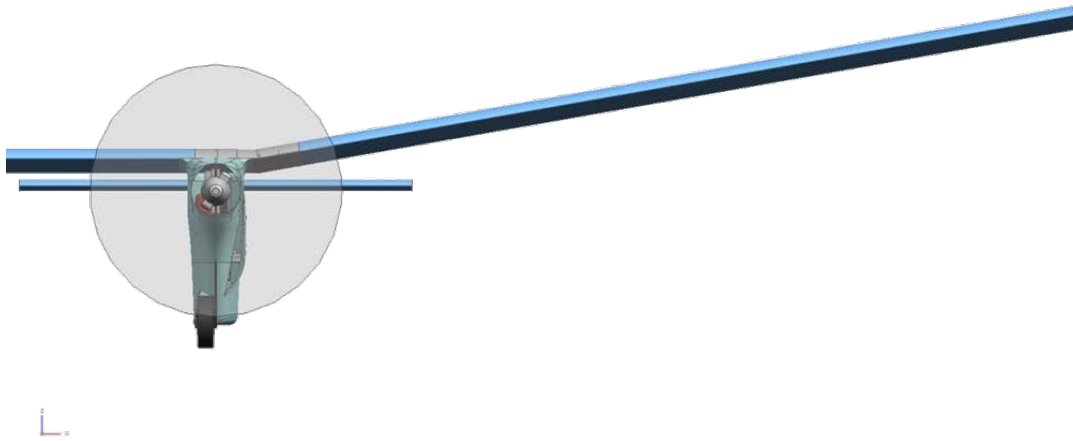


Figure 98. Front view of 6-m version of X-HALE showing dihedral wing joint

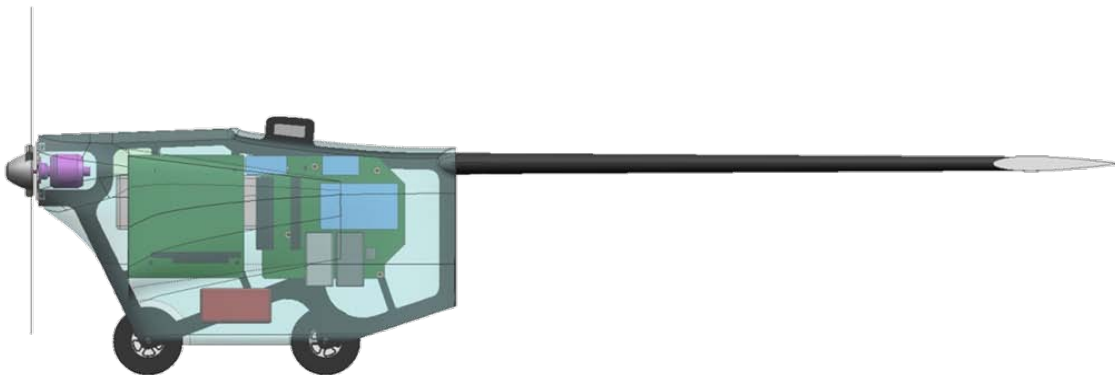


Figure 99. Side view of spine / fairing / tail section showing typical arrangement of internal electronics of each fairing

Within each of the motor fairing sections are a collection of necessary electronics. Included among these are on-board sensors such as strain gages and accelerometers to record wing deformations resulting from the planned excitations. The four outer fairings contain multiple electronics, including batteries, data acquisition computer boards, and a speed controller. Equipment within the center fairing includes an inertial navigation

sensor, a GPS antenna and receiver, modem, speed controller, and batteries. The ATV configuration of X-HALE will ultimately include strain gages and accelerometers throughout the structure.

X-HALE Fabrication

Foam Core.

One of the first steps in the construction of X-HALE wing sections was to create the foam core sections that fill the hollow space within the fiberglass wing box and airfoil. Acrylic templates cut by waterjet were made in the shape of the leading edge airfoil, wing box, and trailing edge airfoil cross sections. These templates were attached to the ends of blocks of Rohacell 31-IG foam which were then sanded into the corresponding shapes by using the templates as guides. Figure 100 shows pre-sanded blocks of foam with guides attached, illustrating the set up of this process.



Figure 100. Uncut foam blocks with acrylic templates attached prior to sanding

Wing Box.

After sections of foam were shaped, the process of laying up the wing box and airfoil continued using aluminum molds. The molds were machined to the shape of the upper and lower curve of the EMX07 airfoil from solid aluminum blocks (Figure 101).

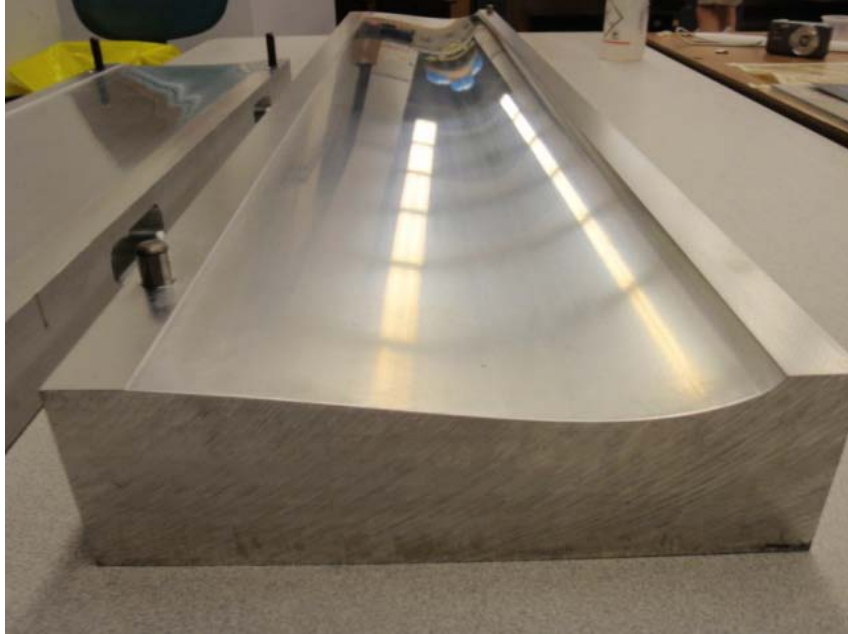


Figure 101. Aluminum wing mold used to shape and cure the X-HALE airfoil

The layup process began with the wing box – specifically, the ends of each one meter long wing box section, which would become the aircraft’s wing joints. Five layers of unidirectional carbon fiber tape were wrapped around 1.25-in. long mold inserts the shape of the hollow wing box (Figure 102).

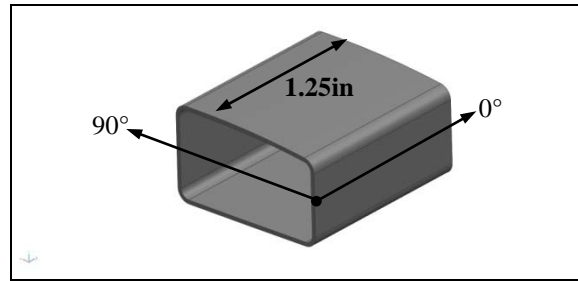


Figure 102. Carbon fiber end of wing box

Rolled dowels made from the carbon fiber tape were added to the outside corners of the joints to fill in the gaps. Blocks of foam in the shape of the hollow wing box were attached in between two carbon joints (Figure 103).

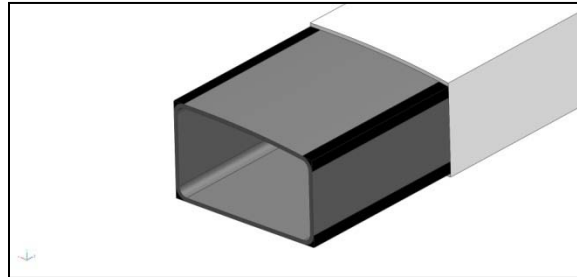


Figure 103. Wing box end with carbon fiber dowels added attached to wing box foam

The entire assembly of two end joints and foam center were wrapped in five layers of fiberglass cloth. The resulting wing box has slightly tapered hollow ends (corresponding to the carbon fiber reinforced joints) and solid foam inside the remainder of the wing box structure (Figure 104 and Figure 105).

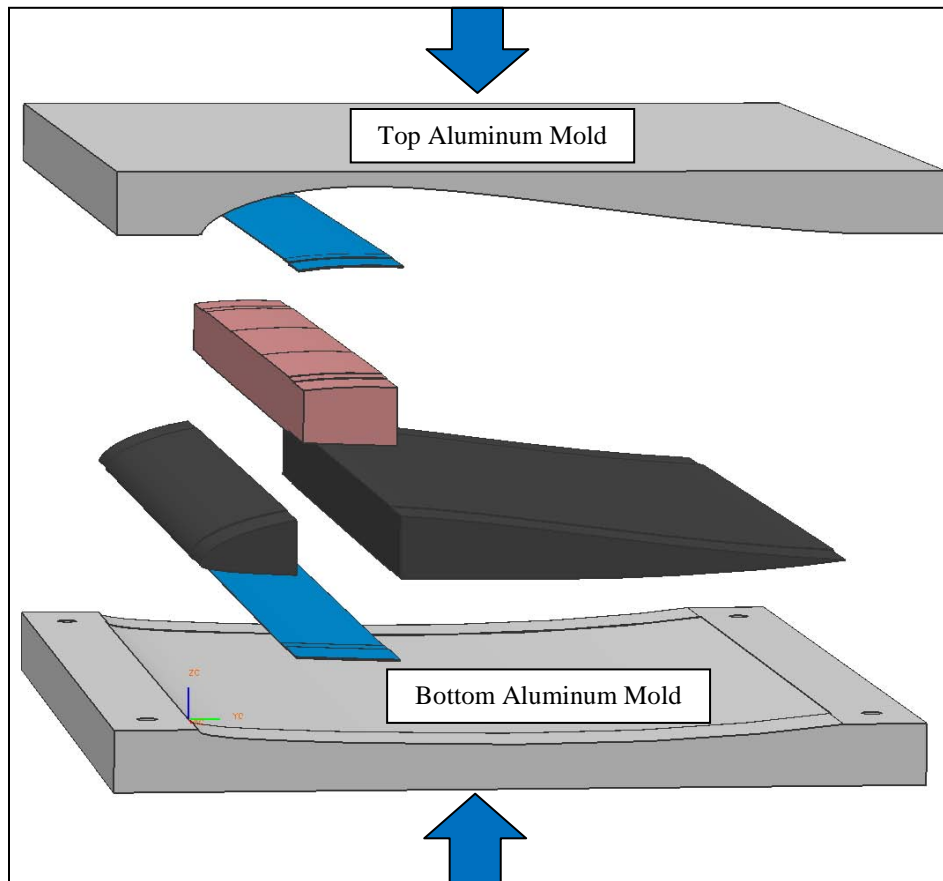


Figure 104. Layup assembly for wing box

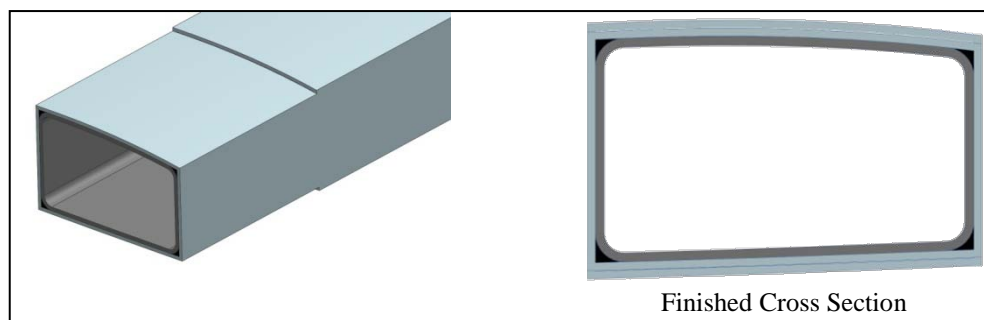


Figure 105. End of finished wing box (left) and cross section (right)

Wing Section.

The layup process continued with the fabrication of complete wing sections. Leading edge and trailing edge pieces of foam were glued to a completed and cured wing box, each of which are one meter long (Figure 106). Two layers of carbon fiber tape

were wrapped around the tapered ends of the wing section for reinforcement at the wing joints. Finally, the entire wing section was wrapped in one layer of fiberglass, creating a single wing with a span of one meter (Figure 107 and Figure 108).

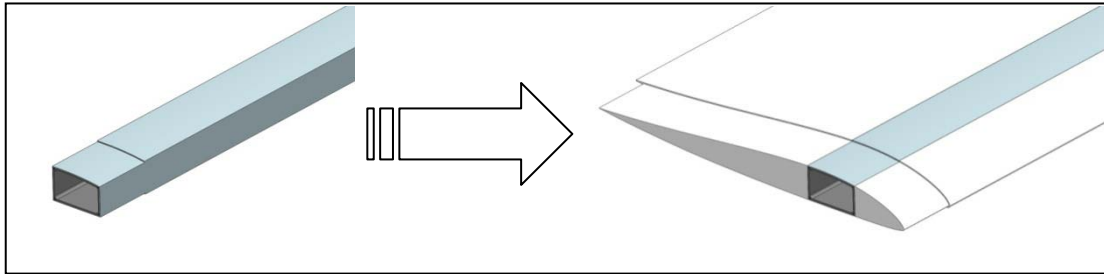


Figure 106. Completed wing box attached to leading and trailing edge sections of foam

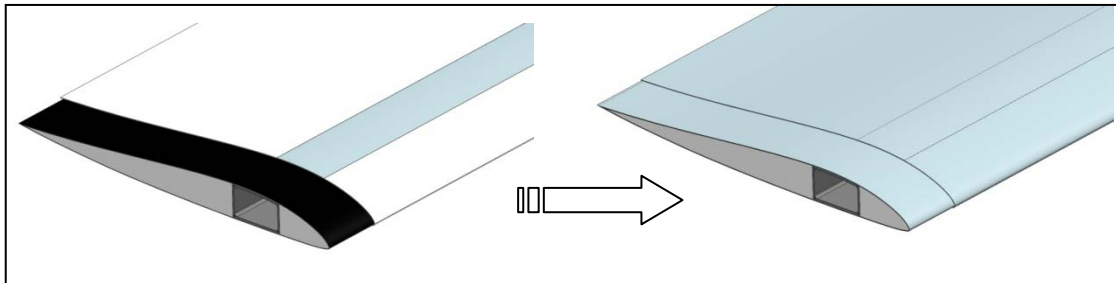


Figure 107. Single wing assembly before (left) and after (right) final fiberglass layer

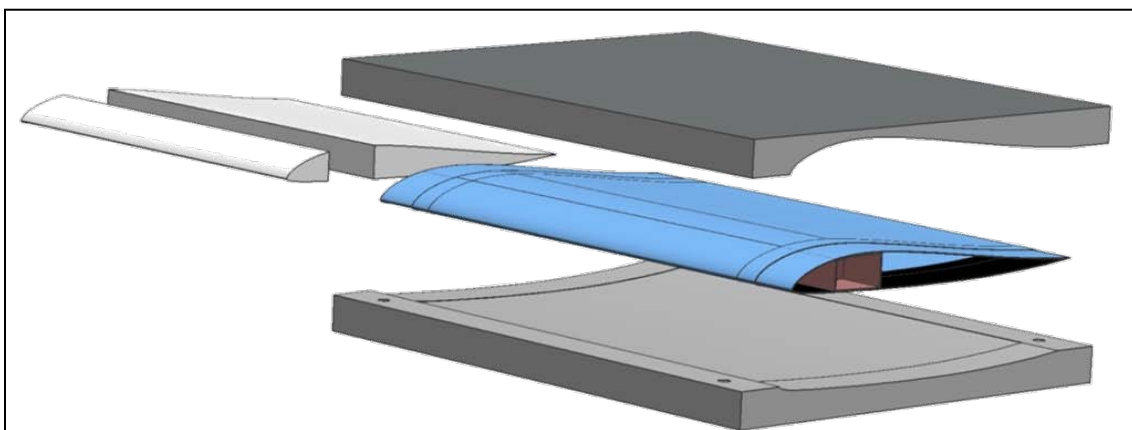


Figure 108. Layup arrangement for single wing section

Wing Joint.

The design of the joiner block which fastens each wing section together and also connects the wing structure to the five spine and engine fairings of the aircraft has evolved heavily throughout this program. The final joiner was machined from a single block of aluminum with as much mass removed as possible so as to lighten the overall aircraft weight. Figure 109 shows the design of the main joiner block and Figure 110 shows the dihedral version of the joiner block.

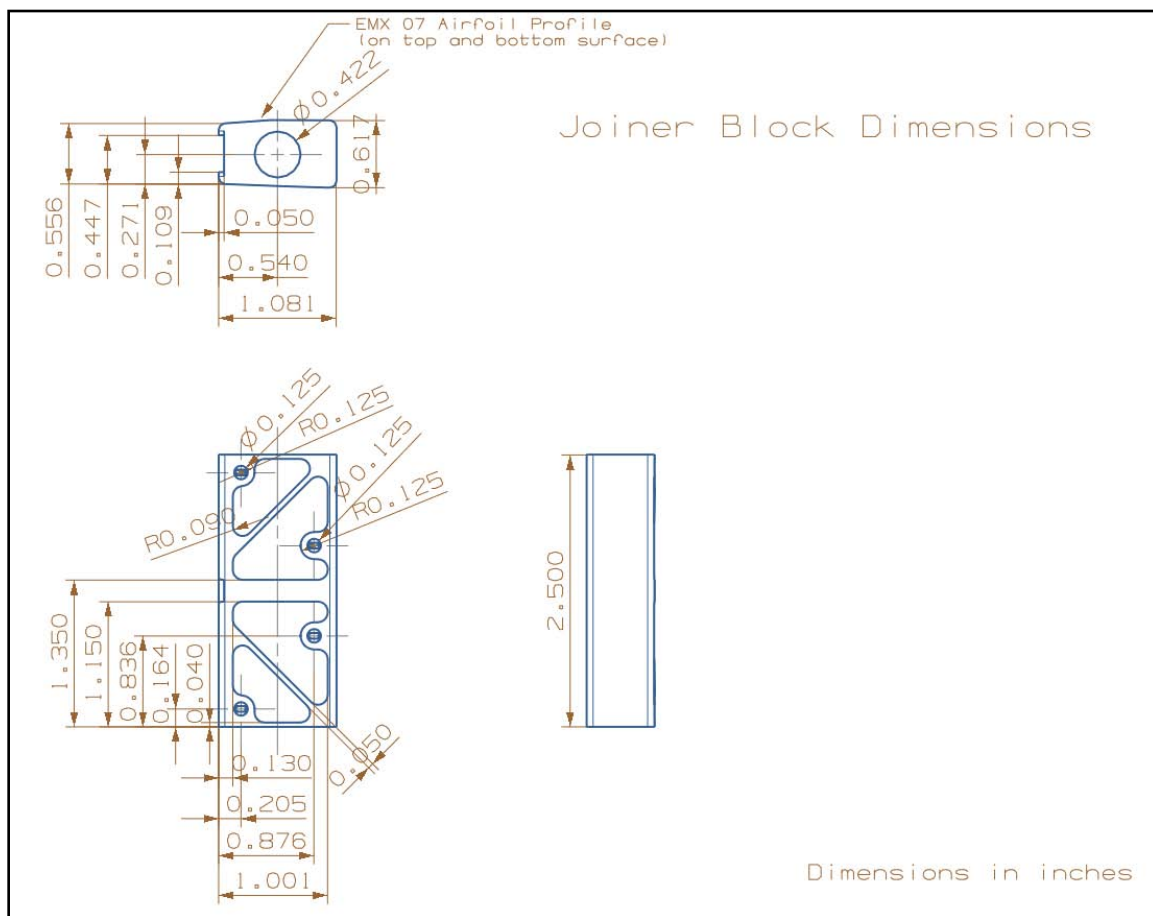


Figure 109. Three-view diagram of aluminum joiner block with dimensions

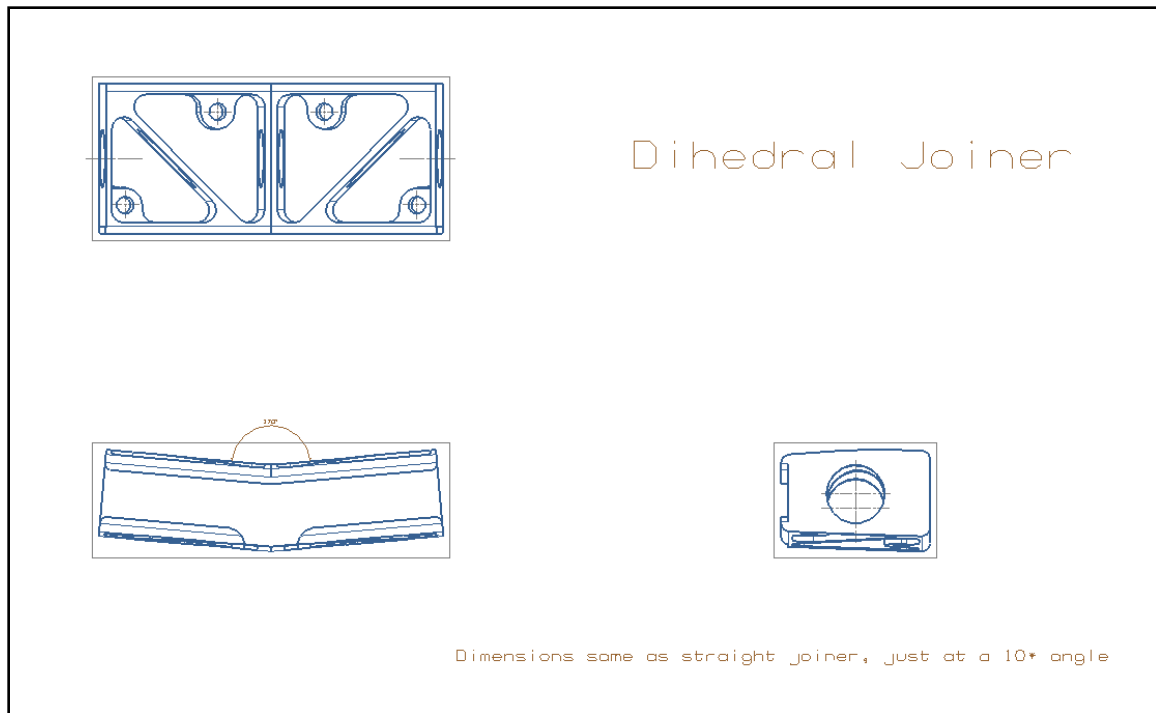


Figure 110. Three-view diagram of dihedral version of aluminum joiner block

X-HALE Testing

Test Plan [31].

Phase 1 consists of ground tests, basic flying qualities (FQ) flight tests, and a limited set of aeroelastic flight tests. Basic ground tests will be performed to ensure all systems are working properly before flights begin. Ground tests will include testing specific sub-systems, such as motor control, control surface deflections, data acquisition system, and radio communication. Also included in the ground tests will be low speed and high speed taxi tests. The FQ tests were designed to ensure X-HALE systems operate correctly during flight and to assess the stability and controllability of the aircraft. Information gathered from these basic test flights of Phase 1 will be used to develop the autopilot to be incorporated into the ATV used in Phase 2. The basic FQ tests will

include maneuvers such as take-off, turning, climb, cruise, descend, and land. Turning will be tested using various methods, including differential thrust and/or aileron inputs, to determine optimal methods of aircraft control. The aeroelastic flight tests will consist of a set of preprogrammed elevon inputs designed to excite predicted nonlinearities in the structural and rigid body nonlinear flight dynamics.

Phase 2 of X-HALE testing was planned to consist of advanced flight tests designed to stress the nonlinear coupled rigid body dynamics of the aircraft. These follow on tests will be conducted for NAST code validation.

The overall objective of the test plan is to ensure X-HALE is controllable and exhibits predicted Dutch-roll response under large excitations of the aileron. At the same time, information about the magnitude of airborne control inputs required to produce the desired nonlinear behavior will be collected. Additionally, the tests were designed to demonstrate acceptable data acquisition, storage, and transmission characteristic of the onboard systems. The test plan was designed for all maneuvers and objective to be completed with X-HALE initially assembled in a 6-m configuration, after which the sequence of maneuvers will be repeated by an 8-m configuration of X-HALE. There will be approximately five hours of flight tests during Phase 1 of the test plan.

Previous Tests [31].

Aside from the formal Phase 1 and Phase 2 portions of the test plan, several preliminary tests were conducted to predict the performance of X-HALE and what structural deflections the aircraft would experience in-flight. The physical bench tests included mass and stiffness testing of aircraft components, propeller performance testing

in the University of Michigan wind tunnel, and motor speed control testing. A graph of power vs. thrust at different airspeeds for a single engine taken from the wind tunnel can be seen in Figure 111.

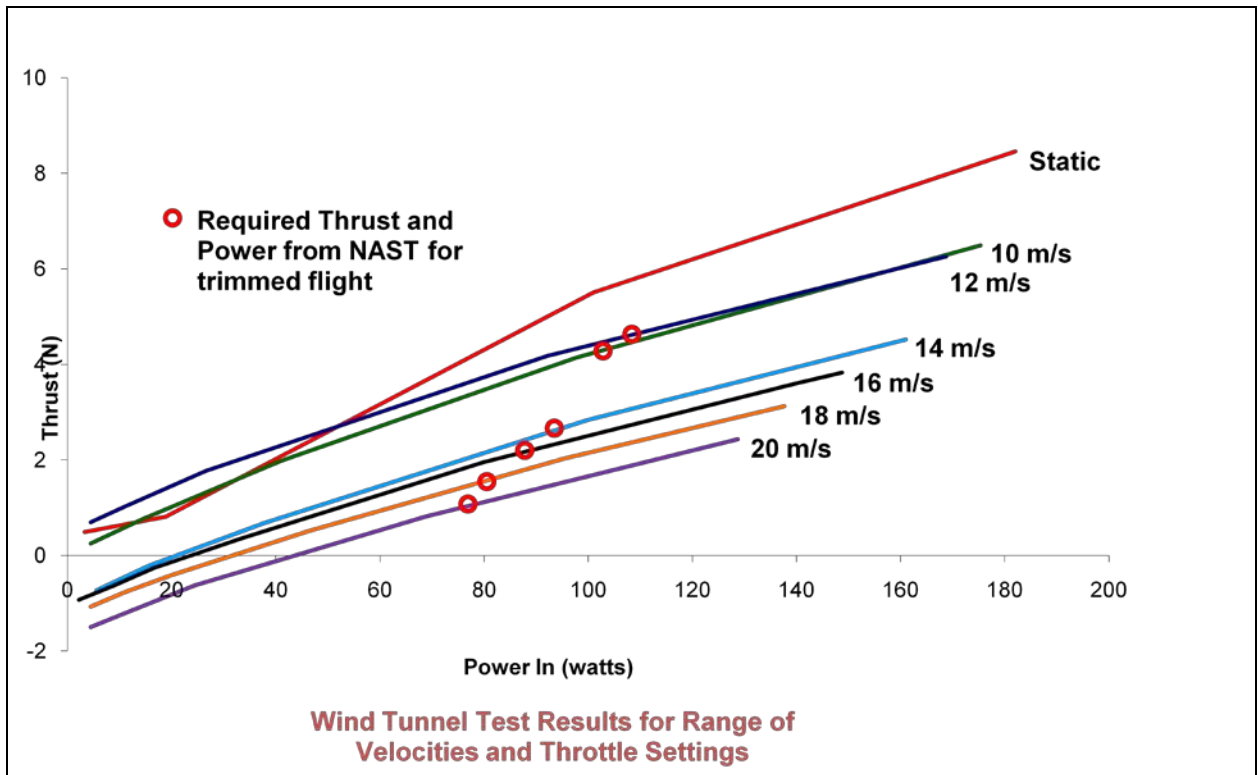


Figure 111. Graph of Power vs. Thrust [31]

Electromagnetic interference (EMI) tests were performed to ensure no interference existed among different components. Finally, the center of gravity (cg) location of the aircraft was calculated using CAD models to take into account every component's weight and position. A final cg location will be physically calculated by weighing the assembled aircraft prior to conducting actual field testing.

For all phases of testing, the X-HALE FTV will be operated as a remotely piloted aircraft (RPA). The designated pilot will operate the vehicle using R/C controls, taking off and landing on a prepared runway surface. To take off, the pilot will smoothly increase throttles to full power during the take-off roll. When the aircraft reaches a speed of approximately 15 m/s the pilot will command the aircraft to pitch up and climb away from the ground. The predicted stall speed for the aircraft is 10 m/s and onboard batteries will provide sufficient power for approximately 45 minutes of flight time before reaching roughly 80% discharged. X-HALE was designed to land normally on a runway. With no braking system incorporated into the design, it will simply roll to a stop after landing. An estimated 300 feet of runway will be required to land and stop. The pilot will use differential thrust to maintain directional control during take-off and landing

Bibliography

- [1] "AeroVironment, Inc.: Global Observer - Stratospheric Persistent UAS (Unmanned Aircraft System)," [<http://www.avinc.com/globalobserver/>, Accessed 5/7/2011.]
- [2] "Boeing Feature Story: Phantom Eye High Altitude Long Endurance aircraft unveiled," [http://www.boeing.com/Features/2010/07/bds_feat_phantom_eye_07_12_10.html, Accessed 4/3/2011.]
- [3] "Unmanned Systems Integrated Roadmap, FY2009 - 2034," 2009.
- [4] "CYTEC Industries," [<https://b2b.cytec.com/engineered-materials/products/Cycom381.htm>, Accessed 3/2/2011.]
- [5] "ASM Material Data Sheet," [<http://asm.matweb.com/search/SpecificMaterial.asp?bassnum=MA6061t6>, Accessed 4/3/2011.]
- [6] "ROHACELL® IG/ IG-F: Specification," [<http://www.rohacell.com/product/rohacell/en/products-services/rohacell-ig-ig-f/pages/default.aspx>, Accessed 2/17/2011.]
- [7] Anderson, J.D., "Introduction to flight," McGraw-Hill, New York, 2007.
- [8] Cesnik, C.E.S., and Su, W., "Nonlinear Aeroelastic Simulation of X-HALE: a Very Flexible UAV," *49th AIAA Aerospace Sciences Meeting including the New Horizons Forum and Aerospace Exposition, Orlando, Florida*, American Institute of Aeronautics and Astronautics, Inc., 2011.
- [9] Cesnik, C.E.S., Senatore, P.J., Su, W., "X-HALE: A Very Flexible UAV for Nonlinear Aeroelastic Tests," *51st AIAA/ASME/ASCE/AHS/ASC Structures, Structural Dynamics, and Materials Conference*, 2010.
- [10] Cesnik, C.E.S., and Su, W., "Nonlinear Aeroelastic Modeling and Analysis of Fully Flexible Aircraft," *46th AIAA/ASME/ASCE/AHS/ASC Structures, Structural Dynamics, and Materials Conference*, 2005.
- [11] Colella, N.J., and Wenneker, G.S., "Pathfinder and the development of solar rechargeable aircraft," *Energy and Technology Review*, 1994, pp. 1–9.
- [12] DARPA, "NewsReleaseVultureII.pdf (application/pdf Object)," [<http://www.darpa.mil/news/2010/NewsReleaseVultureII.pdf>, Accessed 2/15/2011.]

- [13] DARPA, "Vulture Program, Broad Agency Announcement (BAA) Solicitation 07-51," Defense Advanced Research Projects Agency, Arlington, VA, 2007.
- [14] Davis, J.R. ed., "Aluminum and Aluminum Alloys," ASM International, Materials Park, OH, 1993.
- [15] Galante, N. and Tschida, T., "NASA Dryden Helios Photo Collection," [<http://www.dfrc.nasa.gov/gallery/photo/Helios/index.html>, Accessed 4/15/2011.]
- [16] Gosz, M.R., "Finite Element Method: Applications in Solids, Structures, and Heat Transfer," CRC Press, Boca Raton, FL, 2006.
- [17] Hallissy, B.P., and Cesnik, C.E.S., "High-fidelity Aeroelastic Analysis of Very Flexible Aircraft," *52nd AIAA/ASME/ASCE/AHS/ASC Structures, Structural Dynamics and Materials Conference*, 2011.
- [18] Kaszynski, A.A., "X-HALE: THE DEVELOPMENT OF A RESEARCH PLATFORM FOR THE VALIDATION OF NONLINEAR AEROELASTIC CODES," 2011.
- [19] Kim, N., and Sankar, B.V., "Introduction to Finite Element Analysis and Design," Wiley, New York, 2009.
- [20] Matthews, J., "X-HALE Wing Characterization Rig Design Report," 2010.
- [21] Matthews, J., "X-HALE Wing Testing Progress Report," 2010.
- [22] Noll, T.E., Ishmael, S.D., Henwood, B., "Technical Findings, Lessons Learned, and Recommendations Resulting from the Helios Prototype Vehicle Mishap," *UAV Design Processes / Design Criteria for Structures*, Vol. RTO-MP-AVT-145, 2007.
- [23] Noll, T.E., Brown, J.M., Perez-Davis, M.E., "Investigation of the Helios Prototype Aircraft Mishap," 2004, January, [http://www.nasa.gov/pdf/64317main_helios.pdf, Accessed 4/17/2011.]
- [24] Palacios, R., Cesnik, C.E.S., and Reichenbach, E.Y., "Re-examined Structural Design Procedures for Very Flexible Aircraft," *2007 International Forum of Aeroelasticity and Structural Dynamics*, 2007.
- [25] Patil, M.J., Hodges, D.H., and Cesnik, C.E.S., "Nonlinear Aeroelasticity and Flight Dynamics of High-Altitude Long-Endurance Aircraft," *Journal of Aircraft*, Vol. 38, No. 1, 2001, pp. 88-94.
- [26] Seely, O., "Physical Properties of Common Woods," [<http://www.csudh.edu/oliver/chemdata/woods.htm>, Accessed 5/17/2011.]

- [27] Senatore, P.J., "JoinerBlock.pdf," 2009.
- [28] Senatore, P.J., Cesnik, C.E.S., and Su, W., "X-HALE Experimental Aircraft Project Overview and Progress, XHALE Overview.ppt," 2009.
- [29] Senatore, P.J., "Wing Layup read me.doc,"
- [30] Shearer, C.M., and Cesnik, C.E.S., "Nonlinear flight dynamics of very flexible aircraft," *Journal of Aircraft*, Vol. 44, No. 5, 2007, pp. 1528-1545.
- [31] Shearer, C., Cesnik, C., and Haag, C., "Experimental High Altitude Long Endurance (X-HALE) Flight Test Plan Phase 1," 2010, 11 November.
- [32] Su, W., and Cesnik, C.E.S., "Nonlinear Aeroelasticity of a Very Flexible Blended-Wing-Body Aircraft," *Journal of Aircraft*, Vol. 47, No. 5, 2010, pp. 1539-1553.
- [33] Su, W., and Cesnik, C.E.S., "Dynamic Response of Highly Flexible Flying Wings," *47th AIAA/ASME/ASCE/AHS/ASC Structures, Structural Dynamics, and Materials Conference / 14th AIAA/ASME/AHS Adaptive Structures Conference*, 2006.
- [34] Truss, L., "Eats, shoots, and leaves," Gotham, 2003.
- [35] Wang, Z., Chen, P., Liu, D., "Nonlinear Aeroelastic Analysis for A HALE Wing Including Effects of Gust and Flow Separation," *48th AIAA/ASME/ASCE/AHS/ASC Structures, Structural Dynamics, and Materials Conference*, 2007.
- [36] Wilson, J., "Fly Like a Vulture," *Aerospace America*, 2008, pp. 28-33.

Vita

LCDR Nicholas A. Sinnokrak conducted his undergraduate studies at the University of Illinois in Urbana-Champaign under the NROTC scholarship program. He earned a Bachelor of Science degree in Aeronautical and Astronautical Engineering and was commissioned an Ensign in December 2000. After completing flight training at NAS Pensacola, he was designated a Naval Flight Officer in August 2002 and assigned to Sea Control Squadron FOUR ONE (VS-41) at NAS North Island, CA for Fleet Replacement training in the S-3B Viking.

In July 2003 he was assigned to Sea Control Squadron THREE THREE (VS-33) where he completed two deployments aboard the aircraft carrier USS CARL VINSON (CVN-70). Remaining in San Diego, in July 2006 he reported to PEO C4I at SPAWAR where he served as Deputy Assistant Program Manager for the Air GPS program within the Navy's Communication and Navigation Program Office (PMW/A-170).

In August 2009 he began his graduate work at the Air Force Institute of Technology in the Department of Aeronautics and Astronautics. Upon completing his degree he will report to U.S. Navy Test Pilot School to begin the Airborne Systems Test program.

REPORT DOCUMENTATION PAGE				Form Approved OMB No. 074-0188	
<p>The public reporting burden for this collection of information is estimated to average 1 hour per response, including the time for reviewing instructions, searching existing data sources, gathering and maintaining the data needed, and completing and reviewing the collection of information. Send comments regarding this burden estimate or any other aspect of the collection of information, including suggestions for reducing this burden to Department of Defense, Washington Headquarters Services, Directorate for Information Operations and Reports (0704-0188), 1215 Jefferson Davis Highway, Suite 1204, Arlington, VA 22202-4302. Respondents should be aware that notwithstanding any other provision of law, no person shall be subject to a penalty for failing to comply with a collection of information if it does not display a currently valid OMB control number.</p> <p>PLEASE DO NOT RETURN YOUR FORM TO THE ABOVE ADDRESS.</p>					
1. REPORT DATE (DD-MM-YYYY) 16-06-2011		2. REPORT TYPE Master's Thesis		3. DATES COVERED (From – To) FEB 2010 – May 2011	
4. TITLE AND SUBTITLE Process for Refining and Validating a Finite Element Model of an Experimental High-Altitude, Long-Endurance (HALE) Aircraft				5a. CONTRACT NUMBER	
				5b. GRANT NUMBER	
				5c. PROGRAM ELEMENT NUMBER	
6. AUTHOR(S) Sinnokrak, Nicholas A., Lieutenant Commander, USN				5d. PROJECT NUMBER	
				5e. TASK NUMBER	
				5f. WORK UNIT NUMBER	
7. PERFORMING ORGANIZATION NAMES(S) AND ADDRESS(S) Air Force Institute of Technology Graduate School of Engineering and Management (AFIT/EN) 2950 Hobson Way, Building 640 WPAFB OH 45433-7765				8. PERFORMING ORGANIZATION REPORT NUMBER AFIT/GAE/ENY/11-J04	
9. SPONSORING/MONITORING AGENCY NAME(S) AND ADDRESS(ES) Intentionally left blank				10. SPONSOR/MONITOR'S ACRONYM(S)	
				11. SPONSOR/MONITOR'S REPORT NUMBER(S)	
12. DISTRIBUTION/AVAILABILITY STATEMENT APPROVED FOR PUBLIC RELEASE; DISTRIBUTION UNLIMITED.					
13. SUPPLEMENTARY NOTES This material is declared a work of the U.S. Government and is not subject to copyright protection in the United States.					
14. ABSTRACT The work presented here focuses on finite element (FE) modeling of X-HALE, a test aircraft designed and built by the University of Michigan, in conjunction with the Air Force Institute of Technology (AFIT) and Air Force Research Laboratory (AFRL). This scaled vehicle is representative of high-altitude, long-endurance (HALE) aircraft and was designed to provide controlled aeroelastic and flight data. FE models of portions of the X-HALE wing structure were created and analysis results were compared against two separate laboratory static bending tests conducted on X-HALE wing sections. The process documented here should improve future efforts to refine FE models of X-HALE. Improved modeling techniques will help design and test X-HALE to provide data for future designs of HALE aircraft and will also help to validate coupled nonlinear aeroelastic and flight dynamic codes. Results of the FE models created indicate the manufactured wing structure possesses material properties close to those expected of the composite materials used in its design. However, the results also suggest additional focus is required to accurately model the wing joint region of the X-HALE structure, with specific attention paid to the joiner piece which connects the wing sections together.					
15. SUBJECT TERMS Aircraft, high altitude, long endurance, finite element, FEMAP, X-HALE					
16. SECURITY CLASSIFICATION OF:			17. LIMITATION OF ABSTRACT	18. NUMBER OF PAGES	19a. NAME OF RESPONSIBLE PERSON
a. REPORT	b. ABSTRACT	c. THIS PAGE			Christopher Shearer, Lt Col, USAF
U	U	U	UU	154	19b. TELEPHONE NUMBER (Include area code) (937) 255-1179 (Christopher.Shearer@wpafb.af.mil)

Standard Form 298 (Rev. 8-98)
Prescribed by ANSI Std. Z39-18